2008

LINKING THE STRUCTURE AND MECHANICAL BEHAVIOR OF NANOPOROUS GOLD

Ye Sun
University of Kentucky, sun.ye1@gmail.com

ABSTRACT OF DISSERTATION

Ye Sun

The Graduate School

University of Kentucky

2008

LINKING THE STRUCTURE AND MECHANICAL BEHAVIOR OF NANOPOROUS GOLD

ABSTRACT OF DISSERTATION

A dissertation submitted in partial fulfillment of the
requirements for the degree of Doctor of Philosophy in the
College of Engineering
at the University of Kentucky

By
Ye Sun

Lexington, Kentucky

Director: Dr. T. John Balk, Professor of Chemical and Materials Engineering

Lexington, Kentucky

2008

ABSTRACT OF DISSERTATION

LINKING THE STRUCTURE AND
MECHANICAL BEHAVIOR OF NANOPOROUS GOLD

The structure of nanoporous gold (np-Au) provides a very limited volume for deformation to occur, and thus offers an opportunity to study the role of defects such as dislocations in nanoscale metal volumes. A practical goal is to understand mechanical properties of np-Au so that it can be can produced in stable form, for use in applications that require some mechanical integrity. Bulk and thin film np-Au have been fabricated and studied here.

Bulk np-Au was prepared by electrochemically dealloying Au-Ag alloys with 25 and 30 at.% Au. In the lower Au content material, cracks always formed during dealloying. When Au content increased to 30 at.% and a two-step electrochemical dealloying method was used (first using diluted electrolyte and then concentrated acid), bulk np-Au with no volume change and minimal cracking was successfully fabricated. Thermal and mechanical behavior of np-Au was studied by heat treatment and microindentation. During annealing in air, Ostwald ripening governed ligament coarsening, while annealing of ligaments in vacuum was more likely a sintering process.

Nanoporous Au thin films were produced by dealloying sputtered Au-Ag alloy films. Residual stresses in np-Au films were measured with wafer curvature. Similar to bulk materials, np-Au thin films made from 25 at.% Au alloy films exhibited extensive cracking during dealloying, whereas films from 30 at.% Au precursor alloys were completely crack-free. 25 at.% Au np-Au films carried almost no stress because of extensive cracking, whereas stress in 30 at.% Au np-Au films was up to ~230 MPa. Ligament coarsening followed a $t^{1/8}$ time dependence for stress-free films, versus $t^{1/4}$ in films under stress. It was proposed that bulk diffusion was responsible for formation of larger pits at grain centers during the incipient stages of dealloying.

In situ nanoindentation experiments inside the transmission electron microscope were performed to investigate deformation of np-Au films and dislocation motion within ligaments. Dislocations were generated easily and moved along ligament axes, after which they interacted with other dislocations in the nodes of the porous network. It was

found that slower displacement rates caused load drops to occur at shorter distance intervals and longer time intervals.

KEYWORDS: nanoporous, gold, dealloying, mechanical behavior, *in situ* TEM

Ye Sun

October 31, 2008

LINKING THE STRUCTURE AND
MECHANICAL BEHAVIOR OF NANOPOROUS GOLD

By

Ye Sun

T. John Balk, Ph. D.
Director of Dissertation

Douglass S. Kalika, Ph. D.
Director of Graduate Studies

October 31, 2008

RULES FOR THE USE OF DISSERTATIONS

Unpublished dissertations submitted for the Doctor's degree and deposited in the University of Kentucky Library are as a rule open for inspection, but are to be used only with due regard to the rights of the authors.

Bibliographical references may be noted, but quotations or summaries of parts may be published only with the permission of the author, and with the usual scholarly acknowledgments.

Extensive copying or publication of the dissertation in whole or in part also requires the consent of the Dean of the Graduate School of the University of Kentucky.

A library that borrows this dissertation for use by its patrons is expected to secure the signature of each user.

Name Date

_____

_____

_____

_____

_____

_____

_____

_____

_____

_____

_____

DISSERTATION

Ye Sun

The Graduate School

University of Kentucky

2008

LINKING THE STRUCTURE AND MECHANICAL BEHAVIOR OF NANOPOROUS GOLD

DISSERTATION

A dissertation submitted in partial fulfillment of the
requirements for the degree of Doctor of Philosophy in the
College of Engineering
at the University of Kentucky

By
Ye Sun

Lexington, Kentucky

Director: Dr. T. John Balk, Professor of Chemical and Materials Engineering

Lexington, Kentucky

2008

ACKNOWLEDGMENTS

There are many people I would like to thank who have helped me become a better scientist, either directly or through friendship and support. I will begin with my research advisor, Dr. T. John Balk. This dissertation could not have been written without Dr. Balk who not only served as my supervisor but also encouraged and challenged me throughout my academic program. I would like to express my acknowledgment to him for his stimulating suggestions, guidance and encouragement during my four years Ph. D. study as well as for helping with life in Lexington. I thank Dr. Balk's wife, Ilka for her help, kindness and generosity to my family. I also want to thank Dr. Balk's parents, Thomas and Michele. I appreciate their hospitality and generosity when I visited San Francisco.

I thank the members of my committee: Dr. Bruce Hinds, Dr. Chi-Ying Man, Dr. Stephen Rankin. I appreciate your time and energy to attend meetings, my oral exam, and my exit seminar. I thank you for agreeing to be on my committee and especially for reading this dissertation

I thank Dr. Andrew Minor and Dr. Fuqian Yang for their help and advice in my research. I thank Mr. Larry Rice and Dr. Alan Dozier for their assistance in learning SEM and TEM.

I would also like to thank my colleagues as well as friends who shared discussion, knowledge and ideas, and collaborated with experiments and research: Wen-Chung Li, Sofie Burger, Simone Schendel, Kalan Kucera, Jessica Fleming, Rachel Wilson, Christian Schumacher, Rong Chen, Qiang Zeng and Jianhui Xu.

I am also indebted to my family: my wife, Yunyan, my son, Weilun and my parents, Guangda Sun and Yuqin Yun, for their support, patience and love, without which I am not able to finish this work.

Thanks to the American Chemical Society Petroleum Research Fund, National Center for Electron Microscopy (NCEM), University of Kentucky Graduate School and Department of Chemical and Materials Engineering for their financial support of this work.

Thanks to all the people that helped and believed in me.

TABLE OF CONTENTS

LIST OF TABLES

LIST OF FIGURES

LIST OF FILES

YeSunDissertation.pdf	13 MB

Chapter 1

Introduction

Porous materials have attracted considerable attention in science and engineering. The varieties are many including porous carbon, porous silicon, porous inorganic oxides, porous polymeric materials and porous metals. All these porous materials have a common advantage: high surface-to-volume ratio. Most applications of porous materials take advantage of their high surface area, though specific properties may be needed for particular purposes. For example, many have found that porous materials are useful in optical applications [1, 2]. When the pore size of a material falls into the range of several to tens of nanometers, it may be referred to as a nanoporous material.

Nanoporous materials can be fabricated by many approaches. One of them is using templates to form the nanoporous structure, including anodic porous alumina membranes [3], templates formed from self-assembled structures of inorganic-block copolymer micelles [4] and polymer templates [5]. Other methods include electrodeposition from a liquid crystalline plating mixture [6], introducing gases in molten metals [7], and etching or dealloying binary alloys [8].

Of all porous materials, one important class is porous metals, which share the virtues of light weight, good conductivity and large internal surface area and which therefore can be used in energy absorption devices and heat dissipation devices [9]. Porous metals can be classified by the method of manufacture, pore spatial distribution and their applications. Porous metals can be made by dealloying, powder metallurgy, chemical and electrochemical deposition, physical vapor deposition, casting and gas-eutectic transformation, which were reviewed by Shapovalov [10]. Among these methods, dealloying of binary alloy to make nanoporous metals is of particular interest in the present work and will be discussed in more detail in Chapter 2. To make nanoporous metals, the precursor alloys need to meet at least two requirements: firstly, the alloy should be composed of two elements, with one more noble and the other less noble; secondly, the alloy should be homogeneous with no phase separation at the alloy composition. Numerous systems have been observed that have the ability to form

nanoporous structure by dealloying, including Mn-Cu [11, 12], Cu-Au [13, 14], Cu-Pd [15], Au-Ag [16-19], Zn-Cu [20, 21], and Mg-Cd [22, 23]. Among these binary alloy systems, Au-Ag alloy is of particular interest in the present study due to its resultant nanoporous Au, because Au has unique physical and mechanical properties. For example, Au can be attached by bio-particles via Au-thiol bonds, which makes it a promising candidate in biotechnology applications. However, to fully take advantages of the virtues of nanoporous Au, an important aspect that must to be understood is its mechanical properties, because the mechanical integrity or robustness of nanoporous metals is vital for their applications.

It is worth noting that the nanoporous materials here refer to porous materials that have porous structure with pore sizes ranging from several to tens of nanometers. However, according to a convenient classification, first used by Dubinin [24] and later accepted by the IUPAC [25], there is not an official term "nanoporous". The IUPAC classification is summarized in Table 1.2. The pore sizes in the present research fall into the category of mesopores. But "nanoporous" is also extensively used and accepted by many researchers in materials science. Throughout this dissertation, "nanoporous" is used.

Table 1.1 IUPAC classification of porous materials according to pore size.

Classification	Pore size *d* (nm)
Macropores	> 50
Mesopores	2 – 50
Micropores	< 2

This dissertation concentrates on the microstructure and mechanical behavior of nanoporous Au. By examining the microstructural evolution of np-Au during dealloying using electronic microscopy, along with compositional change by energy dispersive spectrometry (EDS), an attempt to better understand the mechanism of dealloying was made. Mechanical behavior of nanoporous Au thin films were studied using the wafer curvature technique, through which residual stresses in thin films at various stages of

dealloying were measured. Evolution of ligament coarsening was monitored and analyzed by statistically measuring scanning electron micrographs, and kinetics of ligament growth during dealloying was discussed as well as possible effects of stress on ligament coarsening. Emphasis was also placed on improving the dealloying process to avoid cracking, because crack formation was initially a general problem encountered during dealloying. Thermomechanical behavior of np-Au was also investigated. By measuring residual stress during cooling and heating processes via the wafer curvature technique, the lower limit of yield strength of ligaments was calculated. In addition, microindentation testing was used to evaluate the mechanical properties of bulk np-Au. *In situ* nanoindentation was performed in the transmission electron microscope (TEM), with which dislocation-governed deformation behavior was studied.

Chapter 2

Background

2.1 Introduction of nanoporous Au

Nanoporous Au (np-Au) is a relatively new material and has gained more and more interest in recent years. Nanoporous Au exhibits interesting properties and structural features. For example, this nanoporous structure has high surface area, so it could be quite useful in applications such as gas sensing or catalysis. Figure 2.1 shows a typical nanoporous structure of bulk np-Au made from a 25at% Au-Ag alloy by electrochemical dealloying. Usually, the pores and ligaments are in the range of a few to tens of nanometers in the as-dealloyed state, with a normal distribution of ligament width. Nanoporous Au can be fabricated by etching Au-Ag alloys using a process called dealloying. During dealloying, Ag atoms dissolve and Au atoms aggregate, forming a structure with interconnected ligaments and nanoscale pores between the ligaments. The mechanism of dealloying has been investigated extensively. Several models have been proposed to explain the dealloying mechanism, including dissolution-redeposition mechanism, volume diffusion mechanism, surface diffusion mechanism, and percolation mechanism. However, even though nanoporous Au has been investigated extensively since the 1980's, many aspects of the material still require further study, such as crack formation and volume change during dealloying, dislocation activity during deformation, and the overall mechanical properties of np-Au. In this chapter, a literature review of np-Au will be presented.

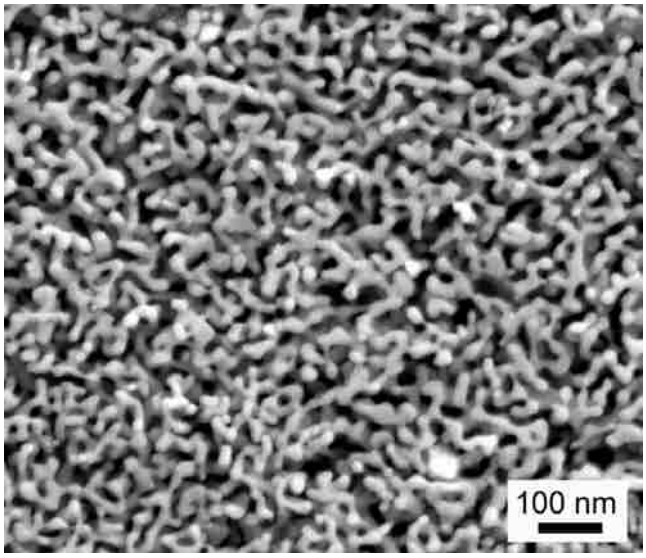

Figure 2.1 Morphology and microstructure of bulk np-Au made by dealloying a 25 at% Au-Ag alloy, showing the sponge-like nanoporous structure that is created when Ag atoms are leached from the Au-Ag alloy and the remaining Au atoms self assemble into interconnected ligaments.

2.2 Applications of np-Au

Because of its nanoscale sponge-like structure, its noble metal character, and its high resistance to oxidation, np-Au has many potential applications. One important application of np-Au is as a biosensor, where np-Au serves as a linking layer on the transducer surfaces of biosensors and immobilizes receptor clusters, such as bio-molecules, cells, and neurons. Application of np-Au as an actuator has been also been investigated [26, 27], where np-Au displayed large mechanical reactions when subjected to an external voltage. Other applications of np-Au include those in catalysis, in optical coatings, in fuel cells, and in ultra-capacitors [28].

2.2.1 Biosensors

Due to its high specific surface area and its stability in a variety of conditions, nanoporous Au is more suitable for biosensor applications than other porous materials or those with smooth surfaces. Nanoporous Au can be used as an electrically conductive, porous scaffold on which functionalized coatings/groups are assembled. Au surface is a

very appropriate basis for such self-assembly due to its metallic nature, high nobility, and particular affinity for sulphur. This allows the nanoporous Au surface to assemble various groups including thiols and other organic molecules once they contain or have been modified to contain a sulphur atom [29]. Depending on the substance being adsorbed, adsorption of acceptors has been proven to increase 3 to 11 times after porous Au was used to replace the planar Au surface [30-33], which consequently results in improved signal detection.

2.2.2 Actuators

The significance of understanding reactions of np-Au subjected to external stimuli is that it largely extends the scope of application of np-Au. Kramer *et al.* [27] investigated the deformation of np-Au in an electrochemical cell and reported that the charge-induced expansion or contraction of the porous metal could induce a biaxial stress that resulted in large bending of the foil. A bilayer foil was devised according to this principle, and behaved similarly to a bimetal thermometer. One layer was the nanoporous metal (np-Au) and the other a solid metal layer (Au). When the bilayer foils are immersed in an electrolyte, the porous layer tends to expand or contract, while the solid metal layer tends to retain its dimensions, resulting in a shear stress at the interface between the two layers and millimeter scale deflecion. Weissmuller *et al.* [26] also reported dimensional changes of nanoporous Pt in response to an applied voltage.

2.2.3 Optically selective coatings

Another potential application for nanoporous Au is in the young field of plasmonics [34]. It has been shown that a nanoscale mesoporous film of metal can be observed to be optically selective for certain wavelengths of visible light. In this situation, where the holes in such a film are actually far smaller than the wavelength of visible light, the layer would be opaque under normal optical criteria. However, light can actually be conducted through the nanoscale holes by the mechanism of surface plasmon resonance, with the net effect that the layer can become transparent [35].

2.2.4 Ultra-capacitors

Ultra-capacitors (also known as 'electrolytic double-layer capacitors' or 'super-capacitors') are based on the interface properties of mesoporous conductors immersed in liquid electrolytes. Ultra-capacitors have considerably better power-buffering capacities than chemical batteries or ordinary capacitors. The capacitance of ultra-capacitors is significantly magnified over those of ordinary parallel plate capacitors by two factors: their high specific surface area, and the small value of the effective dielectric thickness of the charged double layer. Carbon-based ultra-capacitors suffer limitations in performance at high power ratings due to the internal resistance of their porous carbon aggregates, which limits power draw [36]. Nanoporous Au might find application in this area because of its relatively high surface area and its excellent electrical conductivity. Since devices based on np-Au have much lower resistances than carbon-based ultra-capacitors, they should deliver much higher volumetric power density, though at a higher cost.

2.2.5 Catalysis

The platinum catalyst of polymer electrolyte membrane (PEM) fuel cells is extremely sensitive to CO poisoning, making it necessary to employ an additional reactor to reduce CO in the fuel gas if the hydrogen is derived from an alcohol or hydrocarbon fuel. Researchers are still working on finding the next generation nanostructures to use as catalyst to facilitate the conversion of CO. Nanoporous Au, as a new catalytic material to convert CO, has attracted recent attention [37-40]. Xu *et al.* [39] reported extraordinary catalytic properties of np-Au for CO oxidation. At room temperature, CO can be converted to CO_2 by unsupported bulk np-Au with a conversion higher than 95% for 20 hours. The conversion dropped to ~75% after 35 hours. Ligament size increased significantly after room temperature catalysis activity, which is the reason for the decrease in efficiency. At -30 °C, higher than 85% conversion rate can be achieved by np-Au and no obvious efficiency drop was found in 30 hours, while only a slight increase in ligament size was observed (5 to 8 nm). This gives np-Au unique advantages of sustaining stability and high efficiency at low temperatures.

The high cost of precious metals (usually platinum) used in the conventional PEM fuel cell, as well as the degradation of catalyst over long periods of use, imposes a huge

obstacle to large-area application of PEM fuel cells. A new concept of platinum-plated nanoporous Au was created to reduce the high cost of platinum while maintaining the high performance efficiency [37, 38]. Platinum-coated np-Au membranes were made through an electroless deposition in which np-Au leaf was placed at the interface between electrolyte containing platinum salt solution and a vapor of a reducing agent. Using this technique, approximately one atomic monolayer of Pt can be coated on the conductive substrate. Fuel cells using the Pt-coated np-Au membrane were reported to be able to generate an output power of up to 4.5 kW g^{-1} Pt by at a Pt load of 0.028 mg cm^{-2}, compared to 1.0 kW g^{-1} with loading of 0.5 mg cm^{-2} of Pt of a typical commercially available membrane electrode assembly (MEA) [41].

2.3 Dealloying

2.3.1 Dealloying and its mechanism

Dealloying is a selective dissolution process of a precursor alloy, during which the less noble (LN) atoms are dissolved, while the more noble (MN) atoms aggregate instead of being leaching off, leaving behind a nanoscale, interconnected network of open pores. Dealloying is an ancient technology: Ausmiths used this technique to enhance the surfaces of their artifacts, which can be traced back to fifth and fourth century BC [42]. By this technology, Au-Cu or Au-Ag alloys were dealloyed by chemicals to create a pure Au surface layer, during which copper or silver was removed from the surface of alloys. This technique was known as depletion gilding.

In recent times, selective dissolution has been examined in the context of corrosion [43], especially in terms of stress-corrosion cracking (SCC). Newman and Sieradzki *et al.* investigated the function of nanoporous Au layers on the film-induced cleavage of alloy substrates beneath porous layers [44-46]. They studied cracking propagation in dealloyed layers of Au-Ag alloy under tensile stress. They showed that the porous layer served to nucleate brittle cracks that propagate into uncorroded bulk face-centered cubic materials for many microns. These brittle cracks could be intergranular (IG) or transgranular (TG) and film-induced cleavage or film-induced cracking (FIC) was thought to be the mechanism. Pickering [14], however, thought that anodic dissolution is responsible for stress corrosion in the Cu-Au alloys. According to his mechanism,

materials along the operating slip plane dissolve rapidly, in association with the anodic dissolution process, and then the remaining materials between pores may rupture.

With the pioneering work of Pickering [21] and Forty [17, 18, 47], as well as subsequent work by Sieradzki and Erlebacher, significant advances were made in understanding the electrochemical mechanism of dealloying. The basic problem of dealloying involves how the atoms are dissolved and how they move or transport at the alloy surface or within the solid state. Figure 2.2 shows a schematic of the terrace-ledge-kink model of dissolution of Ag from a Au-Ag alloy. Of course, this model applies to other binary alloy systems as well. According to this model atoms are most readily dissolved from kink sites (K in Figure 2.2) of the surface steps. For a binary alloy system, a less noble atom at kink site will move from its kink position and become an adsorbed atom, which will then enter the solution subsequently and become an ion. With further dissolution of those less noble atoms at kink sites more and more kink sites become occupied by the more noble atoms. Then less noble atoms at non-kink sites (N) and terrace sites (T) will be removed thereafter, while greater activation energy or overpotential is required. Eventually, all the surface sites are occupied by the more noble atoms and the alloy becomes passivated. Further dealloying can only continue if the less and more noble atoms can exchange positions.

There are four possible mechanisms of atom transportation that may account for the formation of nanoporous structure in a binary alloy system: (1) dissolution-redeposition mechanism: both metals ionize, or dissolve, followed by redeposition of the more noble metal; (2) surface diffusion mechanism: only the less noble atoms dissolve and the more noble atoms aggregate by surface diffusion; (3) volume diffusion mechanism: only the less noble atoms ionize and enter the solution and atoms of both metals transport in the solid phase by volume diffusion; (4) percolation model: there exists a continuous connected cluster of less noble element atoms, which provides a pathway for dissolution as well as the electrolyte.

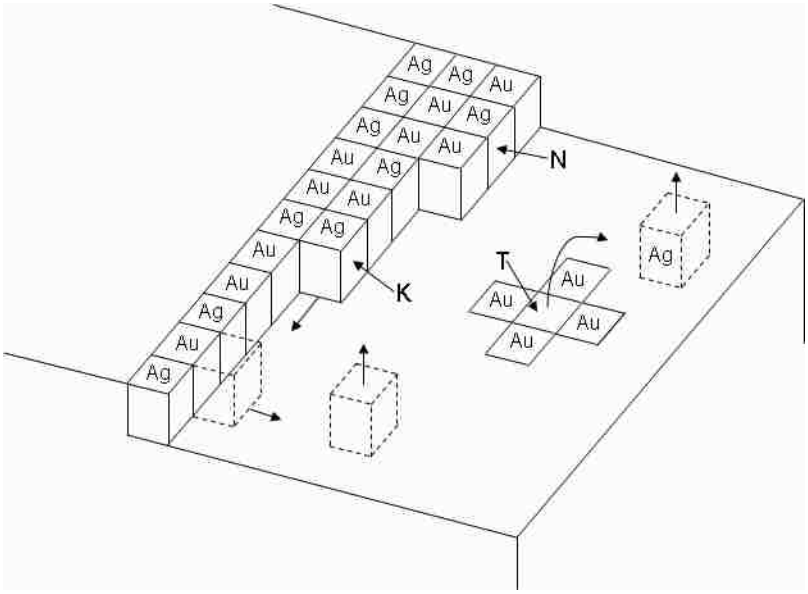

Figure 2.2 Schematic of dissolution of Ag from a Ag-Au alloy. K is a kink site on a surface step, N is a non-kink site on a step, and T is a terrace site. Ag atoms at the kink sites will dissolve first, while those at the N and T positions will be removed when greater activation energy can be obtained. This figure was adapted from Figure 1 in the following literature: Forty, A.J., *Micromorphological studies of the corrosion of gold alloys.* Gold Bulletin, 1981. **14**(1): p. 25-35. Copyright of World Gold Council.

Pickering and Wagner [21] proposed that volume diffusion played an important role in movement of species in the solid state. It was suggested in the model that less noble atoms at kink sites dissolve and become ionized. Atoms at non-kink sites on a step may enter the solution as a divalent ion if the driving force is sufficiently high. All less noble atoms from a complete lattice layer could then be removed and enter solution, resulting in surface vacancies. These surface vacancies could be either filled by lone adsorbed atoms on the surface or by atoms from the lattice layer underneath the surface. The filling of these surface vacancies by atoms underneath the surface will result in the movement of atoms from the bulk alloy to the surface, and therefore, at the same time, the creation of excess vacancies in the interior of the alloy by the transportation of less noble atoms to the surface. The progressive increase of an excess vacancy concentration near the surface will improve diffusion of less noble atoms to the surface from the bulk

alloy while more noble atoms diffuse backwards because of the gradient of the ratio between these two elements.

Using electron microscopy Forty *et al.* [17-19, 47] observed the morphology of Au-Ag films with various Au content (33 to 67 at%) after dealloying by HNO_3 and used the results to deduce the model of the processes involved in the dissolution of these alloys. The first part of Forty's model is similar to that of Pickering and Wagner, and he proposed that preferential dissolution of Ag happened first at kink sites in the surface steps on (111) film surfaces. These kink sites were occupied by Au atoms and monatomic Au-rich discs were formed by diffusion of Au atoms along the steps. Further reordering of Au adatoms on the surface resulted in Au island formation and growth, as well as pit formation. This aggregation of the Au adatoms into islands continuously exposed fresh alloy to the acid so that the surface was not passivated and further dealloying proceeded continuously. The main difference between Forty's model and Pickering's is that the former attributed the reordering or migration of Au adatoms to surface diffusion while the latter ascribed the continuous replenishment of less noble atoms at the surface to volume diffusion. Through further dealloying, Au-rich islands may coalesce, while the channels between the islands deepen.

Substantial work on the mechanism of dealloying has also been performed more recently by Erlebacher *et al.* [8, 48, 49]. The authors presented an analytical atomistic model combined with computational simulation that described the underlying physics of porosity evolution during dealloying. Both computational and experimental investigations on porosity formation and mechanical behavior of np-Au have been performed. They proposed that porosity formation of Au-Ag alloys during selective dissolution processes as follows: a Ag atom was dissolved and entered solution. Ag atoms coordinating with it were dissolved subsequently because of their increased susceptibility to dissolution. Au atoms at kink sites in the topmost layer did not dissolve, but aggregated into clusters. When the second layer of alloy was attacked by the electrolyte, similarly, Ag atoms were removed and Au atoms transported to the Au clusters formed earlier. The maximum distance that Au atoms can transport, i.e. the distance between Au clusters, is called the characteristic spacing, λ. Eventually, a series of hills were formed. According to the authors, these hills had high Au content at their

peaks, but alloy composition at their bases. These hills were subjected to "undercutting", which increased the distance that Au atoms must travel to clusters. If the distance became too long for Au atoms to travel, new clusters were nucleated, driven by kinetics, leading to new pit formation. Ultimately, interconnected channels and porosity developed.

Sieradzki *et al.* proposed [50] a percolation model for the selective dissolution process. A two dimensional schematic of this percolation model is shown in Figure 2.4 [51]. According to the model, continuous connected clusters of the less noble element (Ag in Figure 2.4) must exist in order to dissolve these less noble atoms. Through the pathway provided by these percolating clusters, electrolyte is not only able to remove less noble atoms on the surface as well as those located interior but also penetrate into the bulk solid. The penetration of electrolyte was also facilitated by coarsening of the initial structure that consists of a ligament network. The coarsening was achieved by surface diffusion of the more noble element atoms. This coarsening is known in the metallurgical literature as Ostwald ripening and occurs immediately after the process of dissolution.

2.3.2 Volume change during dealloying

Since significant composition and microstructure changes take place during dealloying, one may wonder what will happen to the physical dimension of precursor Au-Ag alloys when, usually, over 50 at% of their compositional atoms are dissolved. Possible dimensional changes of np-Au samples caused by the dealloying are important, since these changes affect the actual relative density, which is the ratio of density of porous materials to that of solid. The actual relative density is one of the most important parameters determining the mechanical properties of porous materials [52].

Parida *et al.* reported volume reduction up to 30% during electrochemical dealloying of bulk Au-Ag alloys [53]. They found that the volume contraction of np-Au was due to applied potentials as well as transferred charge Q. More shrinkage was seen with higher potentials and faster dealloying, and relative length change $\Delta l/l_0$ increased with increasing amount of the transferred charge Q. Figure 2.5 shows the correlations between length change and Q, as well as the half-time of dealloying $t_{1/2}$.

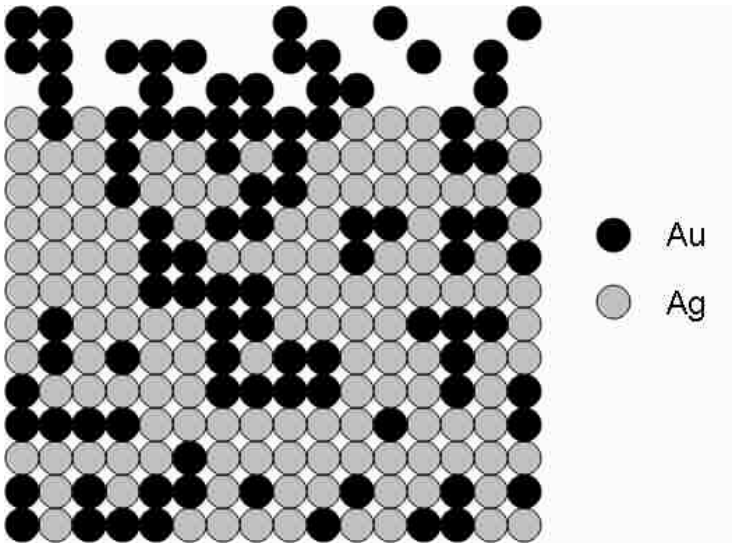

Figure 2.3 Two dimensional schematic of percolation model. Continuous connected clusters of the Ag atoms are asse to exist, in order for dissolution of Ag atoms from the bulk solid to occur, and also to prevent passivation by Au atoms. Figure adapted from the following literature: Dursun, A., *Nanoposity formation in Ag-Au alloys.* Ph. D. Dissertation, 2003. Copyright of Dursun, A.

Parida *et al*. proposed [53] that surface stress-induced compressive yielding, played an important role in these dimensional changes. However, it was thought to be effective only in ligaments with diameters of several nanometers or less, and therefore was a transient state during ligament coarsening. The authors attributed the volume shrinkage during dealloying to plastic deformation, which requires a mechanism for the nucleation of dislocations. Formation of the large number of dislocations required to explain the high amount of shrinkage was thought to be the result of collapse of sufficiently small pores. However, Crowson *et al.* studied geometric changes in nanoporous metals by simulations and found that surface relaxation is the main cause of the dimensional variations after selective dissolution [54].

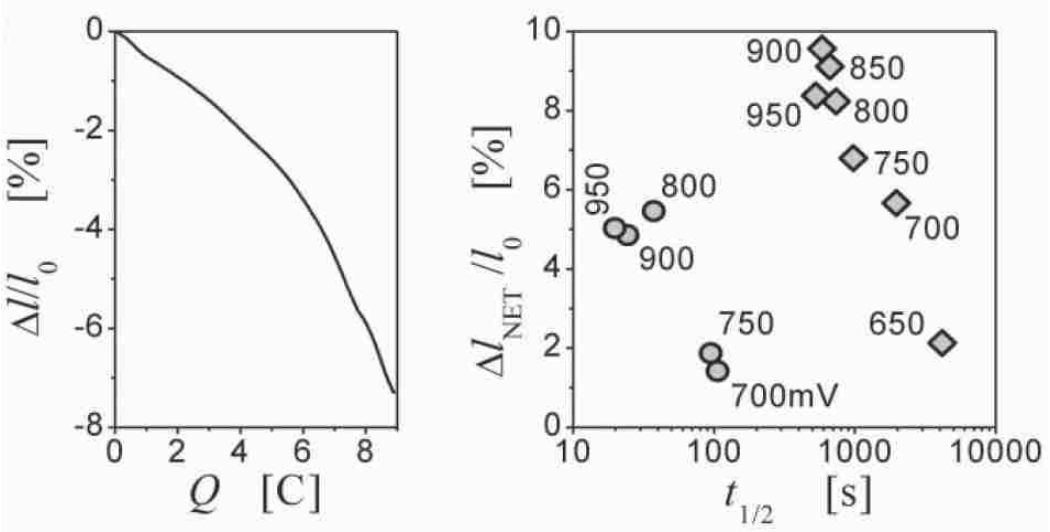

Figure 2.4 *In situ* dilatometry traces for a 0.9 mm^3 bulk $Ag_{75}Au_{25}$ cube showing the relative length change $\Delta l/l_0$ versus transferred charge Q at dealloying potential 850 mV versus Ag/AgCl (left). The plot at right shows the net length change after completion of dealloying versus the half-time of dealloying for bulk (♦) and 11 carat leaf (●) samples. Applied potentials are labeled beside data points. Reprinted figure with permission from Parida, S., et al., Physical Review Letters, **97**(3): p. 035504, 2006. Copyright (2006) by the American Physical Society.

2.3.3 Crack formation during dealloying

Crack formation generally occurs during dealloying of binary alloys [11, 55, 56]. A better understanding of the underlying mechanism of cracking and its prevention is important because the mechanical integrity of nanoporous metals is vital for their application. One reason for cracking could be the volume contraction that typically accompanies dealloying. As mentioned above, nanoporous metals shrink more when applied potential is higher, therefore causing faster dissolution of less noble elements [53]. Recently, Sun *et al.* developed a two-step dealloying method to make np-Au with no volume change or cracking [57]. These results support the hypothesis that volume shrinkage is responsible for the crack formation: Au-Ag alloys dealloyed by concentrated HNO_3 were found to have extensive cracks, but when etched first by diluted HNO_3 and then by concentrated HNO_3, they exhibited almost no cracking nor volume change.

Senior and Newman investigated the effects of Au content in the precursor alloy, applied potential, and temperature of electrolyte on the integrity of dealloyed np-Au foils [58]. Ag-23 at.% Au showed extensive intergranular and transgranular cracks when it was dealloyed at 20 °C and 1.1 V for 30 s. When the potential was lowered to 1.0 V and the dealloying time to extended 120 s (to achieve a similar thickness of dealloyed layer), the amount of cracks was significantly reduced and all cracks were along grain boundaries of the precursor alloy. The best results were achieved with 920 mV applied potential and 60 °C electrolyte temperature. Under this condition, a dealloyed layer ~4.6 μm thick and showing no visible surface cracking was obtained. There are two factors accounting for the results. First, internal tensile stress generated by dealloying facilitates crack formation. This tensile stress will be mitigated by reducing the dealloying potential and increasing the temperature. Second, Au oxidation was prevented when the applied potential was lowered below a threshold (above which reversible monolayer oxidation of Au occurred). The oxidation of Au reduces surface diffusion, thus hindering the relaxation of internal tensile stress induced by dealloying. The oxidation also reduced ligament coarsening so that structures with finer ligaments/pores have an increasing tendency toward brittleness.

2.4 Methods to tune the microstructure of np-Au

There are three methods to tune the ligament size of np-Au: (1) varying dealloying conditions such as external potential, types of electrolyte, and dealloying time; (2) pre-dealloying processes such as cold working and annealing of precursor alloys; (3) post-dealloying annealing.

It is known that different electrolytes lead to different ligament morphologies and length scales (see Table 2.1). Pre-dealloying processing, such as cold rolling, also plays a role in determining the ligament size after dealloying. Cold work may cause residual stress which will contribute to an increase in Ostwald ripening of the ligaments [11]. In other words, samples will have larger ligament size if cold work is performed before dealloying. Pre-dealloying annealing, on the other hand, results in finer pore size, which is attributed to a reduction in phase inhomogeneities during dealloying [12]. The

influence of dealloying conditions and pre-dealloying process on ligament size is summarized in Table 2.1.

Post-dealloying annealing has been an effective way to tune the length scale of np-Au. The underlying mechanisms of ligament coarsening by annealing were not fully understood, but Ostwald ripening is one possibility that has been proposed in several papers [11, 50, 59, 60].

Table 2.1 Literature survey of dealloying conditions and resulting ligament size.

Alloy composition (at.%)		Pre-processing before dealloying	Electro-lyte	Potential (V)	Liga-ment size (nm)	Refer-ence
Bulk	Au0.25Ag0.75	Rolled to 0.2 mm, annealed in air at 850°C for 3 h	1 M perchloric	1 V	15	[55]
	Au0.25Ag0.75 Au leaf: Au0.2Ag0.8, Au0.33Ag0.77	Annealed at 850°C 100 h, rolled to 1 mm sheet and cut into 1mm cubes, and annealed for 3 h at 850°C	1 M perchloric	650 mV to 900 mV	4 - 20	[53]
	Au0.2Ag0.8, Au0.23Ag0.77, Au0.28Ag0.72	10 mm × 2.5 mm, cold-rolled 100 µm thick, 975°C for 1h in H_2, rapidly cooled, no further processing	0.77 M $HClO_4$	0.92V, 1.0 V and 1.1 V for 20, 23, and 28 at% Au respecively	N/A	[58]
	Au0.42Ag0.58	Arc-melting AuAg, annealing at 900°C for 100 h, cut 0.5 mm thick disk, heat treat 8 h at 800°C, polished one side	75% HNO_3	1 V by potentiostat for 2 – 3 days	100	[61]
	Au0.25Ag0.75, Au0.3Ag0.7	Disk-shaped samples with diameter of ~5 mm and thickness of ~300 µm	1 M HNO_3 + 0.01 M $AgNO_3$	1 V vs. Ag pesudoreference electrode; *also free corrosion*	10 - 50	[62]
	Au at.% = 20, 25, 30, 35, 42	AuAg melted at 1100°C, then 100 h at 875°C with Ar, then cut to Ø = 5 mm, 300 µm thick, then 8 h at 800°C	1 M HNO_3 + 0.01 M $AgNO_3$	Potentialstat 600 mV to 900 mV; *also free corrosion*	20 - 100	[60]
	Au0.24Ag0.76	AuAg melted at 1100°C for 1h, then 200 h at 900°C, then cut to 2 mm × 2mm × 30 mm, then 24 h at 900°C	1 M $HClO_4$	1 V vs. calomel reference (HgCl) for 12 h	~20	[63]
	Au0.3Ag0.7	5 mm × 8 mm × 0.2 mm	0.1 M HNO_3	Three-electrode electrochemical cell 42 h	5	[64]
	Au0.3Ag0.7	0.2 mm thick	0.1 M $HClO_4$	1.1 V for 18 h	10	[56]
Thin film	12 carat Au leaf (35at.% Au)	100 nm or 1µm Au leaves	Concentrated HNO_3 1h	None	~22	[65]
	Au0.3Ag0.7	750 nm film	65% HNO_3 at 95°C 10 min	None	N/A	[66]
	Au0.4Ag0.6	800 nm film	65% HNO_3 at 95°C 1h for blanket film and 10 min for free-standing	None	~50 – 80	[67]
	Au0.37Ag0.63	150 nm 12 carat white Au leaf	70% HNO_3 16 M for 45 min	None	20 – 40 nm	[68]
	Au0.35Ag0.65	100 nm white Au leaf	0.1 M $AgNO_3$	~1.4 – 2.0 V vs NHE	~5 nm	[69]

2.5 Mechanical properties of nanoporous Au

Although one study of the mechanical properties of np-Au was first published 16 years ago [63], most research on this material has focused on its synthesis, structure, and mechanisms of microstructural evolution. Recently, several studies have concentrated on deformation mechanisms and ligament strength of np-Au [55, 60, 61, 66, 68, 70, 71], and this area appears to be gaining research attention. One puzzling finding is that although np-Au appears fragile and weak macroscopically, the strength of a single ligament may be very high when taking into account the high porosity of the material. Another interesting finding is that np-Au shows a size effect of its ligament width on its mechanical properties. By far, nanoindentation is the most frequently used method to test mechanical properties of np-Au, though the wafer curvature technique [67, 72] and bending tests were also used [63]. Furthermore, although nanoindentation has turned out to be an easy way to explore the compressive mechanical properties of np-Au [61, 62, 64], it is not clear that nanoindentation is the best approach to test np-Au, considering that the tip sizes of nanoindenters (a couple of hundred nanometers) are not much larger than the length scale of np-Au (a few to tens of nanometers). Along this line, microindentation may be a better method to evaluate the mechanical properties of np-Au, although reports on the mechanical properties of np-Au using microindentation are few in number.

2.5.1 Yield strength

Biener *et al.* [61] performed nanoindentation measurements on bulk np-Au and calculated the hardness of np-Au based on the ratio of the load and the projected indentation area. They found that the mean hardness (H) of np-Au was 145 (± 11) MPa. For porous metals, the yield strength σ is simply equal to the hardness, $\sigma = H$, due to the lack of Poisson expansion ($\nu = 0$ in this case). So the yield strength of np-Au is taken to be 145 MPa, accordingly.

The scaling laws of Gibson and Ashby [52] have been used extensively to compare the mechanical properties of solid materials and their porous counterparts. From the Gibson-Ashby scaling law, the yield strength of an open-cell foam is given by

$$\sigma_y = C_1 \sigma_s (\rho_{np}/\rho_s)^n \quad (2.1)$$

where σ_s and ρ_s are the yield strength and density of the solid materials, and ρ_{np} is the density of the porous counterpart. ρ_{np}/ρ_s is the relative density of porous materials. C_1 and n are empirical constants, with $C_1 = 0.3$ and $n = 3/2$ for many materials.

In the case of Biener's study above, the relative density of np-Au is 0.42 (also equal to the volume percentage of Au in the precursor alloy). σ_s is the macroscopic yield strength of pure Au and equals 200 MPa according to one literature value [73], although this is likely an upper limit to the yield strength of pure Au in bulk form. Therefore the yield strength of np-Au, according to the Gibson-Ashby scaling law, is $\sigma_y = C_1 \sigma_s (\rho_{np}/\rho_s)^n$ $= 0.3 \times (0.42)^{3/2} \times 200$ MPa $= 16.3$ MPa. So the yield strength of np-Au above, measured by nanoindentation (145 MPa), is ~10 times larger than predicted by Gibson-Ashby scaling laws [52]

On the other hand, we can use the yield strength of np-Au combined with the scaling law to calculate the equivalent bulk yield strength of solid Au. For the case of np-Au, this equivalent yield strength can be considered to be the yield strength of individual ligaments. Rearranging equation 2.1

$$\sigma_s = C_1^{-1} \sigma_y (\rho_{np}/\rho_s)^{-n} \quad (2.2)$$

the yield strength of ligaments were calculated to be $\sigma_s = (0.3)^{-1}$ 145 MPa $(0.42)^{-3/2} = 1.77$ GPa. These two equations are used frequently by other researchers as well as in this work.

Volkert *et al.* [55] performed uniaxial compression tests using nanoindenter on np-Au columns made by a focused ion beam (FIB). The stress-strain curves of np-Au columns show an elastic region and a yield point at ~100 MPa, followed by increasing flow stress with strain. All columns with different diameters display a high yield strength of 100 MPa for 15 nm diameter np-Au ligaments. Using equation 2.2 and a relative density of 36%, a yield strength of 1.5 GPa can be calculated for the 15 nm diameter ligaments.

2.5.2 Elastic modulus

The elastic modulus of np-Au can be calculated by the following equation using the indentation method:

$$\frac{1}{E_r} = \frac{(1-\nu^2)}{E} + \frac{(1-\nu_i^2)}{E_i} \tag{2.3}$$

where E_r is defined as a reduced modulus, E and v are Young's modulus and Poisson's ratio for the specimen, and E_i and v_i are the same parameters for the indenter [74]. The reduced elastic modulus E_r can be obtained from the unloading portion of indentation curves using the equation

$$E_r = \frac{\sqrt{\pi} \cdot S}{2 \cdot \beta \cdot \sqrt{A}} \tag{2.4}$$

where S is the slope of the initial part of the unloading curve, as shown in Figure 2.6, and β is the geometric factor of indenter tip.

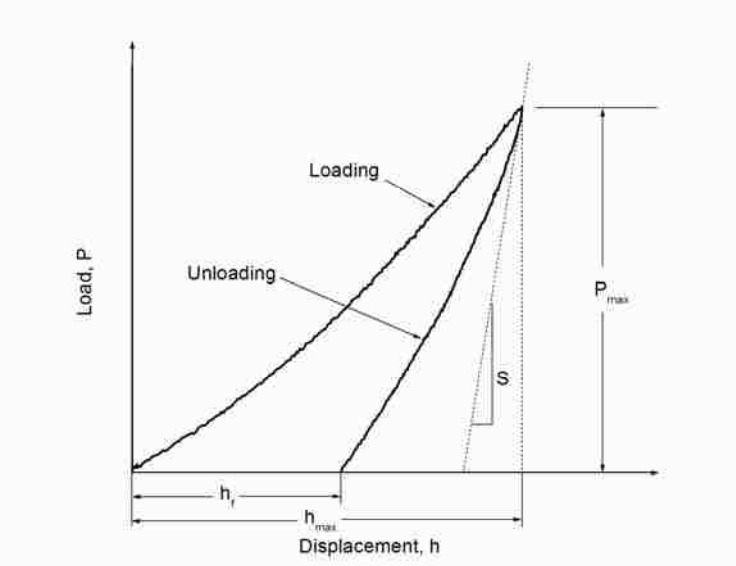

Figure 2.5 A typical load-displacement curve from indentation. *S* is the slope of the initial part of the unloading curve and can be used for calculating the elastic modulus of the material. Figure adapted from: Oliver, W.C. and G.M. Pharr, *An Improved Technique for Determining Hardness and Elastic-Modulus Using Load and Displacement Sensing Indentation Experiments*. Journal of Materials Research, 1992. **7**(6): p. 1564-1583. Copyright of 1992 by Materials Research Society.

Similar to the yield strength of porous materials, there is a Gibson-Ashby scaling law that relates elastic moduli of porous materials to those of their solid counterparts:

$$E = C_2 E_s (\rho_{np}/\rho_s)^n \tag{2.5}$$

where $C_2 = 1$, $n = 2$, ρ_{np}/ρ_s is the relative density of the porous material, and E and E_s are the elastic moduli of porous and solid materials, respectively.

Biener *et al.* [61] used the nanoindentation method and calculated the Young's modulus of np-Au to be 11.1 (± 0.9) GPa. Also, Volker *et al.* [55] determined Young's modulus of np-Au to range from 7 GPa at 2% to 12 GPa at 36% plastic strain using compression tests on np-Au columns. These values are in good agreement with the Young's modulus of np-Au scaled by equation 2.5 using a Young's modulus for single crystal Au of 57-85 GPa.

2.5.3 Mechanical test methods

A variety of mechanical test techniques have been used to explore the mechanical properties of np-Au. 1) ***Three-point bending***. Li and Sieradzki [63] used the traditional three-point bending method to test np-Au beams and obtained load-displacement curves of np-Au with various ligament sizes. 2) ***Nanoindentation***. Nanoindentation has been used by many researchers [61, 64, 67, 68] to explore the compressive strength and Young's modulus using the methods discussed above. 3) ***Compression***. Compression testing of np-Au is actually a variant of indentation. Volkert *et al.* [55] made np-Au pillars by FIB and performed compression on np-Au columns using a nanoindenter with a diamond punch having a flat end. 4) ***Wafer curvature***. Seker *et al.* [67] investigated mechanical properties of nanoporous Au by wafer curvature and nanoindentation.

Table 2.2 Summary of mechanical properties of np-Au and measurement techniques.

Np-Au specimen	Ligament size (nm)	Yield strength (MPa)	Elastic modulus (GPa)	Residual stress (MPa)	Technique used	Refer-ence
Bulk ($Au_{0.42}Ag_{0.58}$)	100	145	11.1	–	Nanoindentaion	[61]
Bulk ($Au_{0.3}Ag_{0.7}$)	5 – 126	990 – 520	–	–	Nanoindentaion	[64]
Bulk ($Au_{0.25}Ag_{0.75}$)	15	100	7 – 12	–	Compression	[55]
800 nm thin film ($Au_{0.4}Ag_{0.6}$)	~70	–	~17	21	Wafer curvature	[67]
100 nm leaf ($Au_{0.35}Ag_{0.65}$)	3 – 40	–	40 – 5	–	Buckling-based method	[75]
100 nm free standing film ($Au_{0.374}Ag_{0.626}$)	20 – 40	110	9	65	Deflective tensile testing / Nanoindentaion	[68]

2.6 Np-Au: Size effects on mechanical properties

It has been well established that the size of ligaments or pores of np-Au can be tuned by two methods: varying dealloying conditions, such as dealloying time and concentration of electrolyte, and annealing. So it is of interest to know how the mechanical behavior changes with variations in ligament size.

Biener *et al.* [62] investigated the mechanical properties of np-Au with various ligament sizes by nanoindentation, column microcompression and molecular dynamics. They adjusted the ligament size of np-Au by increasing immersion time of np-Au in the dealloying electrolyte and found that the hardness and yield strength increased dramatically with decreasing ligament size.

Furthermore, Hodge *et al.* [60] calculated the yield strength of np-Au with different ligament sizes using equation 2.1, based on nanoindentation measurements. They found that the yield strength of ligaments followed a Hall-Petch-type law and the relationship between yield strength and ligament size could be expressed as

$$\sigma_s = (\sigma_0 + k_{Au} L^{-1/2}) \tag{2.6}$$

where σ_0 is related to the bulk material yield strength σ_s, and k_{Au} is a material constant that depicts the slope of the yield strength-ligament size curve (k has the units of MPa $nm^{1/2}$). Specifically, they obtained a relationship of $\sigma_s = 200 + 9821\ L^{-1/2}$ between the yield strength of ligaments (σ_s) and ligament size (L) in nm. Combining equation 2.3 and 2.1, they obtained a modified scaling equation

$$\sigma_y = C_1(\sigma_0 + k_{Au} L^{-1/2}) (\rho_{np}/\rho_s)^{3/2} \tag{2.7}$$

where k_{Au} is the Hall-Petch-type coefficient for the theoretical yield strength of Au (10 nm $\leq$ L $\leq$ 1 μm). When L >> 500 nm, $k_{Au} L^{-1/2}$ is negligible and equation 2.4 reduces to equation 2.1.

Hakamada *et al.* [64] performed a similar investigation of size effects of ligament size on the yield strength of np-Au. The method they used is similar to Biener *et al.*: annealing np-Au to achieve various ligament sizes and using nanoindentation to explore the mechanical properties. They found that the yield strength of the Au ligaments varied with ligament size according to

$$\sigma_s = K L^{-0.2} \tag{2.8}$$

where L is the ligament size and K is a proportionality constant. It should be noted that the strength values claimed by Hakamada *et al.* are exceedingly high (up to ~1 GPa), resulting in equivalent bulk yield strengths up to 20 GPa. This is far above the theoretical strength of Au, indicating that the Gibson-Ashby scaling laws or nanoindentation testing (or both) may not be appropriate for measuring the mechanical behavior of np-Au.

Mathur and Erlebacher [75] investigated Young's modulus of np-Au by a bucking-based method. They tested a stiff thin film adhered to a thick compliant substrate. When the film and substrate were subjected to a compressive strain, buckling of the film occurred, in order to balance the energy for bending the film and that required to deform the substrate. They used dealloyed free-standing np-Au leaves and "mounted" the leaves on polydimethylsiloxane (PDMS) by simply catching them form below and lifting them off the surface of the water. By measuring the buckling wavelength λ, the effective Young's modulus E_f of the film can be calculated by

$$\frac{E_f}{(1-\nu_f^{\,2})} = \frac{3E_s}{(1-\nu_s^{\,2})}\left(\frac{\lambda}{2\pi h}\right)^3 \tag{2.9}$$

where h is film thickness, v is Poisson's rations, E is elastic modulus and subscripts f and s designate film and substrate, respectively.

They found that the effective Young's modulus of np-Au leaf increase dramatically with decreasing ligament size. Np-Au leaf modulus is found to be 6 GPa for 20 nm ligament size and 12 GPa for 12 nm ligaments. When ligament size falls to 6 nm, the modulus increases rapidly to 27 GPa and goes up to 40 GPa for 3 nm ligaments.

There several possible explanations for the size effects of mechanical properties of np-Au. (1) ***Dislocation absence***. It was suggested that dislocations are absent in ligaments of the order of 10 nm in diameter or smaller, assuming an initial dislocation density of ~10^6 cm^{-2}. The larger the ligament width, the more the dislocation source can be accommodated and the lower the stress to activate dislocation sources for deformation. (2) ***Dislocation interaction***. The interaction between dislocations (if any) and dislocation pile ups, as well as high dislocation densities are also possibilities to explain the high strength of np-Au. Other explanations include surface stresses and structural considerations for np-Au [75]. In the case of Mathur and Erlechacher's study of modulus

in np-Au leaf on PDMS, np-Au ligaments are regarded as beams. The finer np-Au leaf, with a large number of thin beams, has a greater moment of inertia than coarse np-Au leaf with fewer but thicker beams. So the finer np-Au leaf is stiffer than the coarse leaf, which explains the higher Young's modulus of np-Au leaf with smaller ligament size.

2.7 Deformation/failure behavior of np-Au

2.7.1 Macroscopic brittleness and microscopic ductility

Li *et al.* [63] analyzed the failure behavior of nanoporous Au beams with various ligament sizes using a three-point bending method, and reported a sample-size-driven ductile-brittle transition in np-Au. They investigated the load-displacement (P-δ) curves of np-Au via three-point bending test and evaluated scaled fracture strains e_f against the scaled sample size $Ł$. The determined the following relationships

$$Ł = L / (A/N)^{0.5} \tag{2.10}$$

$$\Delta_f = \delta_f / (A/N)^{0.5} \tag{2.11}$$

$$e_f = \Delta_f / Ł \tag{2.12}$$

where L is the width of the beam in μm, $(A/N)^{0.5}$ is the average cell size in μm, where A is unit area and N is the number of voids in A, δ_f is the load point displacement at fracture. One important finding is the fracture strains e_f at small $Ł$ are large, which indicates ductile behavior, whereas the fracture strains at large $Ł$ are small, which is more typical of brittle behavior. Thus the authors concluded that np-Au exhibited a ductile-brittle transition, which was controlled by the microstructural length scale controlled. They also concluded that this transition may be quite universal with respect to the exact nature of the constitutive behavior of the individual ligaments in the random structure as compared to the overall sample geometry.

The results of this paper can also be interpreted essentially through ligament size dependence. The parameter $Ł$ represents the cell size or ligament size of the nanoporous structure, assuming that the sample size L is the same for all samples. The fracture strains e_f in fact reflect δ_f, the load point displacement at fracture, when combining equations (2.10) – (2.12). So the fracture strains are large when ligament size is small, whereas the fracture strains are small with coarser ligaments. The conclusion can therefore be

expressed in another, more practical form, namely that the deformation behavior of np-Au changes from brittle to ductile as ligament or cell size increases with respect to the overall sample dimensions.

Biener *et al.* [59] investigated the failure behavior of np-Au by observing fractured np-Au with electron microscopy. Specimens of np-Au were manually bent to fracture using a three-point bending setup. There was no sign of plastic deformation prior to failure, which indicates brittle fracture of np-Au macroscopically. Closer observation of indentation induced cracking revealed that some ligaments bridging the cracks were strained by as much as 200%. Prominent necking prior to failure was also observed for ligaments in the area of large cracks. These observations indicate that microscopically, np-Au is a very ductile material, despite its evident macroscopic brittleness. Furthermore, more plastic deformation was observed in annealed np-Au. Elongation of cell structure and slip bands in ligaments were detected after deformation of the annealed samples. It was proposed that the annealing process allowed sufficient diffusion to eliminate defects that would serve as crack nucleation sites.

2.8 Other properties of np-Au

Dixon *et al.* [76] investigated the physical properties of np-Au, including surface area and optical response. Au-Ag alloy films were sputtered directly on a Quartz crystal microbalance (QCM) face and then dealloyed to make np-Au. Using a measurement system consisting of a phase-locked loop with a frequency generator and a lock-in amplifier, various pressures of nitrogen gas were admitted to the system. By converting the frequency shift, which was a function of the N_2 pressure, the adsorbed mass per active electrode area can be acquired. They found that for the same etch times, thicker films tend to produce higher surface area. Due to coarsening of np-Au at longer dealloying times, the surface area of np-Au decreased after further dealloying.

Optical properties of np-Au were measured with spectroscopic ellipsometry (SE). Two Stokes parameters, Δ and Ψ, were measured versus wavelength. Spectra were analyzed using comparisons with simulations based on a three-layer. Spectra were compared for various etching times and annealing temperatures as well as film thicknesses. There was an interband transition feature at ~500 nm wavelength for the

pure Au film. While the 40 nm np-Au film exhibited the similar features compared to the solid Au film, the 80 nm np-Au showed no visible features. As thickness increased to 160 and 400 nm, a new optical feature was observed in the ~500 nm wavelength region. This feature was thought to be a result of surface plasmon (SP) polariton resonance. Also, with longer dealloying time, critical features responsible for the SP resonance decreased.

Qian *et al.* [77] investigated the surface enhanced raman scattering (SERS) of np-Au with different pore sizes. They found that np-Au could be a promising substrate for SERS application if its microstructure was tuned appropriately. Interestingly, they found a size effect of np-Au on SERS enhancement, i.e. the smaller the pore size the stronger the SERS enhancement. Nonetheless, strong SERS enhancement was also observed in annealed np-Au samples with a large pore size of ~350 nm. By examining the morphology of annealed samples with SEM, the authors made a conclusion that the anomalous enhancement was caused by surface irregularities on the rough Au surfaces.

Chapter 3

Experimental

3.1 Bulk Alloy preparation

3.1.1 Bulk Au-Ag specimens

Bulk Au-Ag alloy "pellets" (cut from alloy wires containing 25at% and 30at% Au) were purchased from the Kurt J. Lesker Company and cut into ~4 mm × 4 mm plates with ~0.5 mm thickness using a diamond saw. These specimens were annealed at 850˚C for 100 hours to relieve residual stresses from cutting and to ensure a consistent grain size. Top and bottom surfaces of specimens were ground by Leco 800 grit and 1200 fine grit abrasive grinding paper. After each step, specimens were rinsed thoroughly and the grinding direction was changed by 90°. After grinding, Leco 1 μm diamond polishing suspension combined with a TexMet 2500 polishing cloth from Buehler were used to polish the specimens. The final step employed a Buehler Mastertex polishing cloth with Buehler MasterPrep 0.05 μm Al_2O_3 suspension. Some specimens were rolled perpendicular to the wire axis in order to increase cold working before dealloying, to improve residual stress that may contribute to an increase in Ostwald ripening of the ligaments [11].

3.1.2 Electrochemical dealloying

In order to produce the nanoporous samples, external potentials of 0.33 - 1.0 V were applied to annealed Au-Ag bulk alloy, using a platinum wire as a counter electrode. A simple galvanostatic electrochemical cell (Extech Dual Tracking DC Power Supply 382285) was used, similar to that of Rösler et al. [78], where potential was provided by a voltage supply instead of a potentiostat. The schematic of the setup for the dealloying experiment is shown in Figure 3.1. Stainless steel mesh was used to hold the Au-Ag sample in the electrolyte. An amperemeter with a scale up to 1.0 mA was used to monitor the current flow during dealloying and generally, the current was tuned below 1 mA by adjusting the voltage. Some samples were dealloyed in concentrated HNO_3 for 2-3 days. For other samples, dealloying was performed in multiple stages and with varying

concentration of the etchant. For the multiple-stage dealloying, a 1:2 diluted acid solution [30 ml HNO_3 (70% stock solution) mixed with 60 ml distilled H_2O] was used as the electrolyte. After dealloying with the 1:2 acid solution for up to 70 hours, the electrolyte was changed to stock (70%) nitric acid and dealloying continued for 10 more hours.

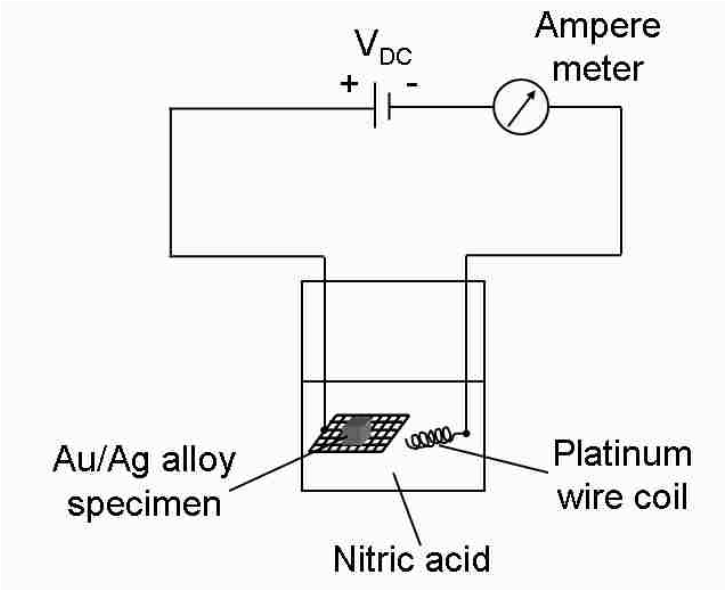

Figure 3.1 Schematic of setup for dealloying experiments. A DC voltage supply was used to provide external potential for Ag removal. Au-Ag alloys were placed on a stainless steel mesh. A platinum wire coil served as the counter auxiliary electrode and nitric acid as the electrolyte.

3.1.3 Microindentation

Microindentation was used to measure the compressive mechanical properties of np-Au. The basic principal is using a sharp diamond tip (Vickers) to press into the flat sample surface. Based on the applied load was used and the residual imprint area of indents after indentation, the hardness can be obtained by the equation:

$$H = \frac{P_{\max}}{A} \tag{3.1}$$

where $P_{\max}$ is the peak indentation load and A is the projected area of the hardness impression. The Young's modulus is calculated according to

$$E = \frac{\sqrt{\pi} \cdot S}{2 \cdot \beta \cdot \sqrt{A}} \tag{3.2}$$

where E is Young's modulus, S is the slope of unloading curve (using the Oliver and Pharr method) and β is a geometric factor (for square diamond tip, β = 1.012 here). Microindentation tests were performed on both as-dealloyed and annealed samples, using a Micro-hardness Tester (CSM Instruments, Switzerland) fitted with a Vickers indenter. Both loading time and unloading time were 30 seconds, without an intermediate pause. Diagonal lengths of the indents were measured with an optical microscope (Olympus BX41) to calculate the hardness of np-Au.

3.2 Thin film Au-Ag samples

3.2.1 Sputtering

Sputtering is a method by which surface material is removed due to ion bombardment. The simplest method for generating the positive ions necessary for sputtering is establishing a glow discharge. An electric field is produced between the substrate and target. Free electrons are accelerated by the electric field and acquire sufficient energy to ionize the gas atoms (usually is Argon). Ionized gas atoms (ions) in the chamber strike the target materials, resulting in the ejection of the target atoms. Target atoms deposit onto anodic substrates and form films with different thickness depending on the sputtering rate. Sputtering can be divided into DC sputtering and RF sputtering (according to the power supply). For DC sputter deposition with a parallel-plate discharge, the power supply is simply a high-voltage DC source. The sputtering target is the cathode of the discharge and the substrate and/or the vacuum chamber walls serve as the anode. The pressure of the gas used is on the order of several millitorr. The main difference between DC and RF sputtering is that for RF the power supply is a high voltage RF source. RF sputtering has advantages over DC, for example, lower voltages, lower sputtering gas pressures required and higher deposition rates obtained. In addition, RF sputtering makes it possible to sputter an electrically insulating target. A significant advantage of sputtering is that multiple materials may be simultaneously deposited, no matter of the differences of partial pressure between components, which need to be

considered using electron beam physical vapor deposition (EBPVD). This allows precise control of both film thickness and composition when producing precursor alloy films.

Magnetron sputtering is a powerful and flexible technique which can be used to coat virtually any workpiece with a wide range of materials - any solid metal or alloy and a variety of compounds. During the sputter process a magnetic field can be used to trap secondary electrons close to the target. The magnetic field $\boldsymbol{B}$ is created to be parallel to the surface of the target and perpendicular to the electric field $\boldsymbol{E}$, which was mentioned above. There is a drift of the electrons in the $-\boldsymbol{E} \times \boldsymbol{B}$ direction. Superposed on this drift, the electrons follow helical or cyclodial paths around the magnetic field lines undergoing more ionizing collisions with neutral gas atoms near the target than would otherwise occur. This enhances the ionisation of the plasma near the target leading to a higher sputter rate. It also means that the plasma can be sustained at a lower pressure. The sputtered atoms are neutrally charged and so are unaffected by the magnetic trap.

In the present study, Au-Ag films (Au-65 or 70 at.% Ag) were magnetron sputtered at room temperature in a high vacuum chamber (AJA ORION system, base pressure better than 10^{-6} Pa) onto glass slides and 180 μm thick (100)-oriented silicon wafers (CrysTec GmbH, Germany) to thicknesses from 45 to 1000 nm. The Si substrates had previously been coated with 10 nm of amorphous silicon oxide (a-SiO_x) and 50 nm of amorphous silicon nitride (a-SiN_x). Prior to deposition of the Au-Ag alloy, a 10 nm Ta interlayer and a 10 nm Au interlayer were sequentially sputtered onto the wafer. From previous work, Ta was known to improve adhesion of Au films, and Au interlayers were known to improve adhesion and stability of np-Au after dealloying. This Au interlayer was visible in cross-section after annealing and was not consumed during ligament coarsening. The Au-Ag (70-75at.% Ag) precursor alloy films were deposited by co-sputtering Au and Ag targets (both 99.99% purity). Au and Ag targets were sputtered by RF and DC powers respectively. The detailed sputtering parameters are listed in Table 3.1. Prior to sputtering, a two-minute substrate biasing was performed using RF power supply with 35 W at 2.0 mtorr pressure.

Table 3.1 Parameters that were used for making Au-Ag films by the AJA sputtering system. Substrate biasing was performed prior to sputtering the interlayers to clean substrates. For all sputtering and biasing processes, a substrate height of 55 mm and substrate rotation of 50% were used.

Specimens		Au-Ag films (25 at.% Au)				Au-Ag films (30 at.% Au)			
Sputtering conditions		Power (W)	Pressure (10^{-3} torr)	Rate (nm/min)	Time (min)	Power (W)	Pressure (10^{-3} torr)	Rate (nm/min)	Time
Substrate biasing		RF/35	2.0	-	2	RF/35	2.0	-	2
Inter-layer	Ta	RF/75	2.0	3.33	3	RF/75	2.0	3.33	3
	Au	RF/50	2.0	10	1	RF/50	2.0	10	1
Alloy layer	Au	RF/50	2.0	7.06	*	RF/75	2.0	9	*
	Ag	DC/65	2.0	21.2	*	DC/60	2.0	21	*

* The sputtering time for the alloy layers vary according to film thickness.

3.2.2 Dealloying

As-sputtered thin film samples were dealloyed in concentrated HNO_3 (70% concentration) for various time and rinsed in ethanol. Sometimes electrochemical dealloying was performed to obtain lower residual Ag content.

3.2.3 Film thickness

Film thickness was measured by a Dektak profilometer. To make thickness difference on a smooth surface, straight lines were draw by a marker (Sharpie) on substrate surfaces. After sputtering thin films for certain thickness over these lines, specimens were merged into ethanol to dissolve the lines. Film over the straight lines became unstable and finally was also removed after the dissolution of the ink of the marker. A stylus profilometer was used to measure the film thickness. Figure 3.3 shows a result of film thickness measurement by the profilometer.

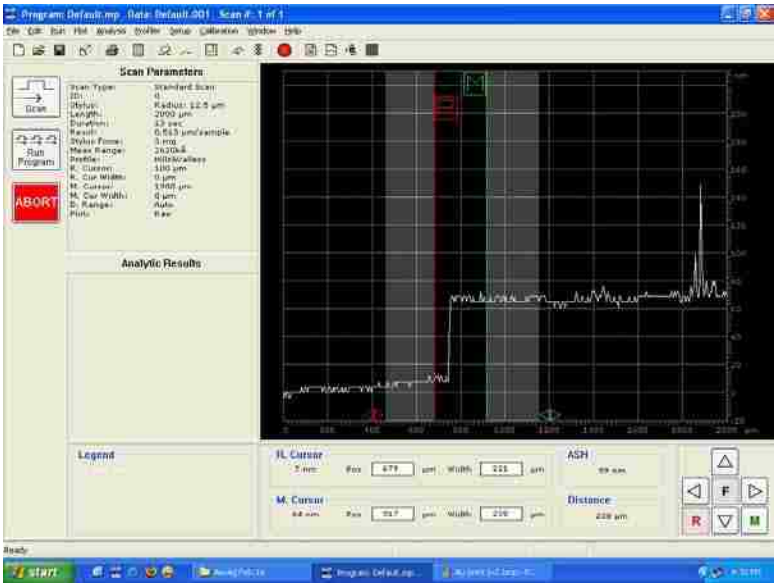

Figure 3.2 Thickness measurement of a np-Au film by the Dektak surface pofilometer. The sample was scanned by the stylus across a thickness step produced by lifting off films from the substrate in some area.

3.2.4 Wafer curvature

Stresses in films have significant influence on dislocation motion in materials and their mechanical properties. Stresses in films on substrates come principally from differing thermal expansion coefficients of film and substrate, as well as nonequilibrium growth processes.

Expression of the biaxial stress in a film is given by

$$\sigma_f = M_s \frac{h_s^2}{6h_f} K = M_s \frac{h_s^2}{6h_f R} \tag{3.3}$$

where K=1/R is the curvature of the substrate, M_s the biaxial elastic modulus of substrate, and h_f and h_s are thickness of film and substrate, respectively [79]. The most popular technique for measuring curvature changes associated with thin film stresses is laser scanning (Figure 3.4). The principle of laser scanning is that a beam of laser light reflects

off the surface of a curved substrate at an angle θ, which depends on the orientation of the surface. When the laser beam moves to a new position, the light reflects at a different angle if the substrate is curved. This causes the reflected beam to strike a different region on the photodetector, and the exact position is used to calculate the local substrate curvature. By comparison with the reference curvature of the bare substrate, the net curvature is calculated and the film stress is obtained from Stoney's equation (Equation 3.3).

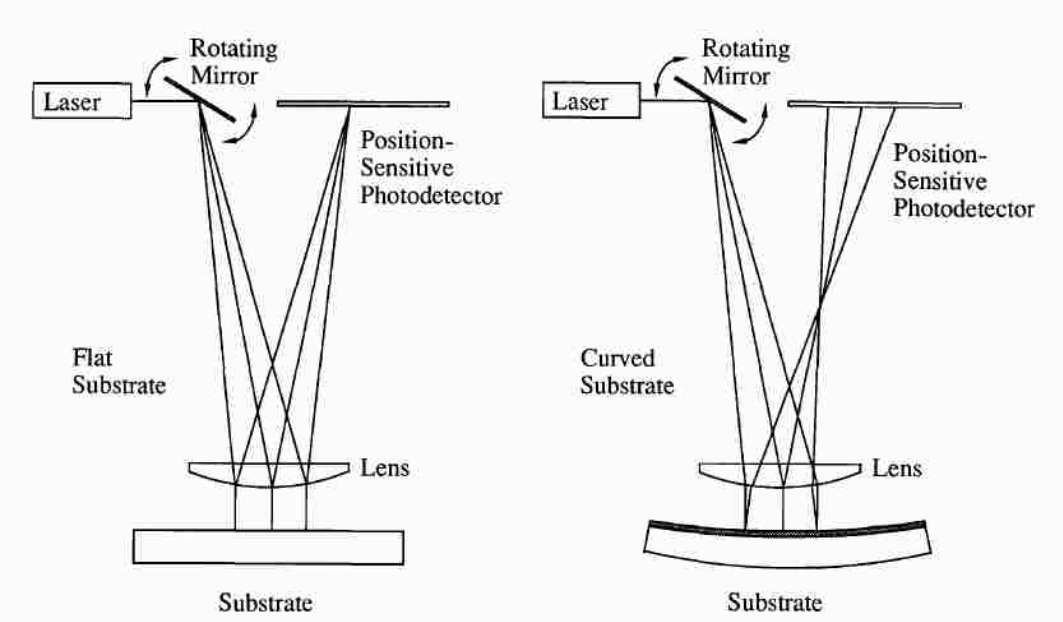

Figure 3.3 Schematic diagram of a laser scanning instrument used to measure substrate curvature and corresponding residual stress in films. Position change of the reflected laser beam caused by the change of the substrate curvature was measured by a position-sensitive photodetector and was used to determine the substrate curvature. Reprinted figure with kind permission of Springer Science and Business Media from Metallurgical Transaction A, **20**(11), 1989, 2217-2245, *Mechanical properties of thin films*, W. D. Nix, figure 18.

In the present research, stress in thin films was measured by a wafer curvature equipment (FLX-2320-S, Toho Technology Corporation). For stresses after dealloying, wafer curvature measurements were performed immediately following dealloying to

determine film stress. Diametric scans were taken at 15˚ intervals to generate a three-dimensional stress map and obtain an average stress value representative of the entire film. Figure 3.5 shows a sample of 3D stress map of a np-Au film after dealloying. The stress in the Ta and Au interlayers, measured separately with another sample, was subtracted from total stress measurements of np-Au samples to determine the stress in the np-Au layer only. Average stress from the stress maps was generally used, although the stress maps also provide the minimum and the maximum of the stresses across the wafers. For samples that need to explore their thermomechanical behavior, stress was measured along a certain angle, along which reference measurement of the substrate curvature was made. Samples were thermally cycled up to 500°C in flowing N_2 (1 cubic feet per hour) while stresses of the films were measured with certain time or temperature intervals. Both the complete wafer sample and smaller samples were thermally cycled in parallel, so that film microstructure could be characterized without damaging the wafer curvature sample.

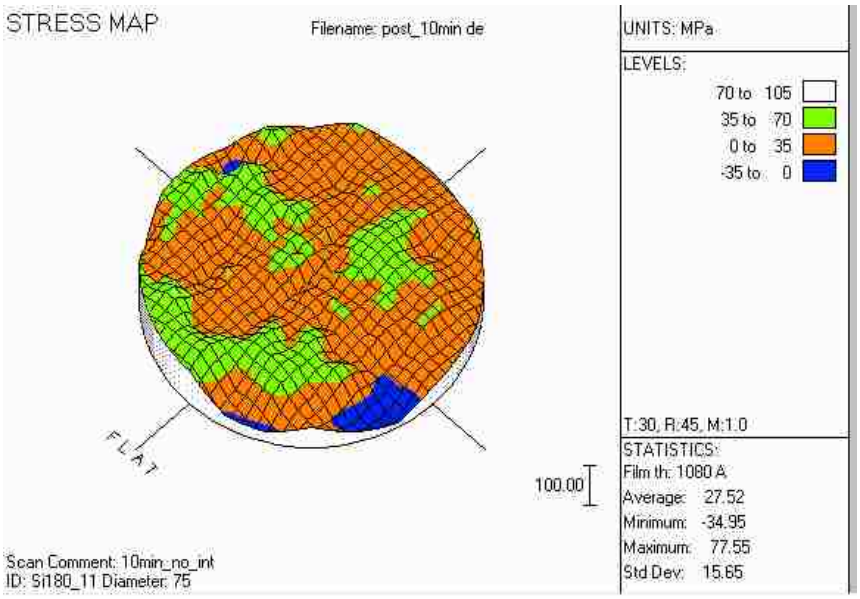

Figure 3.4 A three dimensional stress map of a 387 nm np-Au film (25 at% Au) generated by wafer curvature. The film was dealloyed for 10 min. Most of the area of the wafer shows tensile stress (green and brown) while a small fraction of area is compressive (blue area).

3.3 Characterization of np-Au

3.3.1 XRD

X-ray diffraction patterns were collected by a Siemens D500 X-ray diffractometer for np-Au samples before and after dealloying. The scan range is from 20° to 100° with scan rates of 0.1 – 4 °/min and step sizes of 0.01 – 0.5°. X-ray source is Cu K_α line, which has a wavelength of 1.541 Å. Au and Ag are both face-centered cubic (FCC) structure and lattice parameters between them are only slightly different (0.17%; Au: 4.079 Å and Ag: 4.086 Å [80]), so diffraction peaks from them will overlap almost completely throughout entire scan ranges. Using the Bragg equation combined with the structure-factor of FCC, peaks of Au-Ag alloy appeared in the diffraction patterns can be identified. A XRD pattern of a bulk Au-Ag alloy (25 at.% Au) is shown in Figure 3.6.

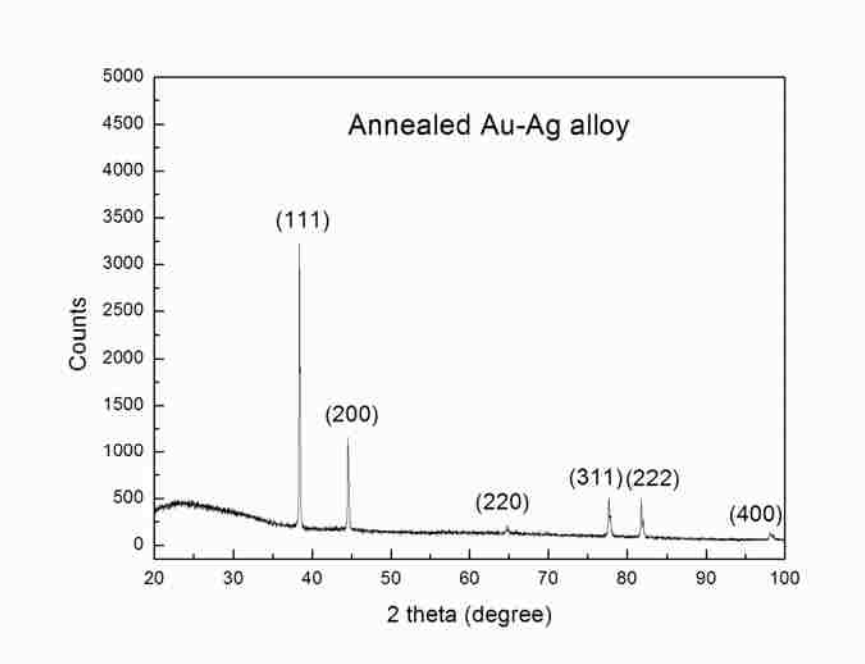

Figure 3.5 X-ray diffraction pattern of a Au-Ag alloy containing 25 at.% Au. The sample was annealed for 100 h at 850 °C to homogenize the internal microstructure. All peaks for FCC structure appeared.

3.3.2 SEM and EDS

Along with complete wafer samples, smaller Si pieces were coated with precursor alloy film and were used for making electron microscopy specimens. Samples were examined using scanning electron microscopy (SEM, Hitachi S900 and Hitachi S3200) and energy dispersive spectrometry (EDS, affiliated with the S3200). Sometimes cross-sectional view images were also taken under the S900.

Hitachi S900 and S3200 were used to observe the morphology of bulk sample surface as well as nanoporous Au structure under high magnification. For plan view, specimens were mounted on Cu or Al stubs using carbon paint and no coating was applied. The image quality is good enough. For cross-sectional view thin film samples, in addition to carbon paint, crystal bond adding carbon powder was used to help hold samples tight on substrate stubs. However, cross-sectional view image specimens still shifted slowly sometimes under SEM. To make cross-sectional view specimens, as-sputtered or dealloyed films were dipped into liquid nitrogen for several minutes and then broken immediately after they were lifted out of liquid nitrogen.

Evex EDS system affiliated with a SEM (Hitachi S3200) was used to analysis compositions of np-Au. A typical EDS result of a Au-Ag alloy is shown in Figure 3.7. Peaks of M_α of Au and L_α of Ag were used to calculate the ratio of Au and Ag. Usually, 60 seconds of collection time were used to collect x-ray signals. Five data points were measured for each specimen.

3.3.3 TEM

Transmission electron microscopy (TEM) was performed on a JEOL 2000FX. TEM specimens were made by dimpling the back side of the Si substrate combined with chemically etching the remaining Si. Figure 3.8 shows the schematic of making np-Au thin film specimens for TEM. First thin film specimens on Si substrate were cut to 3 mm diameter plates using an ultrasonic cutter. Then the plates were mounted to a quartz plug that fits into a Gatan dimpler using crystal bond with films side facing down. Back sides of the specimens were ground to a total thickness of about 75 μm using grinding papers. After grinding, the back sides of the Si substrate were dimpled away for further 60 μm using a Gatan dimpler with bronze wheels and Gatan paste. The finanl step of dimpling is

using felt wheels with 0.1 μm diamond paste (Leco) to remove the rest 15 μm of Si until transparency at the dimpling center is observed. The specimens (Si sides) were etched with a solution of HNO_3:HF:Acetic acid (2:1:1). The etching time is usually short, which was judged by associate observation using an optical microscopy. The a-SiNx layer acted as an etch stop, allowing the Au-Ag film to remain intact for TEM experiments (dealloying was performed after each TEM sample had been prepared). Then specimens were thoroughly rinsed with water and ready to observe under TEM.

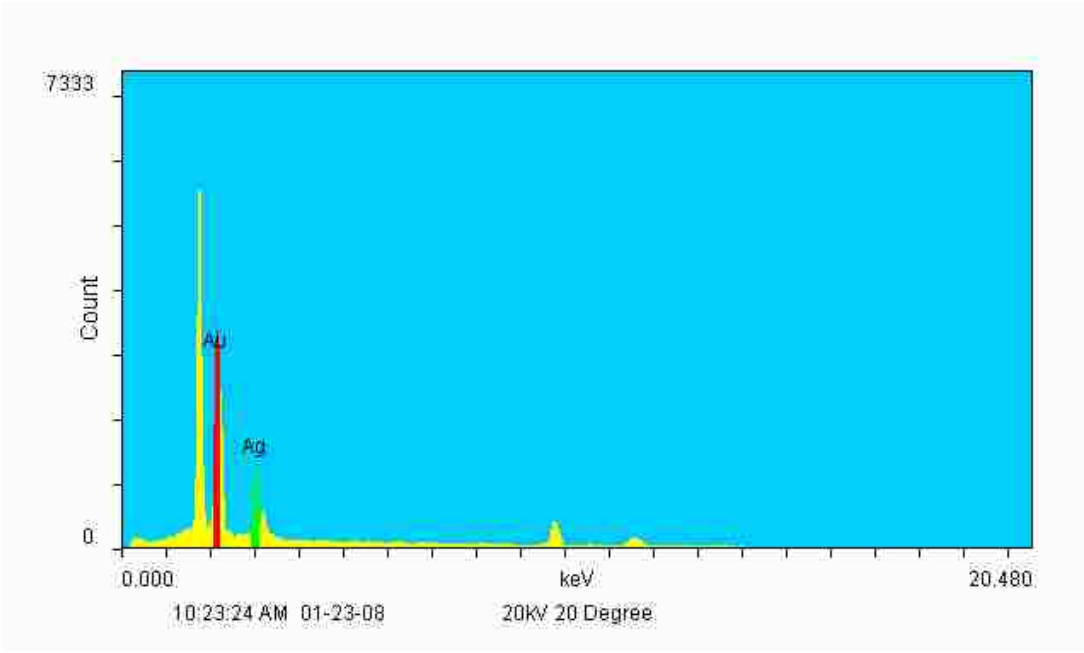

Figure 3.6 A typical EDS plot of a np-Au film measured by the Evex EDS system. The highest yellow peak at ~1.8 keV is from Si. Peaks of M_α of Au (red one) and L_α of Ag (green one) were used to calculate the ratio of Au and Ag.

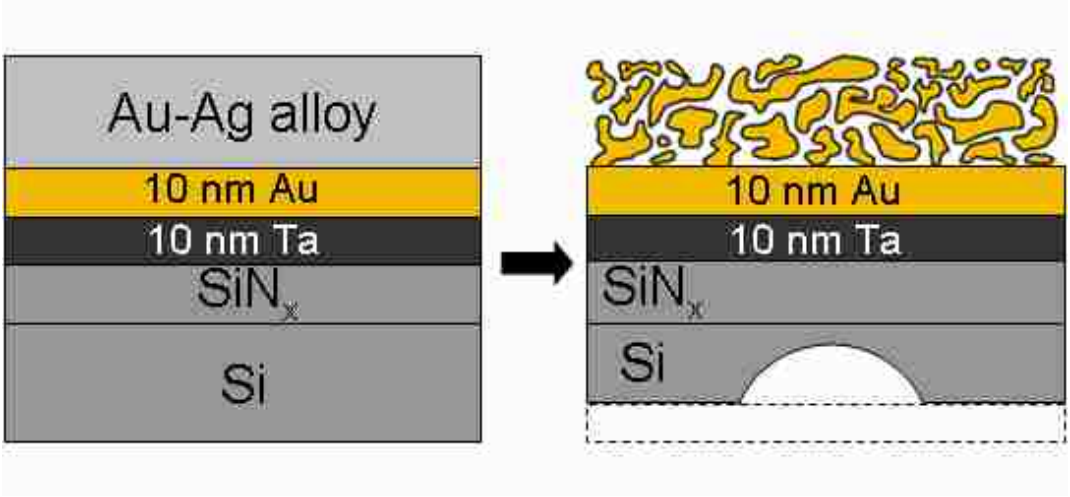

Figure 3.7 A schematic showing procedures making plan-view TEM specimens. The back sides of the Si substrate were ground to a total thickness of ~75 μm, and then dimpled to ~15 μm by bronze wheels and further dimpled by felt wheels until transparency at the dimpling center was obtained. The specimens were then etched with a solution of HNO_3:HF:Acetic acid (2:1:1). The a-SiNx layer acted as an etch stop, allowing the Au-Ag film to remain intact for TEM experiments (dealloying was performed after each TEM sample had been prepared).

3.3.4 *In situ* TEM

A series of Au-Ag alloy films were deposited on substrates in order to produce suitable np-Au films. For *in situ* nanoindentation experiments, 30 at.% Au-70 at.% Ag alloy films of various thickness were magnetron sputtered onto wedge-shaped silicon substrates that had been prepared using lithographic techniques [81]. *In situ* nanoindentation of dealloyed np-Au on Si wedges was performed with a Hysitron Picoindenter^{TM} inside a JEOL 3010 TEM. Figure 3.6 illustrates the sample geometry used for *in situ* nanoindentation. Here, a focused ion beam (FIB) image has been stretched into a perspective view and further altered to show the wedge shape of the specimen. The electron beam direction is oriented vertically downward in Figure 3.9, and the diamond tip moves to the left, making contact during indentation of the film on the ridge of the wedge. Depth of indentation was limited to approximately half the film thickness, and no effect of the Si substrate on the load-displacement curves was observed. The np-Au films,

with a relative density of ~36% [82], were able to absorb the imposed deformation by compacting without expanding laterally.

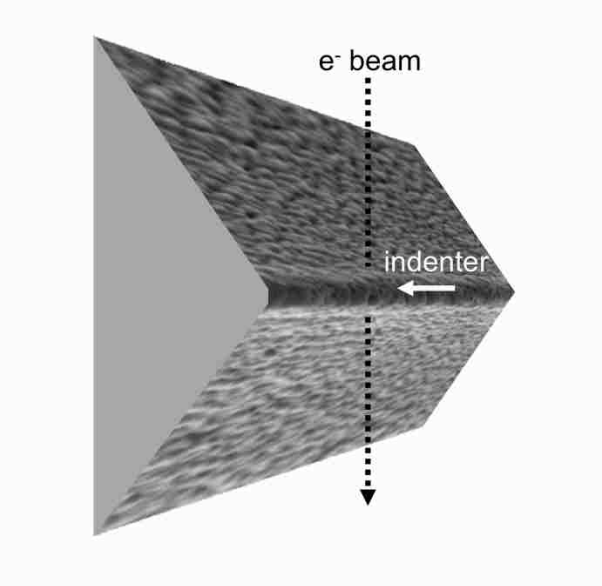

Figure 3.8 FIB image of np-Au on Si wedge sample, stretched into perspective view to provide a schematic illustration of the sample/indenter geometry for *in situ* nanoindentation. The electron beam direction is vertical, oriented perpendicular to the ridge of the Si wedge, and the direction of indentation is into the wedge. This 300 nm np-Au film was dealloyed for 30 min after deposition of the alloy film onto the Si wedge.

Chapter 4

Thermal and mechanical behavior of 25 at.% Au bulk nanoporous Au

4.1 Introduction

Nanoporous metals have been investigated extensively in recent years. Some of them have been found to have unique properties that do not exist in metals with ordinary form, such as dimensional changes upon applied voltage, a property that makes them potential candidates for actuators and sensors [26, 83]. Especially nanoporous Au (np-Au) has widespread potential applications, including biosensing, catalysis and ultracapacitance [31, 33, 37], due to its noble metal character, high resistance to oxidation and affinity for sulfur.

The prospects for application of np-Au have prompted efforts to better understand its mechanical properties, since mechanical integrity is important to product fabrication. Recently, the literature on mechanical properties of np-Au has expanded considerably, although the pioneering paper on mechanical properties of np-Au was published in the early 1990's [63]. Researchers at Lawrence Livermore National Laboratory (LLNL) have investigated the mechanical properties of bulk np-Au via nanoindentation and reported the size effect of ligaments on the yield strength of np-Au, as well as ductile (plastic) deformation behavior of np-Au under compressive stress [60-62]. It was also found by Volkert et al. that the yield strength of np-Au approaches the theoretical strength of Au [55, 62], which is a surprising result considering that over 60% of the material is pore/void. Size dependence of Young's modulus and yield strength was also reported by other researchers [64, 75]. Studies on the mechanical behavior of np-Au films were also performed by several groups [67, 68, 84, 85].

Nanoporous Au (np-Au) has been found to exhibit a size effect in mechanical properties, e.g. higher strength [62] and Young’s modulus [75] for samples with smaller ligament size. Various ligament sizes in np-Au can be achieved by simply annealing the samples [63] or varying the dealloying time [75]. In some instances, a finer ligament size or pore size is preferred in order to take advantage of the high surface-to-volume ratio of np-Au, especially at high temperatures.

Nanoindentation has been the most popular method for exploring the mechanical properties of np-Au [61, 62, 64]. However, the dimensions of nanoindenter tips are usually in the range of 100 – 200 nm and likely do not contact enough ligaments during indentation of np-Au (considering that the length scale of np-Au ligaments ranges from a few to tens of nanometers). On the other hand, microindenter tips generally have a dimension of several microns, enabling microindentation to produce a more average measurement of the mechanical properties of np-Au.

In this chapter, the mechanical properties of bulk np-Au were studied using the microindentation technique. Nanoporous Au specimens were fabricated by dealloying Au-Ag alloys with 25 at.% Au. Some samples were then annealed at various temperatures to obtain different ligament sizes. After dealloying and annealing at each temperature, specimens were tested by microindentation and characterized by scanning electron microscopy. It was found that significant agglomeration occurred when np-Au was annealed at 300°C or above. Hardness of the sample increased after annealing, while the average ligament diameter of bulk np-Au increased as well.

4.2 Results and discussion

The strength of porous materials depends on their structure, which is governed by the relative density (or porosity), the mean cell diameter and whether the cells are open or closed [52]. According to EDS results, less than 2 at.% Ag remained in the dealloyed samples studied here. Therefore the relative density of these np-Au samples is ~ 27%, asumming no volume shrinkage [53]. The mean cell diameter is calculated by combining the ligament width and pore diameter. In the present study, the mean cell sizes of np-Au after dealloying range from ~35 nm to ~50 nm. It is well accepted that nanoporous Au exhibits an open-cell porous structure, as verified in the current study.

Table 4.1 presents an overview of bulk np-Au samples and their processing methods. To reveal the influence of heat treatment on microstructure, the samples were annealed at 100°C to 600°C for 10 or 30 minutes, either using a sputtering system with a high vacuum environment or a wafer curvature system with flowing N_2. Ligament width was determined by measuring SEM micrographs taken after each process. Several hundred ligaments were measured for each sample.

Table 4.1 Overview of bulk np-Au samples made from 25 at.% Au-Ag alloys, as well as their dealloying and annealing conditions.

Samples	Dealloying method [a]	Annealing environment [b]	Note
Set A	EP	N_2/Air 10 min	1 sample annealed at 100°C, 200°C, 300°C, 400°C and 500°C consecutively, after dealloying
Set B	EV	N_2/Air 10 min	6 samples: one was not annealed; 5 others were annealed at 100°C, 200°C, 300°C, 400°C and 500°C
Set C	EV	HV 10 min	1 sample annealed at 300°C, 400°C, 500°C and 600°C consecutively, after dealloying
Set D	EV	HV 30 min	6 samples: 1 was not annealed; and 5 others were annealed at 200°C 300°C, 400°C, 500°C and 600°C

[a] EV denotes electrochemical dealloying by a direct current (DC) voltage supply with 1.0 V output; EP denotes electrochemical dealloying by a potentiostat with 1.0 V versus a Ag/AgCl reference electrode. In both cases, the total dealloying time was ~2 – 3 days.

[b] HV denotes high vacuum environment and N_2/Air denotes samples that were annealed in a flowing N_2 environment that contained trace amounts of ambient air.

Figure 4.1 shows the surface morphology of Au-Ag alloy after different dealloying times, as viewed under an optical microscope. Surface features such as twins and grain boundaries were retained at all dealloying stages including 1 minute and 50 hours. However, in contrast to the alloy and short-time dealloying stages, the surface of the 50-hour dealloyed sample was uneven and had a large number of cracks, as shown in Figure 4.1b. These cracks developed along grain boundaries (GBs). Crack formation is supposedly an inevitable by-product of dealloying of np-Au [11, 55, 86]. Based on our results, crack formation is more sensitive to the dealloying rate and/or electrolyte concentration during the initial stage of dealloying, which will be discussed in more detail in Chapter 5.

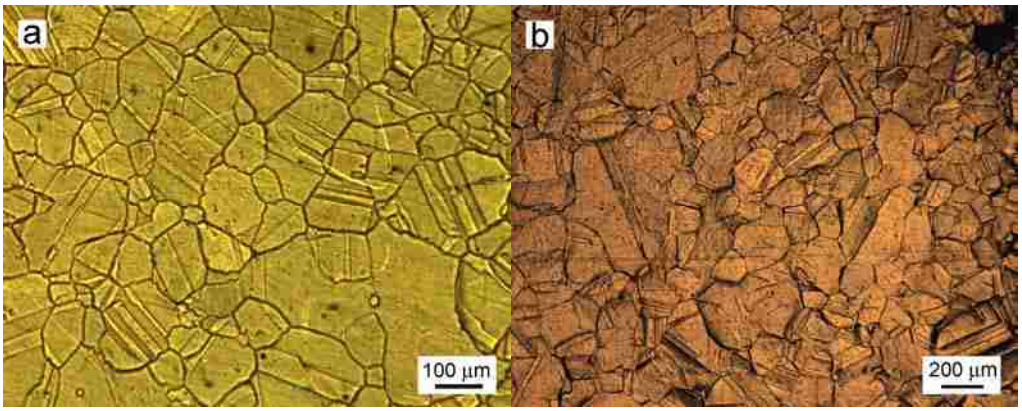

Figure 4.1 Optical images of bulk Au-Ag alloys (25 at.% Au) after electrochemical dealloying for various times. Electrochemical dealloying for (a) 5 minutes; (b) 50 hours. Grain boundaries and twins are the main features visible on the surfaces. Cracks became more severe during longer dealloying.

Figure 4.2 shows the microstructural evolution of sample set A, which was annealed in flowing N_2/air at a rate of 5 cubic feet per hour (CFH). Ligament size remained roughly the same up to 200°C annealing, and ligament coarsening began at ~300°C (Figure 4.2d). At 200°C, ligaments are still smooth but some parts have already begun to coarsen. At 300°C, ligaments became rougher and coarsening was more apparent. At 400°C, the ligaments coarsened to several hundred nanometers, and ligaments assumed an irregular shape, with some amount of apparent surface contamination. In addition to ligament coarsening, so-called fused grain boundaries, which are composed of solid continuous ligaments, began to appear at this temperature (see Figure 4.7; also see reference [57]). Finally, at 500°C the ligament size increases only marginally (compared to 400°C), and more fused grain boundaries were observed. Terrace-like features appeare on ligaments starting at 400°C, and become more apparent at 500°C. The surface contamination and irregular shape of ligaments, illustrated in Figures 4.2e-f, are most likely due to insufficient rinsing after dealloying [77].

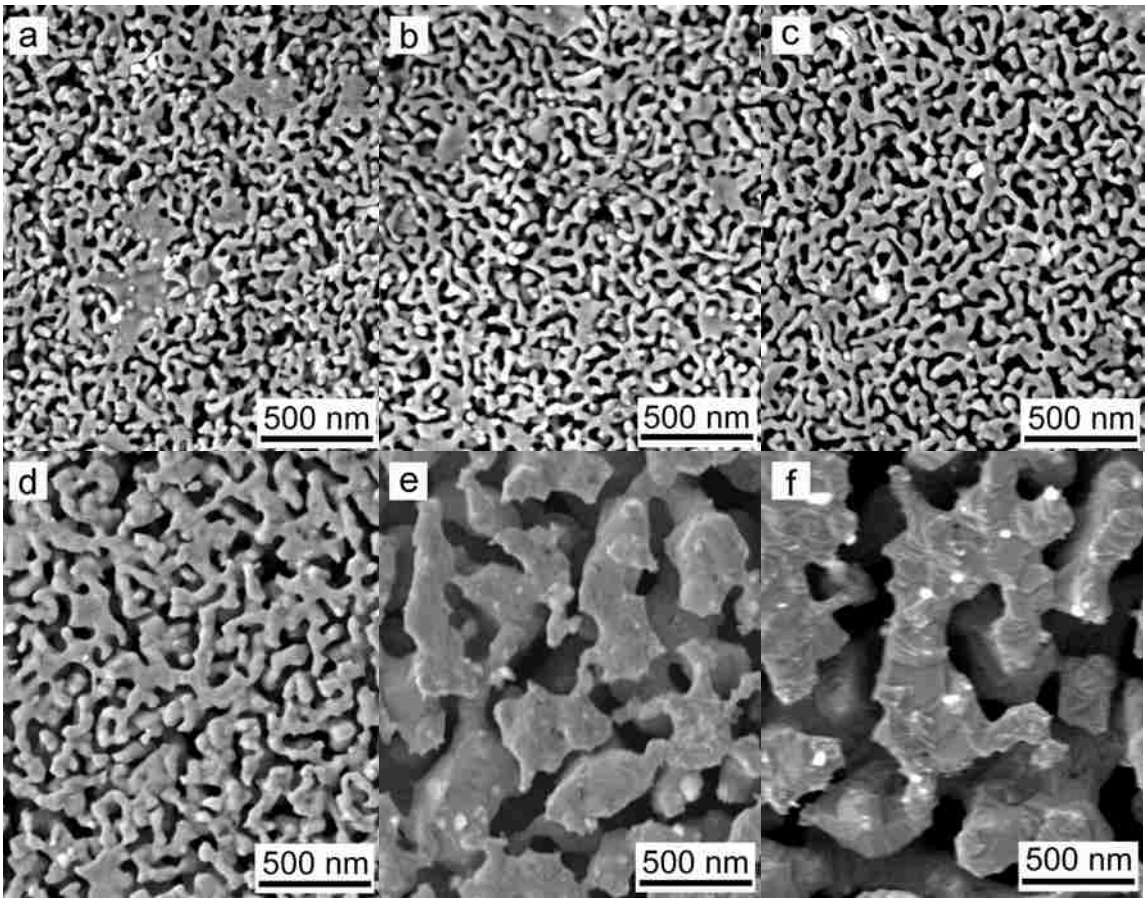

Figure 4.2 SEM micrographs of sample set A annealed in flowing N_2/air at 5 CFH at different temperatures: (a) As-dealloyed, (b) 100°C, (c) 200°C, (d) 300°C, (e) 400°C, (f) 500°C. Ligament coarsening becomes apparent at 300°C and increased significantly at/above 400°C.

Figure 4.3 shows SEM micrographs of sample set C that was annealed in vacuum at various temperatures. Figure 4.3a shows the characterstic sponge-like structure of as-dealloyed np-Au. Ligament size of bulk np-Au increased significantly during 300°C annealing in a vacuum environment. However, unlike the sample annealed in air, shown in Figure 4.2, and unlike former reports [60, 63], further ligament growth of np-Au annealed in vacuum seemed to be hindered during annealing at 300°C or above, i.e. average size of ligaments remained at roughly the same level. Ligament coarsening was accompanied by ligament agglomeration, where ligaments merged together, making some areas solid with little or no porosity. However, these merged areas did not form

bigger or wider ligaments. Considering the pores, total void or pore area remained roughly constant during 300 - 600°C heat treatments. The ligaments remained smooth, and no irregular shapes were observed (note that the agglomerated ligaments are not incorporated in the width measurements). The fusion or merging of individual np-Au ligaments here is perhaps due to a sintering process.

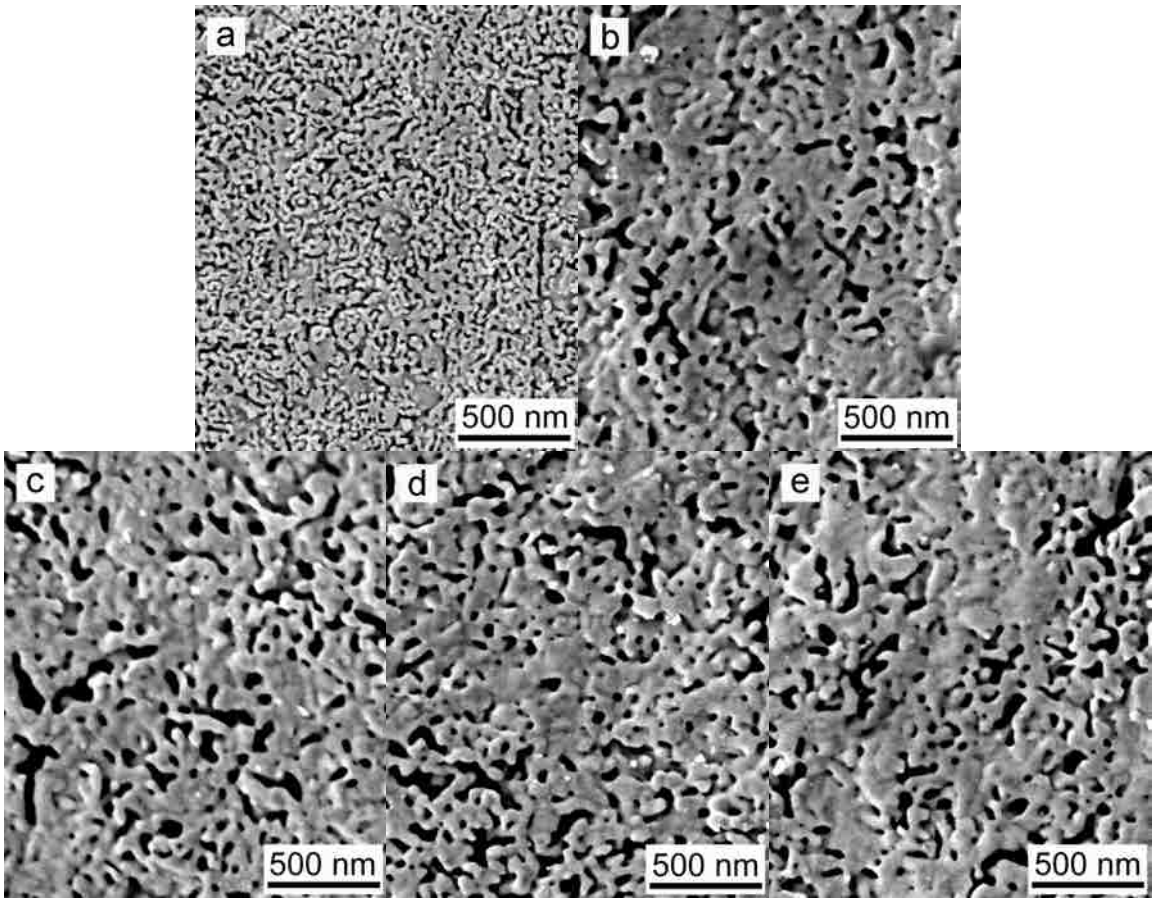

Figure 4.3 SEM micrographs of np-Au samples (set C) showing ligament change after annealing in vacuum. The sample was annealed in vacuum at different temperatures for 10 minutes. (a) as-dealloyed, (b) 300°C, (c) 400°C, (d) 500°C and (e) 600°C. Ligament agglomeration occurred during 300°C annealing, but ligament width in the non-agglomerated area did not change significantly.

Ostwald ripening and sintering are two possible mechanisms for the reduction of overall surface energy. Both involve combining individual nanostructures together to

form larger structures. In Ostwald ripening, a large structure grows at the expense of the smaller one until the latter disappears. However, in sintering, individual structures are packed such that there is no gap among solid nanostructures. Figure 4.2 suggests that the underlying ligament coarsening mechanism of np-Au annealed in air similar to Ostwald ripening [60], in the sense that large ligaments seem to grow at the expense of smaller ligaments. The fusion or coalescence of individual np-Au ligament annealed in vacuum (shown in Figure 4.3) is similar to a sintering process, when considering their surface morphologies, where ligaments contact one another but there are still boundaries among them. However, even if the coarsening mechanism of np-Au annealed in high vacuum is sintering, it cannot explain why ligaments remain relatively narrow, since sintering could result in a macroscopically uniform sample.

Since the only difference between these two annealing processes is environment, the atmosphere has an effect on ligament coarsening. In fact, Sharma et al. found that annealing atmosphere is crucial to the diffusion of Au atoms [87, 88]: the diffusion rate of Au is much slower in vacuum than in nitrogen. So even though the driving forces and total interfacial energy reduction for coarsening is the same for these two mechanisms, np-Au annealed in vacuum retains a relative narrow ligament size distribution, due to the slower diffusion rate compared to samples annealed in N_2/air.

The measured ligament sizes show a unimodal distribution for samples in both the as-dealloyed and annealed states. Figure 4.4 shows the ligament size distribution of sample set A. The histograms broaden at higher annealing temperature due to an increase in ligament size.

Figure 4.5a shows the change in ligament width of np-Au as a function of annealing temperature under two specific conditions: in vacuum and in N_2/air. It is clear that np-Au coarsens differently in these different environments when annealed at 300°C or above. The initial ligament sizes of np-Au dealloyed using a potentiostat are bigger than those for np-Auprepared using a voltage supply. For np-Au annealed in vacuum (sets C and D), the average ligament width before annealing was 17 nm. The ligament size increased continuously up to 300°C, after which it reached a plateau where the ligaments did not change significantly with additional temperature increases. At 600°C, the ligament width within the surface layer was less than 50nm. For np-Au annealed in

air (sets A and B), the ligament size was stable up to 300°C. Above 300°C, the ligament size almost doubled. Thereafter, the ligament width increased with annealing temperature, from ~50 nm at 300°C to ~200 nm at 500°C.

Figure 4.5b presents the microhardness of np-Au after annealing at various temperatures. Loads between 10 to 50 mN were used for indentation experiments on the np-Au samples. Higher loads up to 100 mN resulted in indents that were too deep and large to examine their dimensions. At higher loads, cracking around and inside the indents also posed a problem for determining the correct hardness. Before testing the samples, several other possible influences on the measurements were examined. Hardness did not change whether or not a specimen was mounted on a stainless steel holder using low temperature crystal bond. To keep the samples as clean as possible, they were not mounted for testing. Also, ultrasonicating the samples (e.g. to remove carbon paint after SEM observation) did not affect the hardness if it was performed for less than 20 sec and without the samples flipping over during the process. If the latter happened, surfaces were damaged and cold worked, which resulted in extremely high hardness values.

Samples dealloyed with the voltage supply were slightly harder than those dealloyed using a potentiostat. The samples that were dealloyed by the voltage supply exhibited an average hardness (i.e. yield strength) of 33 MPa, with an average of ligament size of 18 nm, whereas samples dealloyed with the potentiostat had a hardness of 23 MPa and a ligament size of 30 nm. The hardness generally increased with increasing annealing temperature, although some abnormal increases at 400°C made this trend somewhat inconsistent. Three samples out of four show a higher hardness at 400°C in comparison to the as-dealloyed state, and an unexpected drop at 500°C was also observed. For the two HV-annealed samples (sets C and D), the hardness increased again at 600°C. The inconsistent variation of hardness of np-Au may be caused by the fact that cracking is prevalent through samples and lower hardness will be obtained if cracking occurrs by indentation or the microindenter happens to compress areas with dealloying cracks.

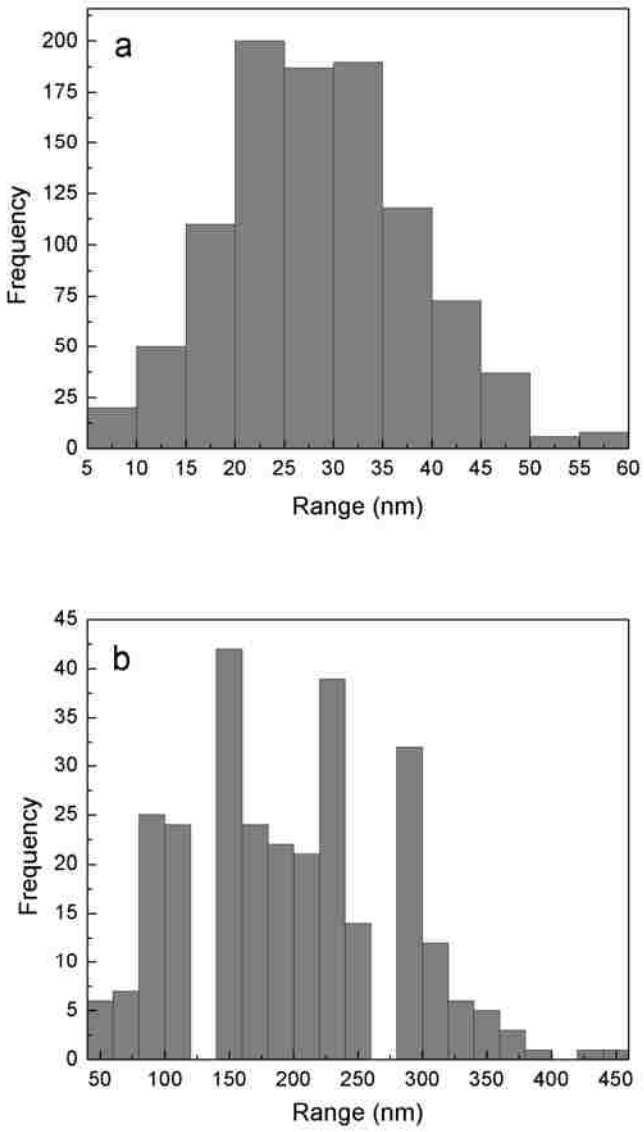

Figure 4.4 Ligament size distribution of np-Au samples (set A) in two different states: (a) as-dealloyed, (b) annealed at 500°C. Ligament sizes show unimodal distributions for both states, although size range became much broader after 500°C annealing than in the as-dealloyed condition.

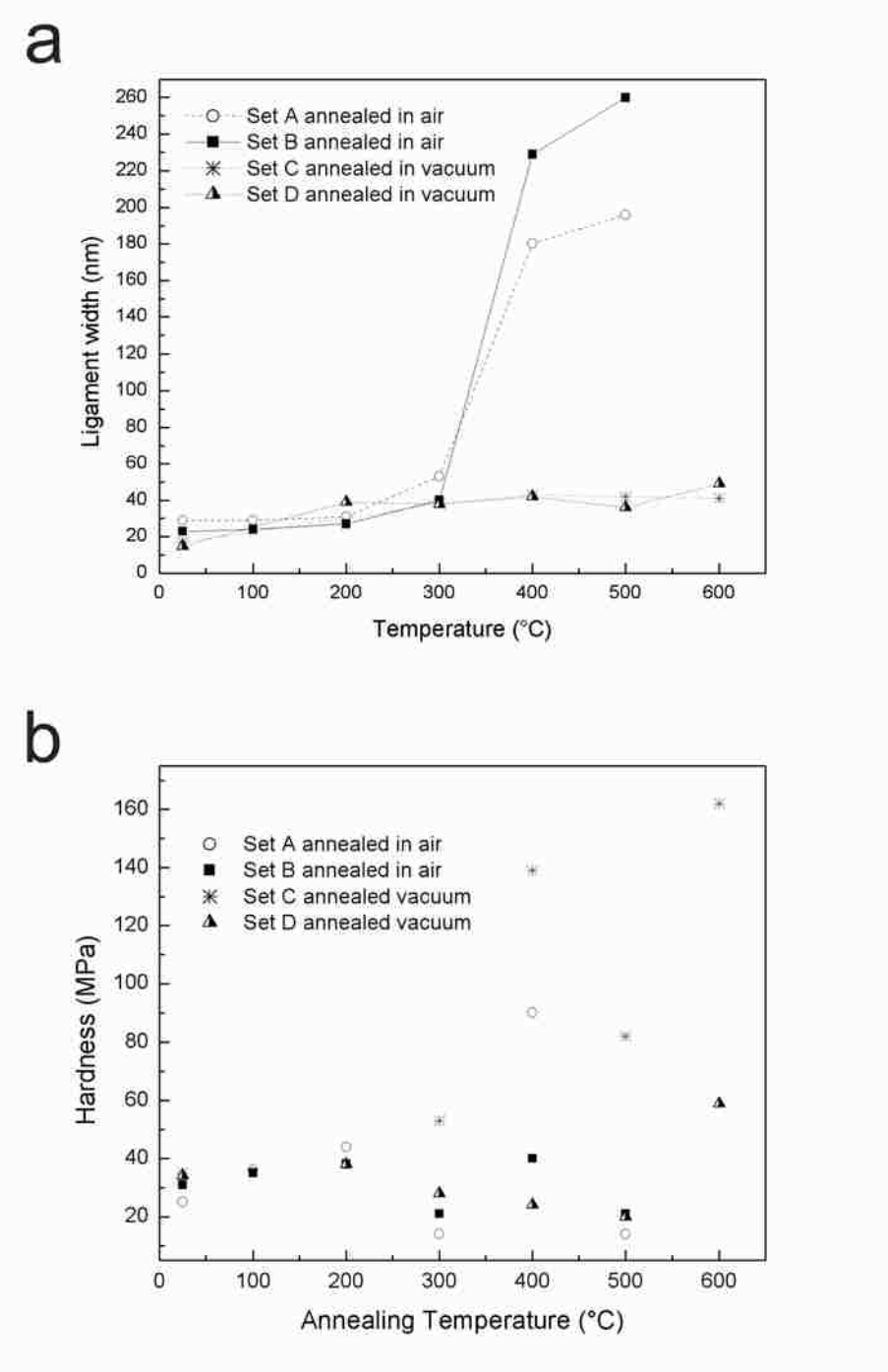

Figure 4.5 Evolution of np-Au ligament width and hardness during annealing at different temperatures. (a) Ligament width; (b) Microhardness.

Figure 4.6 shows SEM images of microindents made in an additional bulk np-Au sample before and after annealing. The sample was dealloyed using the voltage supply and was annealed in air with flowing N_2. The deformation mechanism in nanoporous Au was thought to be ductile and plastic densification [9]. However, several cracks were observed around the microindents made in the as-dealloyed np-Au (Figure 4.6a). In contrast to this, no cracks were found at the microindent edges in the air-annealed np-Au specimen (Figure 4.6b). That indicates the deformation mechanism of np-Au changed from brittle to ductile when ligament size increased in this sample. This is consistent with Sieradzki's results [63]. The more ductile behavior of the annealed sample can also be verified by more elastic recovery at the edges of the indents in Figure 4.6b. Microhardness of nanoporous Au before and after annealing was calculated from the ratio of the peak indentation load to the projected indentation area of the residual impression. After 600°C annealing, the microhardness of bulk np-Au increased to ~2.5 times higher than before annealing, from 29 MPa to 73 MPa. At the same time, ligament width of np-Au increased by a factor of 10 after annealing, from 20 nm to 220 nm.

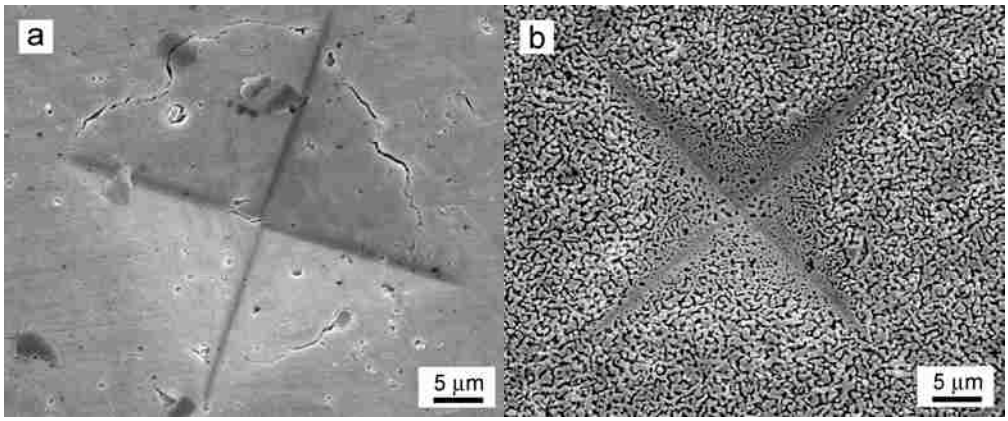

Figure 4.6 SEM micrographs of microindents in bulk np-Au indicating different deformation behavior for various ligament sizes. (a) as-dealloyed; (b) indentation after annealing at 600°C in air for 10 min after dealloying. Deformation mode changed from brittle to ductile as rographs of microindents

Fused grain boundaries in a np-Au sample after 500°C annealing in air are shown in Figure 4.7. Sintering was believed to be the underlying mechanism for fused GBs in

np-Au [58]. Similar microstructure of solid GBs was also observed in np-Au samples that were dealloyed by dilute HNO_3 (not shown here), and the relative ease for atom diffusion along GBs was thought to be the reason for the imbalance between Ag atom dissolution and Au atom diffusion [57]. Although dealloyed layers of np-Au are thought to be epitaxial with their substrates [8, 58], the grain sizes here was too small to support the hypothesis that these GBs in np-Au are inherited from the master alloys.

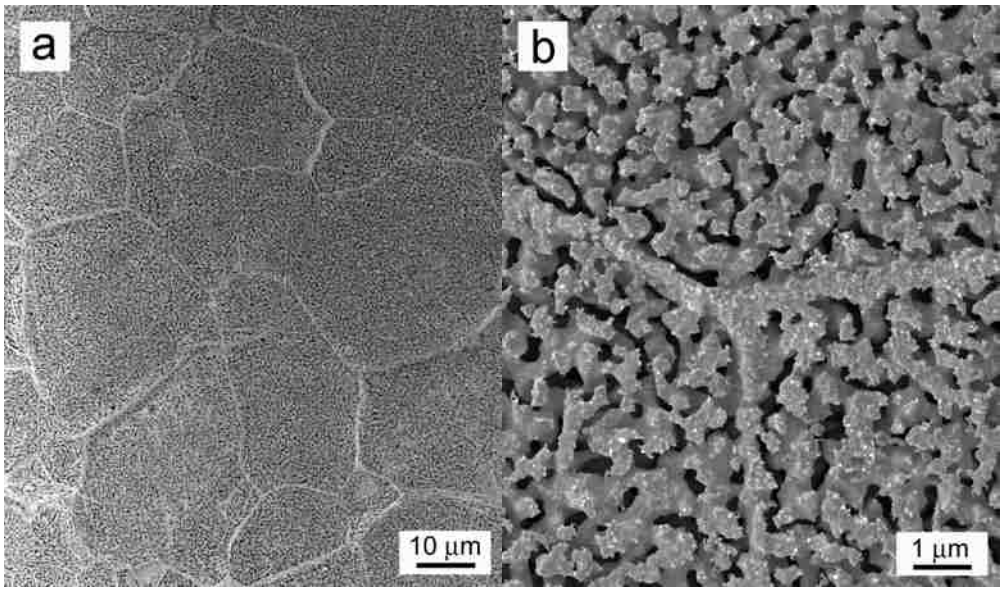

Figure 4.7 Fused grain boundaries in a np-Au sample after annealing in air at 500°C. (a) An overview of fused GBs, from which an average grain size of ~30 μm was estimated. (b) Shows a triple junction of a fused GB. Relative ease with which atoms diffuse along GBs might explain the generation of fused grain boundaries.

4.3 Summary

In summary, 25 at.% np-Au samples were fabricated by electrochemically dealloying Au-Ag alloys with a potentiostat and a basic voltage supply. Cracking occurred and was attributed to the dealloying process. Dealloyed np-Au specimens were annealed in N_2/air or in a vacuum environment. Ligament coarsening occurred in both cases at 300°C or higher, but significantly different morphologies were observed after

annealing in the various environments. This may be due to the different modes with which Au atoms diffuse in air versus vacuum. For annealing in vacuum, the underlying mechanism of coarsening is similar to sintering, whereas a mechanism similar to Ostwald ripening may control ligament growth in air. These findings suggest that nanoscale or nanostructured Au, such as np-Au, is more thermally stable in vacuum applications than in air. Ligament width showed a unimodal distribution in both the as-dealloyed and post-annealed states. Microhardness of np-Au generally increased with increasing annealing temperatures, although some inconsistencies were observed. The inconsistent trend of hardness with temperature was thought to be the result of interaction between the microindenter and cracks caused by dealloying. Deformation of np-Au changed from brittle to ductile when ligaments grew bigger. Fused grain boundaries appeared when np-Au was annealed above 400°C and is thought to result from sintering of neighboring Au atoms.

Chapter 5

A multi-step dealloying method to produce nanoporous Au with no volume change and minimal cracking

This chapter is based on the following published manuscript:
Ye Sun, T. John Balk, *A multi-step dealloying method to produce nanoporous gold with no volume change and minimal cracking*, Scripta Materialia **58** 727-730 (2008),

5.1 Introduction

Nanoporous Au (np-Au) has become an increasingly popular research material, although the focus of studies has changed over the past 20 years. In the early 1990's, np-Au was studied in terms of metallic corrosion [43-46]; starting approximately 10 years ago, research on np-Au shifted toward mechanisms of dealloying and the evolution of dealloying microstructure [8, 16, 48, 49]; more recently, the mechanical properties of np-Au have drawn an increasing amount of attention [60-62, 64, 67, 75]. A newer area of investigation involves the dimensional changes of np-Au samples caused by the dealloying process [53, 54], since these changes affect the actual relative density, which is one of the most important parameters determining the mechanical properties of porous materials [52]. For nanoporous metals obtained by dealloying, any changes in the physical dimensions of a sample due to dealloying will affect the relative density. It is thus paramount to characterize and, if possible, control the volume change caused by the dealloying process.

Recently, Parida et al. reported volume reduction up to 30% during electrochemical dealloying of free-standing leaf and bulk Au-Ag alloy (25 at.% Au) [53] and attributed this to plastic deformation in the form of "homogeneous slip in small ligaments" or "climb of lattice dislocations". In contrast, simulations from Crowson et al. indicated that surface relaxation is the main cause of the geometric contraction of np-Au samples [54].

The mechanical integrity or robustness of nanoporous metals is vital for their application in devices such as sensors, fuel cells and actuators. Due to the volume contraction that typically accompanies dealloying, and due to the macroscopically brittle nature of nanoporous metals, crack formation seemed inevitable during processing and service [11, 55, 56]. However, crack-free thin film np-Au [72] and relatively thin (100 μm) bulk np-Au foil [58] have been successfully fabricated by optimizing the Au-Ag precursor alloy composition, controlling the applied potential and/or increasing the electrolyte temperature. It should be noted that the crack-free 100 μm thick np-Au was not completely dealloyed through the thickness; only a thin surface layer, several microns thick, was dealloyed [58]. However, producing thicker (e.g. 500 μm) bulk np-Au that was completely dealloyed and crack-free remained elusive.

In this chapter we present a facile two-step electrochemical dealloying method to produce np-Au with no volume change. HNO_3 was the electrolyte, but no electrolyte heating was needed, in contrast to other studies [58]. We report for the first time that the resulting bulk np-Au exhibited no volume change whatsoever, but still evolved a normal bicontinuous porous structure with a ligament width of 14 nm. Only a few narrow intergranular cracks were observed at isolated locations on the sample surface, while the vast majority of the sample surface was crack-free, and thus the cracks do not provide a continuous path for failure. This approach has also been used to fabricate millimeter-scale specimens (2.2 mm × 2.4 mm × 2.8 mm). Furthermore, surface defects on the sample remained exactly the same as before dealloying, which can be explained by existing models [8, 48].

Bulk Au-Ag alloy pellets (30 at.% Au), purchased from the Kurt J. Lesker Company, were cut into ~4 mm × 4 mm plates with ~0.45 mm thickness. These specimens were annealed at 850˚C for 100 hours to relieve residual stresses from cutting and ensure a consistent grain size. In order to make the nanoporous samples, an external potential of 1.0 V was applied to the annealed Au-Ag alloy, using a platinum wire as a counter electrode. A simple galvanostatic electrochemical cell was used, similar to that of Rösler et al. [78], where potential was applied with a voltage supply instead of a potentiostat. Dealloying was performed in multiple stages and with varying etchant concentration. For the first stage, a 1:2 diluted acid solution [30 ml HNO_3 (70% stock

solution) mixed with 60 ml distilled H_2O] was used as the electrolyte. After dealloying with the 1:2 acid solution for up to 70 hours, the electrolyte was changed to stock (70%) HNO_3 and dealloying continued for 10 more hours. Morphology of the sample surface before and after dealloying was observed with an optical microscope (Olympus BX41) and scanning electron microscopes (Hitachi S900 and S3200 SEMs). A focused ion beam workstation (FEI Strata 235 Dual Beam FIB) at the National Center for Electron Microscopy in Berkeley, CA was also used for imaging np-Au.

5.2 Results and discussion

This two-step dealloying method has proven very successful for fabricating bulk np-Au. According to the measured mass loss from the sample, and assuming all mass loss was Ag, the Ag in the samples was completely removed. This was verified by energy-dispersive x-ray spectroscopy, which revealed a residual Ag content less than 2 at.%. After the first dealloying step (70 hours with dilute HNO_3), ~75 wt.% of the total Ag in the sample was removed. Thus, the starting composition of the Au-Ag alloy for the second dealloying step (with stock 70% HNO_3) was ~64 at.% Au.

Table 5.1 shows voltage and current readings taken during the first dealloying step. After the first half hour, the current and voltage were consistent during the entire dealloying process. At the beginning of the second dealloying step, voltage and current were the same as in the first step, i.e. ~500 mV and ≥200 μA. At the end of the second dealloying step, no current flow was measured.

Table 5.1 Voltage and current measured during the first step of the dealloying process.

Dealloying time (h)	Voltage (mV)	Current (μA)
0	876	50
0.5	500	200
12	486	220
13	487	220
14.5	502	203
70	557	192

Figure 5.1 shows a comparison of sample dimensions before and after dealloying. It is seen that, compared with the master alloy, no shrinkage of np-Au in either the lateral dimensions or the thickness occurred during dealloying. This observation of no volume change is in stark contrast to the 20-30% volume contraction observed by Parida et al. [53], but is compatible with the rigid lattice concept mentioned in their paper, whereby lattice structure should not change due to Ag leaching. It also agrees with the observation by Rösler et al. [78] that galvanostatic dealloying produces no noticeable volume contraction during etching of two-phase Ni-base superalloys, and is consistent with the observation of no shrinkage in np-Au leaf during electroless etching [89]. As suggested by Rösler, the reasons why the method used in the present study can completely dealloy millimeter-scale samples are (1) galvanostatic etching can provide a constant current density and impose a constant Ag dissolution rate [78], and (2) Au does not oxidize, at least not under the potential applied here, and therefore does not hinder etching at longer times [58, 78]. Furthermore, if no oxidation occurs during dealloying, surface diffusion may relax the tensile stresses that would otherwise evolve, thereby lowering the tendency for np-Au to crack.

Figure 5.2 presents optical micrographs of the sample surface, with Figure 5.2a showing the precursor Au-Ag alloy surface and Figure 5.2b showing dealloyed np-Au. Figure 5.2c is a Nomarski differential interference contrast (DIC) optical image of the Au-Ag alloy surface. Throughout the dealloying process, all observed defects on the sample surface such as grain boundaries and twins retained the same macroscopic appearance (compare Figures 5.2a-b), although microscopically the structure became nanoporous. This observation indicates that dealloyed np-Au retains an epitaxial relationship with the master alloy substrate throughout the dealloying process. This may be explained by models of dealloying, during which the lattice structure is retained even though some lattice sites are vacant due to dissolution of Ag atoms and subsequent diffusion of Au atoms [48, 49].

Figure 5.3 presents SEM images showing an isolated crack and other surface features in the dealloyed sample. After dealloying, the sample is crack-free in most areas, except for a few isolated, narrow intergranular cracks such as shown in Figure 5.3a. The fact that the two-step dealloying method yields almost crack-free and completely

dealloyed bulk np-Au suggests that crack formation is most sensitive to dealloying rate and/or electrolyte concentration during the initial stage of dealloying, since concentrated

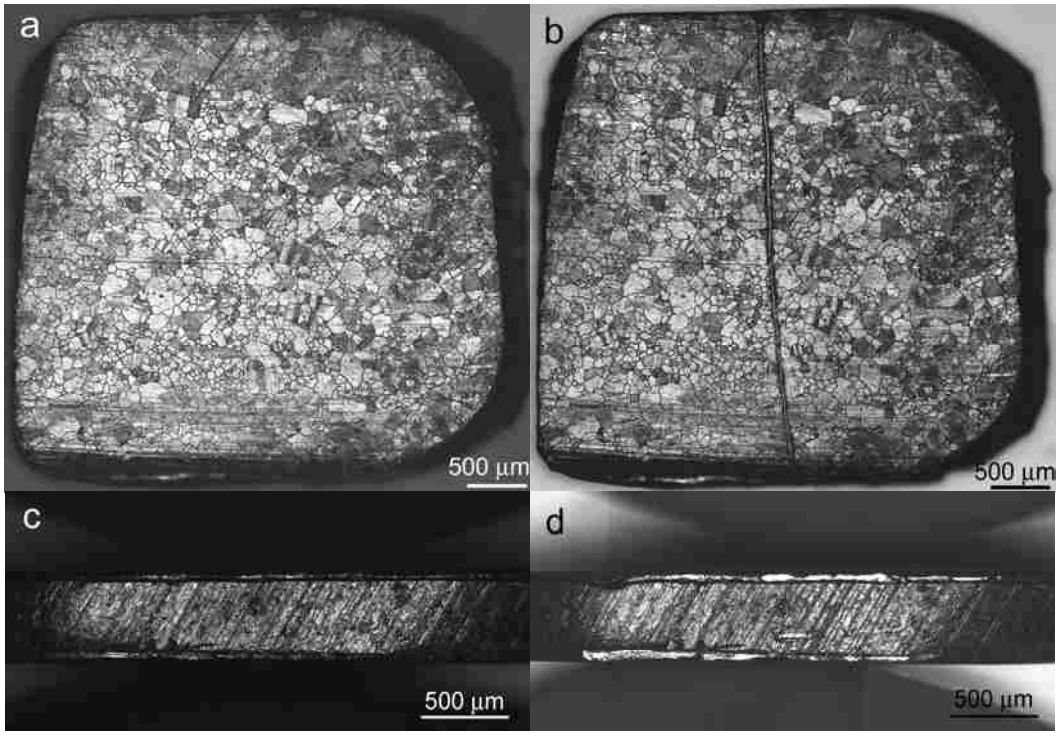

Figure 5.1 Comparison of sample dimensions of the master alloy versus np-Au after dealloying. (a) Lateral dimensions and (c) thickness of the sample before dealloying; (b) and (d) after dealloying. Neither lateral dimensions nor thickness of the sample change during two-step dealloying. The scratch in the middle of (b) occurred specimen handling. The outer layers seen in the thickness images are from the initial cutting process.

70% HNO_3 was used during the second stage but did not cause cracking (in contrast to one-step dealloying with concentrated HNO_3, which always resulted in extensive grain boundary cracking). The dilute electrolyte used in the first stage likely causes a lower initial etch rate and mitigates the tensile stress that generally causes cracking during dealloying [66], since it should lower the dealloying rate by slowing dissolution of Ag atoms and allowing more time for diffusion of Au atoms. At higher magnifications in the SEM, as shown in Figures 5.3b-c, twins and wavy lines (similar to forging flow lines that accompany mechanical fibering) are seen in the nanoporous

structure, and are the same as those in the Au-Ag alloy (see Figures 5.2a-c). These nanoporous areas are continuous with neighboring regions in the same grain, except the contrast varies across the edges of these features.

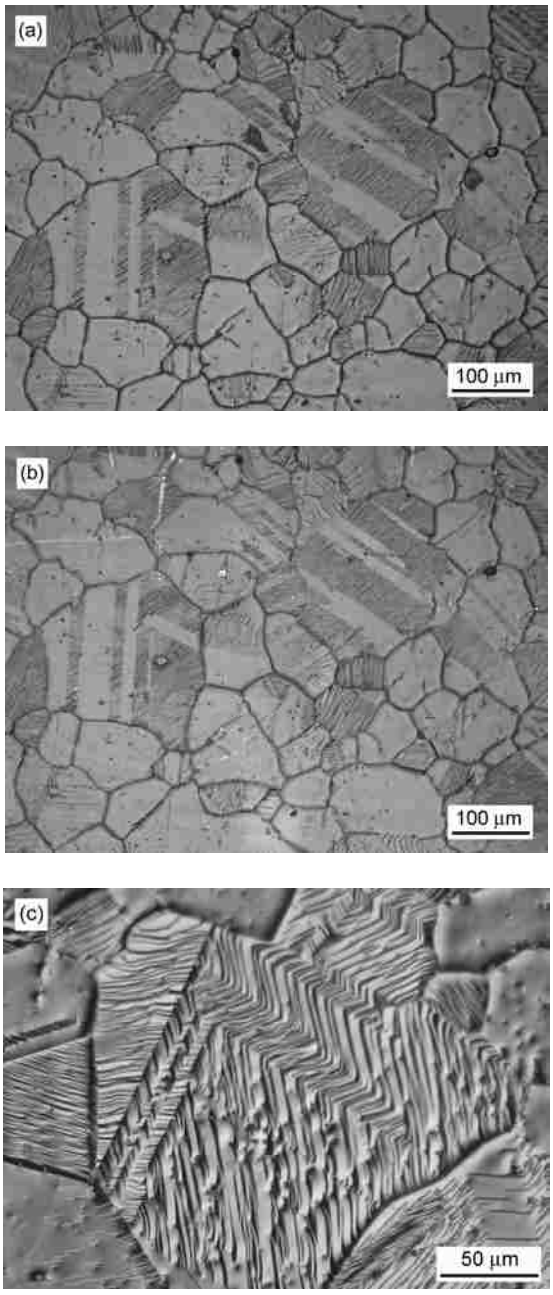

Figure 5.2 Optical micrographs showing defects on the surface of Au-Ag sample (a) before dealloying and (b) after dealloying. (c) DIC optical micrograph before dealloying reveals sample features that were retained on the np-Au surface.

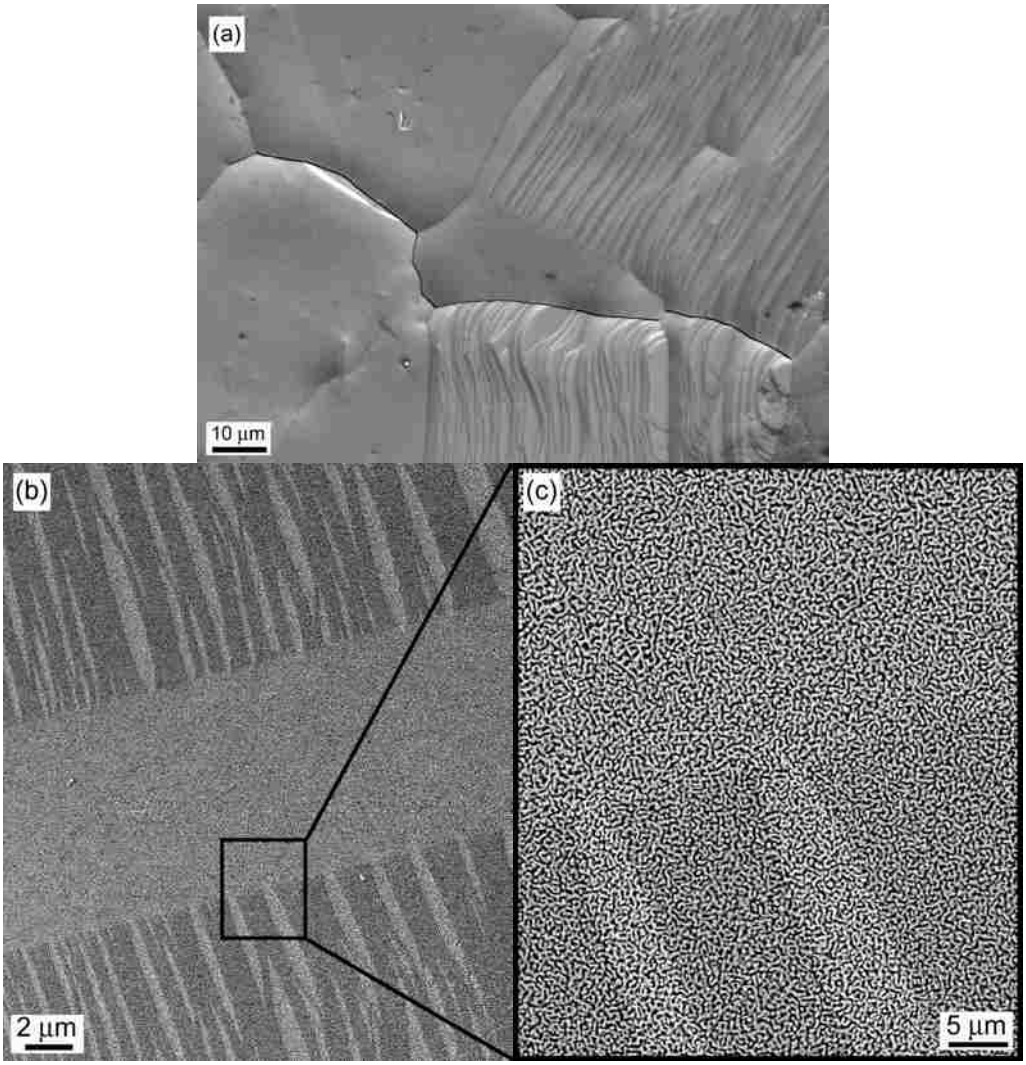

Figure 5.3 SEM images showing an isolated crack and wavy lines on the dealloyed sample surface. (a) After dealloying, bulk np-Au was nearly crack-free, although isolated intergranular cracks were found at a small number of grain boundaries. (b) Dealloyed np-Au exhibiting twins and wavy lines on the sample surface. (c) Close-up of the area outlined in (b), illustrating the continuity of the nanoporous structure across features.

Figure 5.4 shows different morphologies of grain boundaries observed in two-step dealloyed samples. In Figure 5.4a, a grain boundary (GB) triple-junction is seen on the

sample. Surfaces separated by GBs in different grains were not always at the exact same level. Figure 5.4a shows an open GB (at the bottom) bridged by ligaments. Presumably, bridging ligaments below the surface also span this dealloyed GB, since it has not opened into a crack, even though the GB appears to have dissolved. The width of the GB is approximately equal to the pore size or ligament spacing. This "open" GB is not a crack, but may provide a continuous path for sliding or other strain accommodation. Figure 5.4b shows a crack-free GB where ligaments are interconnected along the entire boundary line. Figure 5.4c shows a fused grain boundary, another type of dealloyed GB sometimes observed here.

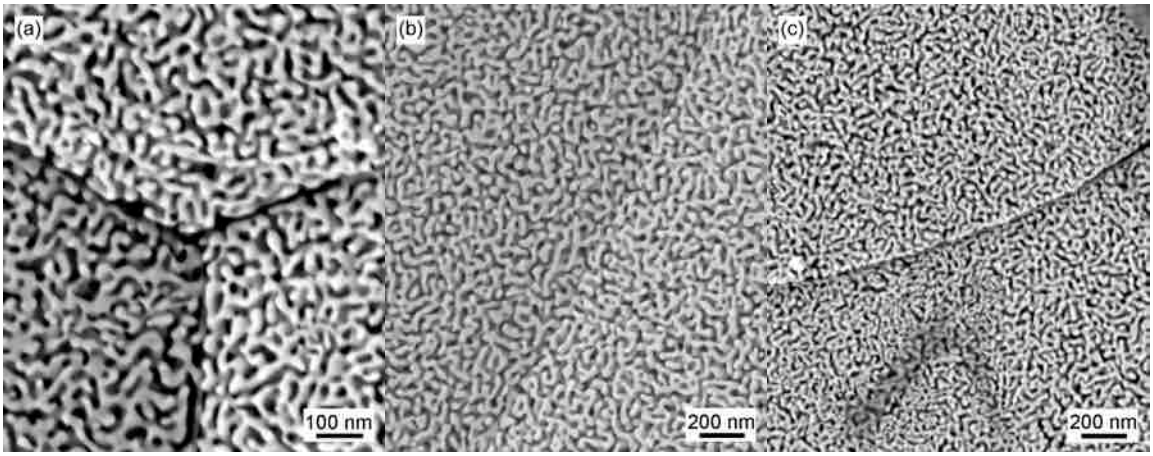

Figure 5.4 Different morphologies observed at grain boundaries in two-step dealloyed samples. (a) Grain boundary (GB) triple-junction, where GBs appear to have completely dissolved, although ligaments still span the GB. The width of the "open" GB roughly equals the pore size. (b) Continuous ligament structure along entire GB, from lower left to upper right of this image. (c) Fused GB, where a continuous line/sheet lies between the grains. Average ligament size of np-Au after two-step dealloying was 14 nm.

According to proposed mechanisms of dealloying, the formation of stable interconnected ligaments in np-Au is achieved by a balance between the rate of Ag dissolution and that of Au surface diffusion [8, 16, 48, 49]. Observation of different morphologies at individual grain boundaries suggests that the rate of dissolution of Ag atoms may be faster or slower than that of surface diffusion of Au atoms, resulting in

either voids (Figure 5.4a) or fused grain boundaries (Figure 5.4c). This imbalance in Ag dissolution rate and Au surface diffusion rate may be due to Ag enrichment at certain GBs, but it may also be due to GB character and the relative ease/difficulty with which atoms diffuse along the GB, a topic that warrants further investigation.

Figure 5.5 shows the effect of focused ion beam (FIB) imaging on the np-Au microstructure. Originally, FIB work in this study was intended to cut cross-sections for observing internal defects in two-step dealloyed samples. Instead, it was the FIB that created defects, causing rapid and significant damage to the sample surface. Figures 5.5a-b show SEM images of the same location on the bulk np-Au surface before and after brief exposure to the ion beam. It is readily apparent that the ion beam causes grain boundary cracking (indicated by white arrows in Figure 5.5b) on the np-Au surface, as well as spallation along polishing lines across grain interiors (Figure 5.5b). Black arrows along the bottom of Figure 5.5b indicate the edge of the area scanned by the ion beam. Figure 5.5c shows three neighboring areas that were exposed to varying ion beam exposure: unexposed np-Au to the left of the white arrow; between the white and black arrows, the material was exposed to one imaging pass of the ion beam; to the right of the black arrow, the material was exposed to two imaging passes. Note that the maximum exposure was extremely brief, only enough to acquire two single-scan FIB images (focusing in FIB mode was performed at an adjacent location, different from that in Figures 5.5b-d). From Figure 5.5c, the effect of the FIB on the np-Au surface is readily seen: cracks became wider with increasing exposure from left to right. The FIB also caused ligament coarsening, which can be seen in Figures 5.5c-d. Figure 5.5d shows a crack tip caused by FIB exposure, where highly strained ligaments bridge the crack.

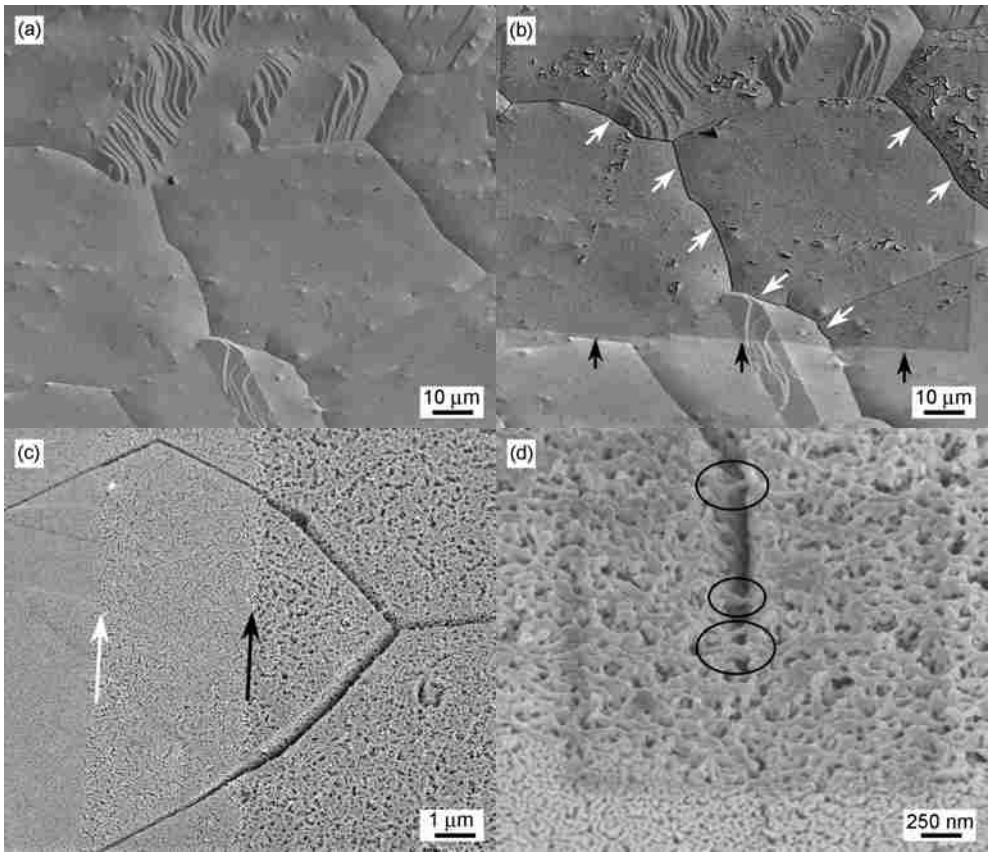

Figure 5.5 SEM micrographs showing the effect of FIB imaging on dealloyed np-Au. (a)-(b) show the same location before and after brief FIB exposure. Cracks along GBs due to FIB exposure are marked by white arrows in (b). Black arrows indicate the lower edge of ion beam exposure. (c) Three distinct regions, corresponding to varying ion beam exposure (increasing exposure from left to right). (d) Bridging ligaments across a crack face (marked by ellipses) created during FIB imaging.

5.3 Summary

In summary, a two-step dealloying method was used to produce crack-free bulk np-Au with millimeter dimensions and exhibiting no volume change. Surface features and defects were retained during dealloying, even though nearly all Ag was removed from the precursor alloy. Isolated cracks were observed in dealloyed np-Au, but these were few in number and did not cause the specimen to break during handling or otherwise compromise mechanical integrity. Various types of dealloyed grain boundaries were observed in fully dealloyed samples (open, closed, or continuous/fused GBs). It is postulated that this variety in GB morphology is due to the character of the original GB,

which should affect diffusion and dissolution rates. In contrast to the potentiostatic dealloying method used by many researchers, the galvanostatic approach used here is well suited to the fabrication of millimeter-scale bulk np-Au with no cracking or volume contraction. It appears that the most important aspect of the two-step dealloying method is initial use of 1:2 diluted HNO_3 as the etchant, since that slows the initial etch rate. However, use of the two-step method described here allows complete dealloying to be achieved more quickly than with dilute acid alone. Finally, FIB exposure caused rapid and severe cracking and coarsening of the np-Au structure. Therefore, care must be taken when using ion beam milling to prepare samples from this fragile material.

Chapter 6

Evolution of Structure, Composition and Stress in Nanoporous Au Thin Films with Grain Boundary Cracks

This chapter is based on the following published manuscript:
Ye Sun and T. John Balk, *Evolution of Structure, Composition and Stress in Nanoporous gold Thin Films with Grain Boundary Cracks*, Metallurgical and Materials Transactions A, **39A** 2656-2665 (2008), copyright of 2008 by Springer Science and Business Media.

6.1 Introduction

Nanoporous Au (np-Au) has received a growing amount of attention recently, due to its potential applications in areas such as sensing, actuation, catalysis and super-capacitance [27, 28, 31, 37], which would benefit from the high surface-to-volume ratio and noble metal chemistry of np-Au. Nanoporous noble metals are formed by a selective dissolution process called dealloying, during which the less noble atoms (e.g. Ag) are dissolved from a precursor alloy (e.g. Au-Ag), leaving behind a nanoscale, interconnected network of Au ligaments and open pores [8, 48, 49]. Although one study of the mechanical properties of np-Au was first published 16 years ago [63], most research on this material has focused on its synthesis, structure, and mechanism of formation. Several studies have concentrated on the deformation mechanisms and ligament strength of np-Au [55, 60, 61, 66, 68, 70, 71], and this area appears to be gaining research attention. Li et al. [63] analyzed the failure behavior of nanoporous Au beams with various ligament sizes using a three-point bending method, and reported a sample-size-driven ductile-brittle transition in np-Au. Biener et al. [61] calculated the hardness and yield strength of np-Au based on nanoindentation measurements and found that the yield strength of np-Au was ~10 times larger than predicted by Gibson-Ashby scaling laws [52]. Volkert et al. [55] reported a high yield strength of 1.5 GPa for 15 nm diameter np-Au ligaments by uniaxial compression, which approaches the theoretical

strength of Au. However, our preliminary work conducted in conjunction with the current study (described in this paper) suggests that the strength of bulk np-Au measured by microindentation may be significantly lower than the values reported by Biener et al. [61] and Volkert et al. [55], depending on the initial alloy composition and final microstructure after dealloying. The mechanical behavior of np-Au is not completely understood and requires further investigation.

Thin films of np-Au can be readily produced, with the advantage that the dealloyed structure is uniform through the thickness. Most studies of np-Au thin films [53, 65, 89] have utilized broad, free-standing films. However, these are difficult to handle and fabricate into structures. Producing np-Au thin films supported by a substrate, which is the aim of the current study, may help to solve problems associated with the instability of free-standing np-Au films. Such an approach also lends itself to wafer curvature measurements of np-Au film stress at various processing intervals, as well as evaluation of its mechanical behavior as a function of temperature [79].

This chapter discusses the structure, composition and mechanical behavior of np-Au thin films during dealloying and thermal cycling. The 25 at.% Au precursor alloy yields stress-free but extensively cracked films, which nonetheless exhibit excellent adhesion to the substrate. This system offers an opportunity to systematically study np-Au thin films supported by substrates.

6.2 Experimental

25 at.% Au-75 at.% Ag alloy films of various thickness were sputtered onto different substrates at room temperature in a high vacuum chamber (ORION system, AJA International, base pressure ~10^{-6} Pa). Substrates included glass slides and 180 μm thick (100)-oriented silicon wafers (CrysTec GmbH, Germany) that had been coated with 10 nm of amorphous silicon oxide and 50 nm of amorphous silicon nitride. To improve adhesion of the alloy film to the glass substrates, a 10 nm Au interlayer was deposited before the Au-Ag films were sputtered, which reduced the tendency of the films to flake off the substrates during dealloying. Additionally, for the films on Si substrates, a 10 nm Ta interlayer was sputtered before the pure Au interlayer, to further improve the adhesion of the dealloyed np-Au films to their substrates.

Dealloying of Au-Ag precursor films was achieved by immersing the samples in concentrated HNO_3 (70% stock concentration), for times ranging from 10 s to 100 min. In order to determine the evolution of composition and surface morphology of np-Au specimens, additional Au-Ag films were cut into small pieces (~5 mm × 5 mm) and dealloyed for 10 s, 20 s, 30 s and 1, 3, 5, 10, 30, 60 and 100 min. Morphology of the film surface at various dealloying times was observed with a scanning electron microscope (Hitachi S900 SEM). Energy dispersive X-ray spectroscopy (EDS, Hitachi S3200 SEM) was used to determine the film composition at each dealloying stage.

Stress in the np-Au films was measured using a wafer curvature apparatus (FLX-2320-S, Toho Technology Corporation). The stress evolution of a single sample during dealloying was tracked by measuring the curvature of the film/substrate following each dealloying time interval. A three-dimensional map of film stress was generated from diametric scans performed in rotational increments of 15°, allowing calculation of an average stress that is representative of the entire wafer surface [84]. Thermal cycles were monitored with the same wafer curvature system, at a heating and cooling rate of 5 °C/min, while periodically measuring the film stress. The stress-temperature behavior of the Ta/Au interlayer was measured separately, with a different sample, and was subtracted from the overall behavior of the composite film stack (Ta/Au/np-Au) in order to obtain the thermal cycling behavior of the np-Au layer only. Note that all film stresses were calculated using the initial alloy thickness, since film thickness was not measured at all stages of dealloying. Given that the film becomes 13% thinner during dealloying (as reported below), the actual stress of nanoporous films should be slightly (up to 15%) higher than the values reported here.

6.3 Results and observation

The microstructure and corresponding mechanical properties of nanoporous metals depend on several factors during dealloying, including the composition of the precursor alloy, dealloying potential, electrolyte composition and temperature [49]. This chapter discusses np-Au made from alloy films by free corrosion, i.e. no electrical potential was applied during dealloying. The actual starting alloy composition measured by EDS was 24.3 at.% Au. The film designations and compositions are shown in Table

6.1, where film thicknesses have been calculated from sputtering times and measured deposition rates. Note that, as discussed below, the overall thickness of np-Au (ligaments and pores) after dealloying is less than the thickness of the initial alloy film, due to volume contraction.

Table 6.1 Summary of film designation and composition of the samples in this study. The total thickness of Au ligaments in the film, calculated from alloy thickness and Au content, is listed in the final column. Np-Au films were designated by the thickness of the initial alloy film.

Designation	Substrate	Film layer sequence	Net Au thickness in np-Au layer (nm)
G1	Glass	10 nm Au + 130 nm Au-Ag	32
S8	Si	10 nm Ta + 10 nm Au + 387 nm Au-Ag	94
S9	Si	10 nm Ta + 10 nm Au + 387 nm Au-Ag	94
S11	Si	10 nm Ta + 10 nm Au + 387 nm Au-Ag	94
S12	Si	10 nm Ta + 10 nm Au + 112 nm Au-Ag	27

6.3.1 Morphology and composition

The SEM micrographs in Figure 6.1 show a comparison of the surface morphology of np-Au films on glass (with Au interlayer only) and on Si substrates (with Ta and Au interlayers). A large number of cracks were observed in both samples, even after 1 min of dealloying. Cracking commonly occurs in np-Au [55, 58], presumably due to volume shrinkage during dealloying [53]. Although cracking in the sample with both Ta and Au interlayers was still extensive (Figure 6.1b), only the films on glass (with Au interlayer only) were observed to delaminate from the substrate (Figure 6.1a). The primary difference between these two samples is the presence of a Ta interlayer. The Au/np-Au interface should be the same in both samples, implying that the interface between the Au interlayer and the underlying material strongly influences film adhesion and delamination. It is thus inferred that the Ta interlayer enhanced the adhesion of the Au interlayer to the Si substrate and was therefore critical to the stability of these np-Au films.

However, the Au interlayer between Ta and Au-Ag was also vital to the integrity of dealloyed films: as-sputtered composite film stacks (identical to samples S9 and S11)

were annealed at 450 °C for 20 min and then dealloyed, but the resulting np-Au film flaked off the Ta-coated Si substrate. This is most likely due to diffusion of Au atoms from the interlayer into the Au-Ag alloy layer, which effectively removed the Au interlayer. The presence of a continuous Au interlayer provides a better anchor for the np-Au ligaments than does the Ta interlayer alone. Similar work using Cr and Au interlayers to improve adhesion of np-Au films to Si substrates has also been reported by other researchers [76]. In this study, Ta was chosen as the first interlayer material because its lack of a ductile-to-brittle transition makes it more suitable for low-temperature thermal cycling experiments.

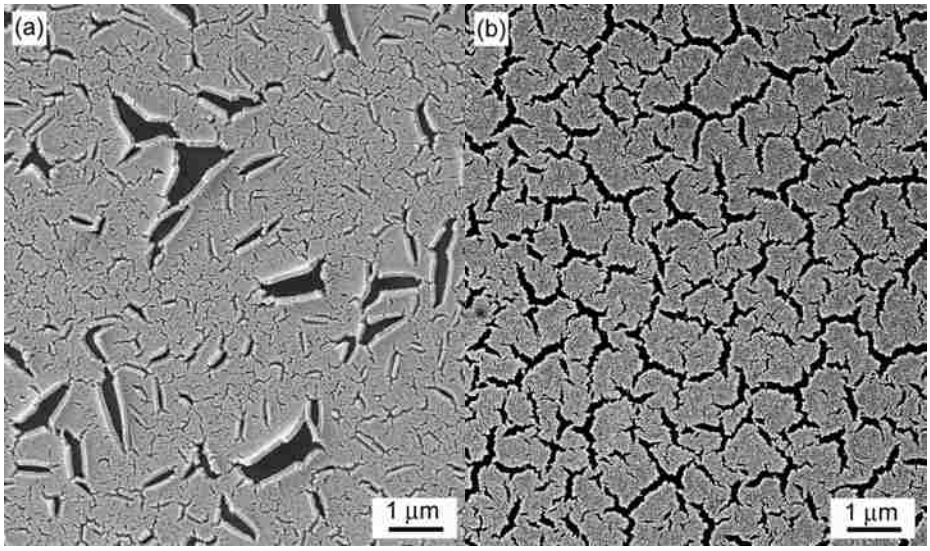

Figure 6.1 SEM micrographs showing surface morphology of np-Au films dealloyed for 1 min. (a) 130 nm np-Au on glass with Au interlayer (sample G1), where delamination has occurred near film cracks. (b) 387 nm np-Au on Si with Ta and Au interlayers (sample S9), where the Ta interlayer has prevented delamination of np-Au.

Higher magnification SEM images of the 130 nm np-Au film on glass (with a 10 nm Au interlayer) are shown in Figure 6.2. These images reveal several features of the morphology of this np-Au film, which are also observed in the np-Au films on Si: (i) Significant "cracking" occurred and was observed at the earliest stages of dealloying, even after 1 min. (ii) The cracks appeared to extend all the way down to the substrate. (iii) The average spacing of large cracks was ~300 nm. (iv) Pore and ligament size

increased with prolonged dealloying time. (v) Cracks in the film became less prominent at longer dealloying times, as the ligaments coarsened and the porous structure became more uniform in appearance. Note that the cracks did not shrink or disappear, but they did not grow, either. Instead, the surrounding ligaments and pores increased in size until they were nearly as large as the cracks (Figure 6.2c).

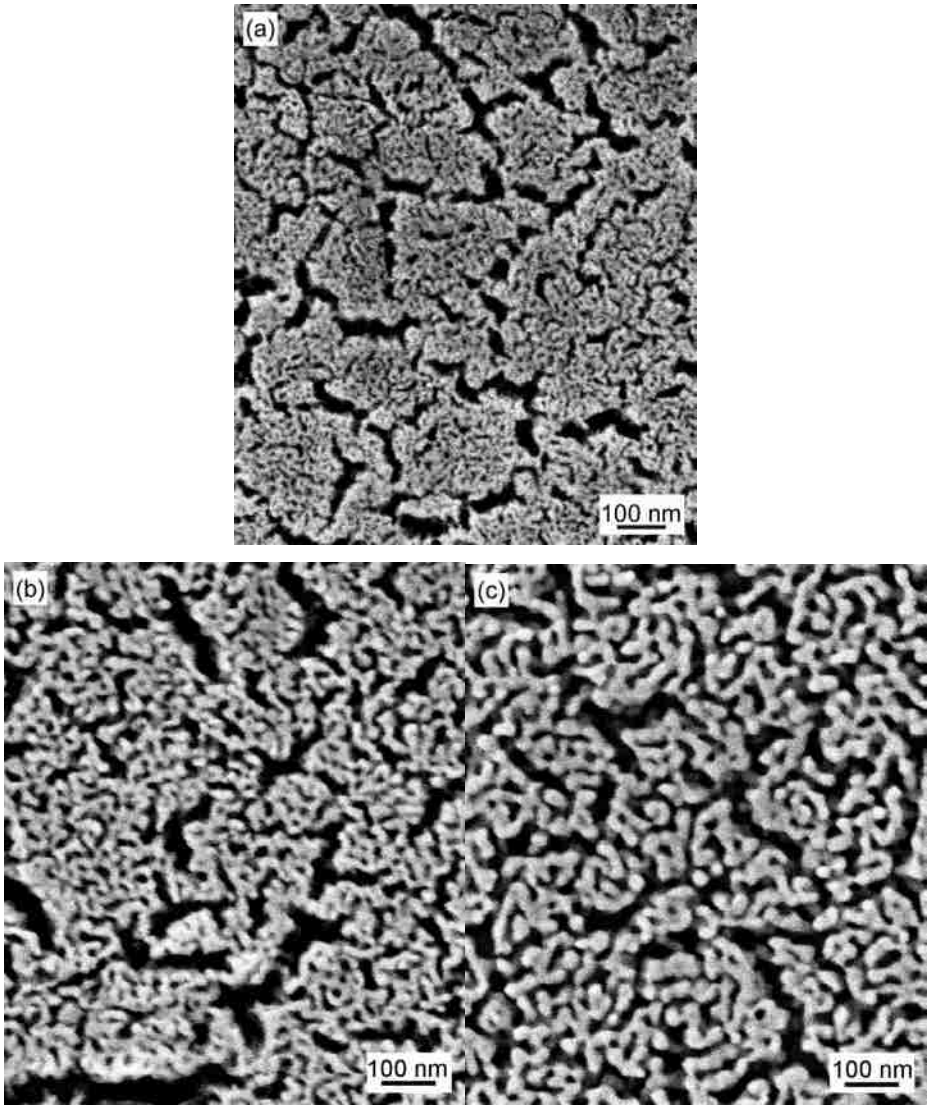

Figure 6.2 Evolution of nanoporous structure in a 130 nm np-Au film on glass substrate (G1) after dealloying times of (a) 1 min, (b) 5 min, (c) 10 min. "Cracks" appear in the film almost immediately, before pores undergo any significant growth. During dealloying, the pores and Au ligaments coarsen, but the width of large cracks remains roughly constant.

The evolution of morphology in a 387 nm np-Au film on Si substrate (with Ta and Au interlayers; sample S9) is illustrated in Figure 6.3. In contrast to sample G1, a Ta interlayer was added to sample S9 before sputtering the Au interlayer and resulted in excellent adhesion of np-Au to the substrate at all stages of dealloying. However, cracking was still prevalent throughout the film, as seen in Figures 6.3a-c and in the lower magnification image in Figure 1b. At longer dealloying times, the np-Au structure became more "open" and the porosity more interconnected. While the ligaments coarsened, the maximum crack width remained fairly constant (compare Figures 6.3a and 3c), as was also seen for np-Au films on glass (Figure 6.2).

Figure 6.4 shows cross-sectional SEM images of a 387 nm np-Au thin film (S11) on Si substrate, at various stages of dealloying. Figure 6.4a shows the initial alloy film, before any dealloying, and reveals that the film is fully dense with an average grain size ~50 nm. Figure 6.4b shows the cross section, viewed edge-on, of a sample dealloyed for 1 min, while Figure 6.4c shows a sample dealloyed for 10 min and tilted 20°, allowing the film surface to be viewed along with the cross section. Figures 6.4b-c reveal that the np-Au layer adheres well to the pure Au interlayer (the continuous, bright line indicated by the white arrow in Figure 6.4b). After 1 min dealloying, the nanoporous structure has already developed throughout the entire film thickness (see Figure 6.4b), in agreement with findings by Erlebacher et al. [8]. The major cracks that were seen in Figures 6.1-3 extend through the film thickness and end at the Au interlayer, as shown clearly in Figure 6.4c, where it is also seen that many of these large cracks have a wedge shape after 10 min of dealloying. However, after 1 min dealloying, some film cracks appear to be buried within the film thickness, or even to extend from the Au interlayer toward the film surface (see Figure 6.4b, to the left of the white arrow). It should be noted that the large, wedge-shaped cracks seen in Figure 6.4c are also observed after 1 min of dealloying at numerous other locations. Figure 6.4b is included here to illustrate that there is a small additional population of cracks located in the film interior and/or at the bottom of the np-Au film. Finally, the thickness of the np-Au film in sample S11 after dealloying was measured from cross-sectional images such as those in Figure 6.4. Following dealloying for 1 to 10 min, the average thickness as measured by SEM was 331 nm. This is significantly less than the 382 nm alloy film thickness measured from Figure 6.4a

(compare to the calculated thickness of 387 nm) before dealloying. Although the film structure before dealloying (Figure 6.4a) may not appear as clearly columnar as after dealloying (Figures 6.4b-c), cross-sectional focused ion beam imaging of similar films reveals columnar grains. All films were sputtered with identical deposition parameters (except deposition time), but the contrast in SEM images of alloy films is simply lower than in images of nanoporous films and the microstructure in Figure 6.4a is thus not as obvious.

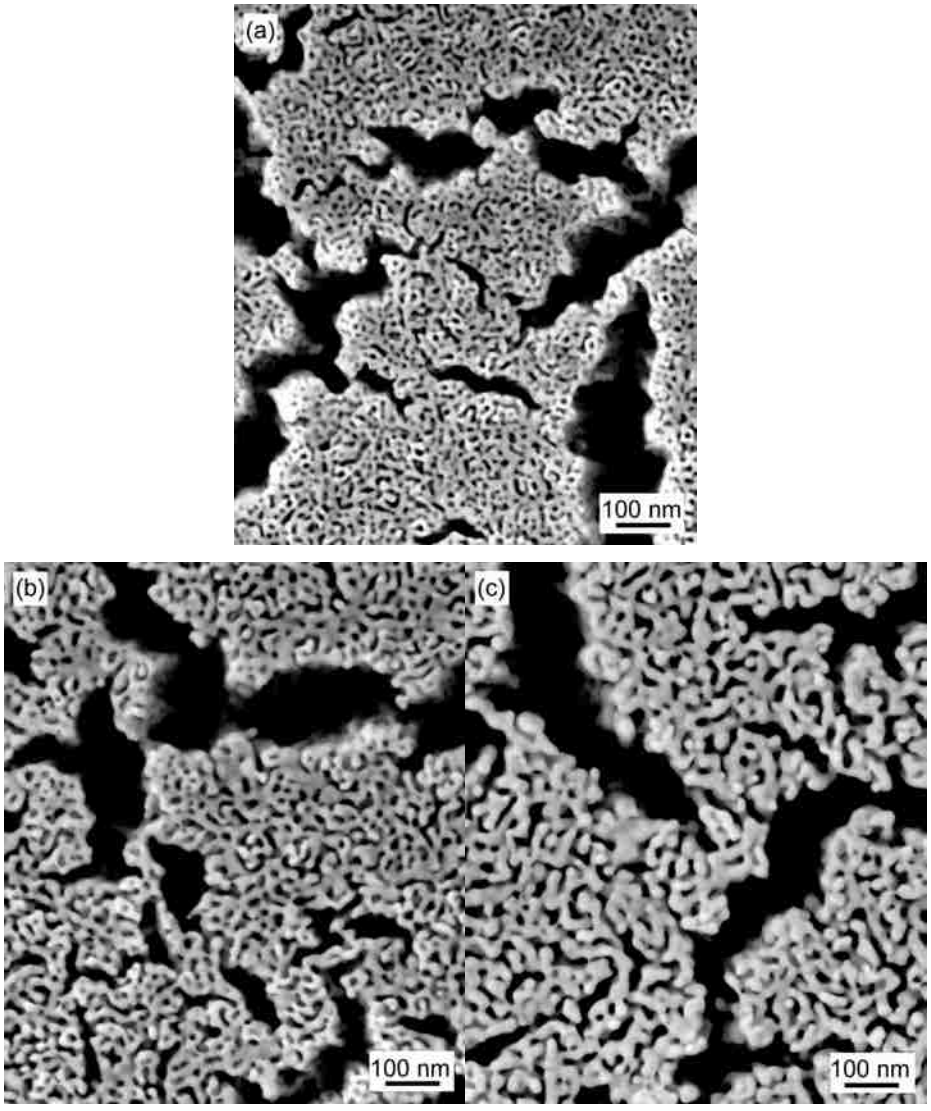

Figure 6.3 SEM images of nanoporous structure in a 387 nm np-Au film on Si substrate (S9, with 10 nm Ta and 10 nm Au interlayers) after dealloying times of (a) 1 min, (b) 10 min, (c) 100 min.

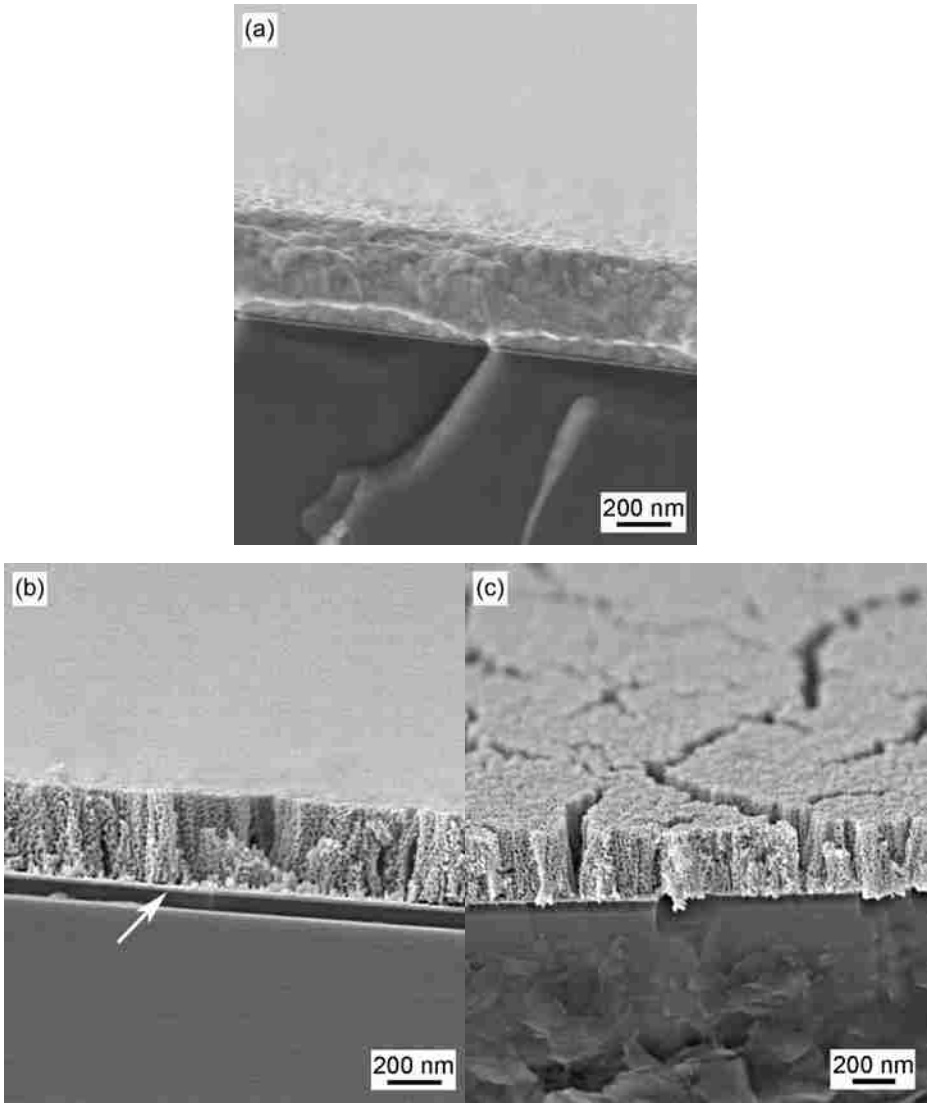

Figure 6.4 Cross-sectional view of sample S11 (from a 387 nm Au-Ag alloy film) at different dealloying times and tilt angles. (a) As-sputtered film before dealloying. (b) 1 min dealloying and almost no tilt (viewed edge-on). (c) 10 min dealloying and 20° tilt, allowing the film surface and crack pattern to be seen clearly. After 10 min dealloying, most cracks extend from the film surface to the substrate, although after 1 min dealloying, a small number of cracks are seen to start at the film/substrate interface and terminate within the np-Au film.

Measurements of the average spacing of large ("major") cracks in samples G1 and S9, presented in Table 6.2, revealed that the crack spacing is two to three times the alloy film thickness. This is much larger than the ~50 nm grain size (see Figure 6.4a). In an earlier study of np-Au thin films, it was observed that preferential dealloying occurred at grain boundaries, even in films where the Au content was too high for complete dealloying of the film to occur [90]. Thus, it appears that preferential dealloying may occur only at certain grain boundaries in the film, leaving clusters of attached grains between the large cracks (Figures 6.2 and 6.3). In the current study, the width of major cracks was measured, and this width appears to scale with the crack spacing. As indicated in Table 6.2, the ratio of crack width to crack spacing is approximately 9%.

Table 6.2 Spacing and width of large ("major") cracks in films of different thickness. The width of major cracks appears to be proportional to crack spacing.

Sample	Au-Ag alloy film thickness (nm)	Avg. major crack spacing (nm)	Avg. major crack width (nm)	Ratio of crack width to spacing
G1	130	300	28	0.093
S9	387	1100	94	0.085

At several stages of dealloying, Ag content in the alloy/np-Au film was measured by EDS. The relative amounts of Au and Ag in each analysis were corrected for the presence of the pure Au interlayer, in order to obtain the composition within the np-Au only. Additionally, SEM micrographs from these same samples were analyzed to determine ligament width. In each case, at least 100 ligaments were measured in order to obtain a statistically significant measure of their size. Ligaments were measured at their midpoint, as this region typically has the smallest diameter and should therefore be important in understanding ligament failure. The variation in Ag content and ligament width of np-Au as a function of dealloying time is shown for three 387 nm np-Au samples in Figure 6.5. Note that the error for Ag content is ±1%, approximately the same size as the data points in Figure 6.5. For ligament width, the 95% confidence interval, taken as the range of true values, is nearly constant at ±1.2 nm. When the film was dealloyed for 30 min, Ag content decreased from 76 at.% to 4 at.%. This trend in the

evolution of Ag content with dealloying time is consistent with results of another study [76], although the initial alloy composition and timescale for dealloying were different in that study. As opposed to those results, the plot of Ag content in Figure 6.5 focuses on the earlier stages of dealloying. Over a total dealloying time of 100 min, ligament width increased by 85%, from 8.7 nm to 16.1 nm. Ag loss occurs immediately during dealloying, and seems to precede ligament coarsening (ligament width remains nearly constant at 8.7-8.8 nm in the first minute of dealloying, whereas more than 75% of the initial Ag is lost in this time). This decay in Ag content agrees well with that observed in sample G1 (130 nm np-Au sample on glass) reported in a preliminary study [84].

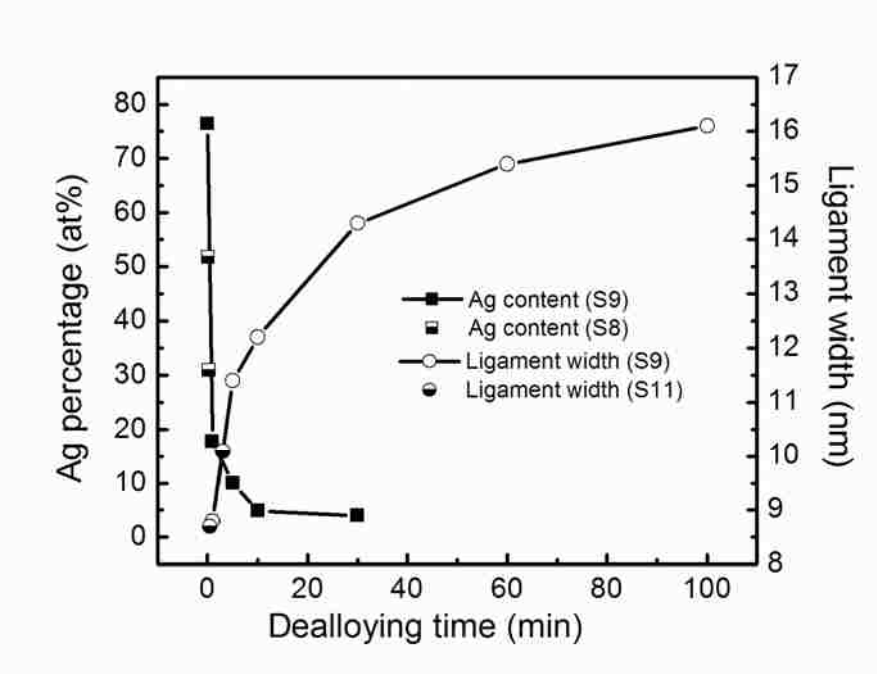

Figure 6.5 Changes in composition and ligament width during dealloying of three 387 nm np-Au films on Si (S8, S9 and S11). The data from both samples agree well with each other. Ag content decreases immediately and rapidly, while ligament width increases noticeably after 1 min dealloying.

6.3.2 Stress evolution during dealloying

The evolution of stress in a 387 nm np-Au film on Si (sample S11) was measured by wafer curvature at several stages of dealloying and is shown in Figure 6.6a for times up to 10 min. Also plotted here are the data for Ag content (samples S8 and S11), as

determined by EDS, over the same time period. The Ag content data are similar to those in Figure 6.5 (for samples S8 and S9) and show in greater detail the film composition during the initial stages of dealloying. For film stress, the total error is estimated at 4.6%, including uncertainty in film thickness measurement (2.0%), accuracy of substrate curvature values (2.0%), and natural scatter of repeated curvature measurements on the same sample (0.6%). From Figure 6.6a, it is clear that dealloying of the np-Au thin film is very rapid, with more than 75% of the Ag being removed in the first minute. Moreover, both Ag content and film stress decrease in a similar fashion during dealloying. After 5 min, both have nearly reached their steady-state minima of ~7 at.% Ag and ~8 MPa stress. The rapid relaxation of film stress is illustrated in more detail in Figure 6.6b, which shows the evolution of stress during the initial stages of dealloying (up to 90 sec) for sample S8. Film stress drops quickly and reaches a plateau of ~20 MPa within the first minute of dealloying.

Stress evolution curves during longer-term dealloying of 112 nm and 387 nm thick np-Au films (samples S12 and S9) are shown in Figure 6.7. These specimens were dipped into liquid nitrogen before dealloying, in an attempt to induce a compressive stress state and minimize cracking during dealloying. This attempt was unsuccessful, and these samples exhibited the same degree of cracking as all others (e.g. Figure 6.3). Note that for sample S9 (the 387 nm film), samples for characterization were processed with and without a liquid nitrogen dip before dealloying. SEM images showed no difference in nanoporous structure of films that underwent liquid nitrogen immersion, so the microstructure for the film referenced in Figure 6.7 is accurately portrayed by the images in Figure 6.3. For both films in Figure 6.7, the liquid nitrogen dip caused film stress to decrease by 15-17 MPa. In the case of the 112 nm film, this was enough to induce a net compressive stress in the Au-Ag alloy. Furthermore, the 112 nm film exhibited an intermediate peak in stress (27 MPa) at 5 min dealloying time, after which stress decreased monotonically. However, these differences in film stress behavior did not affect the final stress of np-Au after complete dealloying. Stress in both np-Au films decreased with dealloying time beyond 10 min, and after 100 min, the tensile stress dropped nearly to zero (<1 MPa).

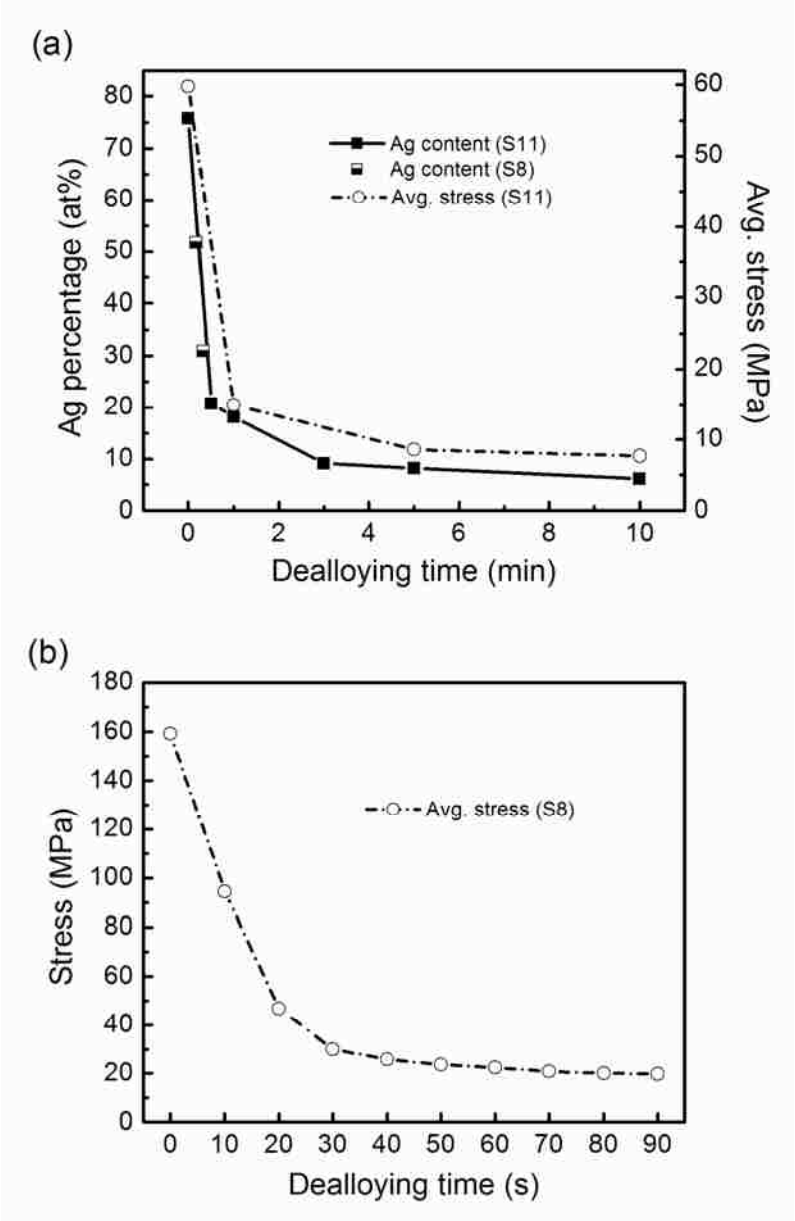

Figure 6.6 (a) Evolution of Ag content and stress in two 387 nm np-Au films on Si (S8 and S11) with dealloying time. Both Ag content and film stress decrease in the same manner, rapidly approaching their steady-state minima. (b) Evolution of stress at short dealloying times for a 387 nm np-Au sample (S8). Film stress exhibits a plateau at ~20 MPa, similar to S11 in (a).

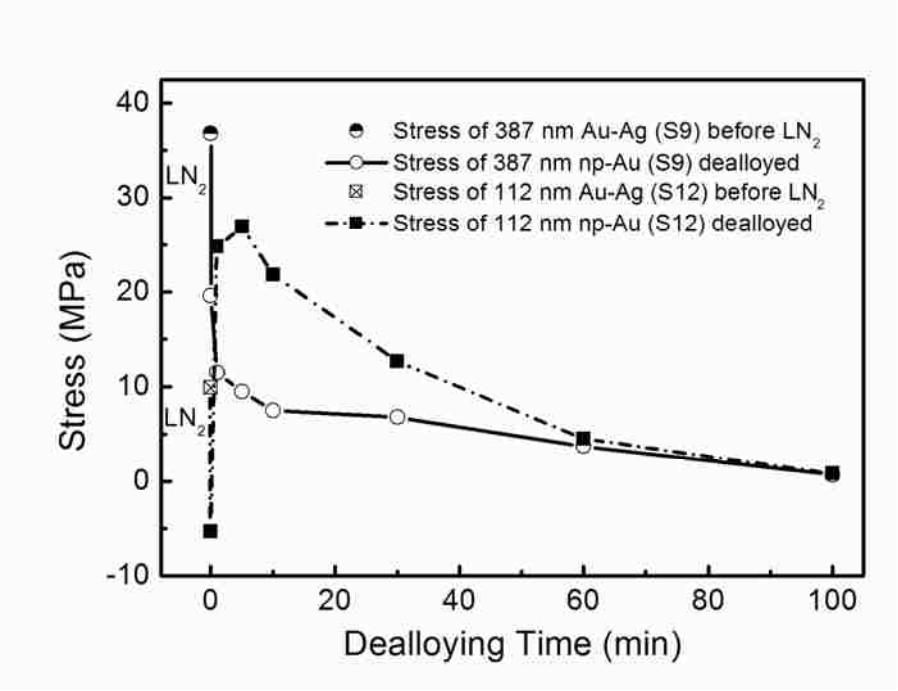

Figure 6.7 Stress evolution of np-Au films on Si (S9 and S12) as a function of dealloying time, following immersion in liquid nitrogen before dealloying. Stresses in the Au-Ag alloy films dropped by 15-17 MPa when they were dipped into liquid nitrogen and decreased with prolonged dealloying time. Note that sample S12 entered compression due to the liquid nitrogen dip, then exhibited an increase and subsequent decrease in film stress during dealloying.

No compressive stress was measured in either film after dealloying began. Cracking occurs immediately upon dealloying, but film stress decreases to zero only after extended times. Overall, it appears that dealloying causes stress relaxation, as opposed to the generation of tensile stresses that one could reasonably expect based on volume contraction [53].

6.3.3 Thermal cycling behavior

The stress-temperature plot for a 387 nm np-Au film on Si substrate (sample S11), which was dealloyed for 10 min and then thermally cycled, first to 100 ˚C and then to 200 ˚C, is shown in Figure 6.8. The initial room temperature stress in this film was ~3 MPa, which was 5 MPa lower than the stress measured after 10 min dealloying in Figure 6.6 (some additional stress relaxation may have occurred before thermal cycling experiments were performed). Overall, the film exhibits no temperature-dependence of

stress. Although film stress may appear to increase slightly during heating to both 100 and 200 ˚C, these changes are minimal, with a total variation in stress of <10 MPa. They appear to lie within the error of the wafer curvature system and therefore are more useful as an indication of the scatter in stress measurement during thermal cycling. Based on thermal cycling studies of another np-Au film system [82], the nanoporous structure is expected to be stable during heating up to 200 °C, with some additional coarsening of ligaments but without loss of the open porosity.

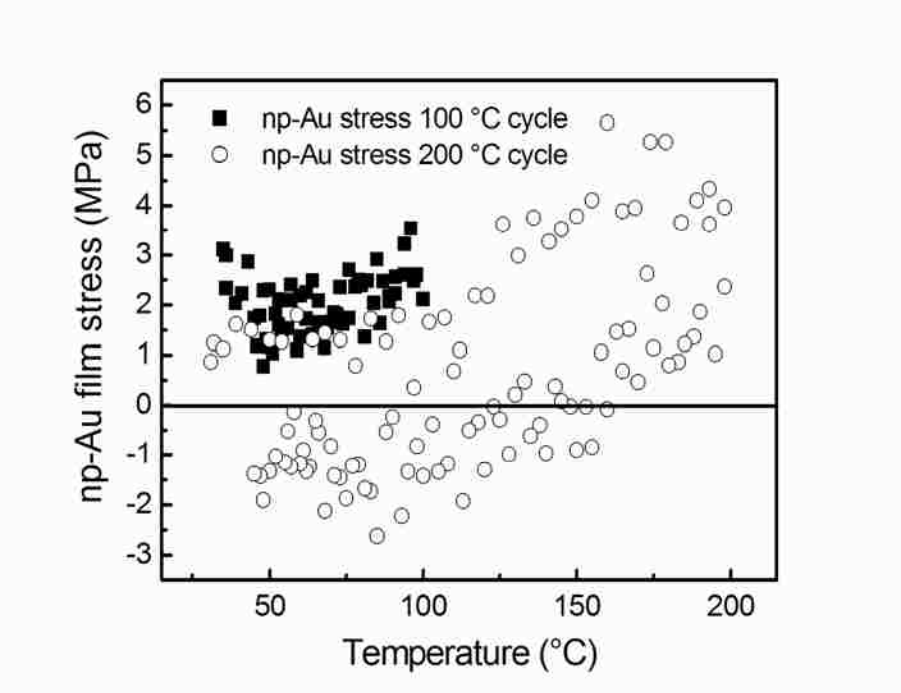

Figure 6.8 Stress-temperature curves of a 387 nm np-Au film on Si (S11). For the 100 °C thermal cycle, film stress fluctuates around 2 MPa, while the stress varies around zero during the 200 °C cycle. The total fluctuation is less than 10 MPa for both cycles.

6.4 Discussion

During dealloying of np-Au thin films, several observations were made that not only indicate which compositional and microstructural changes occur, but also reveal the time sequence of their progression. This allows speculation on how these various changes may be connected to one another.

During dealloying, significant volume contraction occurs and should generate tensile stresses in the np-Au films. However, extensive cracking of the film takes place at the grain boundaries and should relieve film stress. This appears to be the case for almost all of the films studied here, except for the 112 nm film subjected to a liquid nitrogen dip (discussed in section 6.4.3 below). Overall, relaxation processes including cracking, Ag depletion and ligament coarsening dominate the evolution of stress in these films.

6.4.1 Volume contraction during dealloying

First, consider the amount of volume contraction measured in the np-Au films on Si. As shown by the data in Table 6.2 and the micrographs in Figures 6.2-3, the ratio of major crack width to crack spacing is approximately 9%. This can be interpreted as the linear shrinkage (i.e. along one dimension) of the film plane during dealloying. However, as was shown in Figure 6.4, major cracks have a wedge shape, and thus the average crack width through the film thickness is only half that measured at the surface. The average linear contraction is therefore more properly estimated as 4.5%. Moreover, since this linear contraction occurs in two dimensions in the plane of the film, this implies a biaxial contraction of ~9%.

To determine the total volume contraction, one must also consider the reduction in thickness caused by dealloying. As was shown in Figure 6.4, cross-sectional SEM measurements of dealloyed np-Au thin films revealed that the film thickness decreased significantly, e.g. from 382 nm to 331 nm for sample S11. This corresponds to a thickness contraction of ~13% in this sample. When this thickness contraction is considered along with the ~9% biaxial contraction in the plane of the film, which was attributed to the grain boundary cracks discussed above, a total volume contraction of 21% is calculated ($1 - 0.91 \bullet 0.87$). This agrees well with the findings of Parida et al. [53], who observed that dealloying of bulk Au-Ag alloys resulted in volume shrinkage of up to 30%. In contrast, Dixon et al. measured lower thicknesses for np-Au films than for their alloy films, but attributed the possible thickness variations to sputtering conditions rather than the dealloying process itself [76]. Nonetheless, the films in the present study, which have a lower Au content that appears to lead to film cracking, exhibited a consistent thickness reduction that can be explained by dealloying. The film cracks shown in Figures 6.1-6.4 appear to partially accommodate the total shrinkage during dealloying,

while preserving the lateral overall sample dimensions and allowing the blanket np-Au film to remain attached to the substrate across its width/diameter.

Along with the volume contraction that occurs during dealloying, the relative density of np-Au changes with respect to the value one would expect based on initial alloy composition. Relative density is simply the density of a porous material relative to that of the fully dense bulk material. Since Au and Ag have nearly identical lattice parameters [80], the volume/thickness percentage of Au in the precursor alloy is taken to be the atomic percentage of Au in the Au-Ag alloy, i.e. 24.3% in the current study. If dealloying simply removed the Ag atoms and did not change the overall film dimensions (or cause cracking), the relative density of the np-Au films would also be 24.3%. However, the 21% total volume contraction measured here implies that the actual relative density is higher. The corrected value should thus be 0.243/0.79, or 31%.

6.4.2 Time dependence of ligament coarsening

A significant finding of this study is that Ag loss does not occur simultaneously with ligament coarsening. Instead, the most rapid rates of Ag depletion appear to precede ligament coarsening, although there is some overlap between the two. As was shown in Figures 6.5 and 6.6a, significant coarsening of np-Au ligaments begins after 1 min, when over 75% of the initial Ag content has been removed. This finding does not appear to be due to a discrepancy between surface observations from SEM images and through-thickness chemical analysis with EDS, since the film surface should either have the same dealloyed composition as the film interior or, perhaps, a slightly lower Ag content. As was shown in Figure 6.4, porosity is uniform throughout the film thickness at dealloying times of 1 and 10 min, suggesting that Ag content is also uniform through the thickness. Even if the curves in Figure 6.5 are indeed affected by a surface-versus-interior discrepancy, the curve representing Ag content may need to be shifted down and/or to the left, in order to obtain a lower Ag content at the film surface for comparison with SEM measurements of ligament width. This would still support, and indeed strengthen the claim that ligament width increases after Ag depletion is nearly complete.

In addition to the observation that most Ag depletion occurs before ligament coarsening, Figures 6.5-6.6 indicate that relaxation of film stress also precedes any significant increase in ligament width. The rapid, substantial decreases in Ag content and

film stress are concomitant, and thus the initial reorganization of Au atoms into fine nanoscale ligaments occurs simultaneously with the measured stress reduction. With regard to a mechanism for ligament coarsening, film stress is not expected to play a dominant role. Nonetheless, extended dealloying (beyond 10 min) does lead to ligament coarsening and further relaxation until the film is nearly stress-free, so film stress may provide a small contribution to ligament coarsening. Alternatively, a nearly stress-free state may facilitate coarsening; a substantial tensile stress, which decreases in accord with Ag content, could counteract the driving force for ligament coarsening and thereby delay the onset of coarsening until stress has dropped to a threshold value that happens to coincide with nearly complete Ag depletion. Thus, it may be a combination of lowered Ag content and/or film stress that is a prerequisite for ligament coarsening.

The finding that Ag depletion precedes ligament coarsening may also be due to the fast dealloying time, which in turn is due to the low film thickness and correspondingly short distance over which mass transport of depleted Ag must occur. Nonetheless, this apparent distinction between Ag loss and increase in ligament width allows determination of the time dependence of Au ligament coarsening in np-Au films.

The ligament coarsening discussed here is that which occurs after almost all Ag has been removed, so-called "post-etch coarsening" [49]. During dealloying, the coarsening of ligaments is due to the diffusion of Au atoms and is driven by capillarity, i.e. reduction in surface energy, as discussed by Erlebacher [48]. Presumably, capillarity is also the driving force in the post-etch coarsening regime, with surface diffusion of Au creating thicker ligaments.

Consider the time dependence of ligament coarsening measured for a 387 nm np-Au film (sample S9). As was shown in Figure 6.5, average ligament width (measured at the midpoint) increased monotonically from 1 min dealloying time to 100 min. Based on this plot, it appears that the ligament width has nearly reached a steady-state maximum of 16-17 nm. This data has been plotted again in Figure 6.9, where a log-log plot of width versus time shows a clear trend in this coarsening regime. Between 1 and 100 min dealloying time, ligament width w exhibits a time dependence $w \propto t^{0.13} \approx t^{1/8}$. The rate of ligament coarsening therefore decreases very quickly with time, and ligaments approach a steady-state size within a relatively short time interval. For this reason, and given the

rapid penetration of etchant through the film at the beginning of dealloying, ligament width is consistent throughout the nanoporous structure.

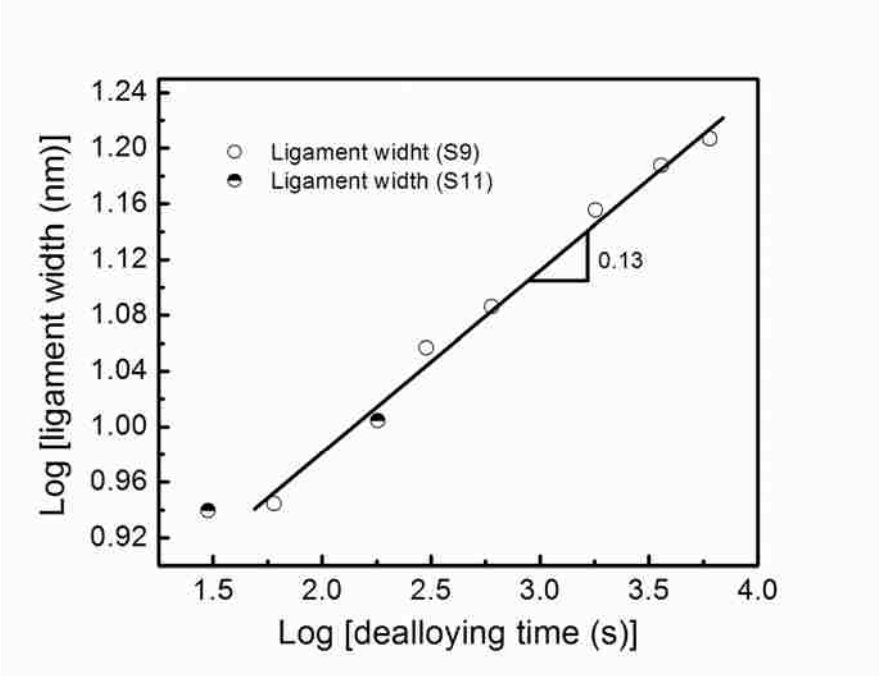

Figure 6.9 Log-log plot of ligament width w versus dealloying time for samples S9 and S11, using the data from Figure 6.5. For dealloying times longer than 1 min, i.e. once the majority of Ag has been depleted and film stress has nearly been relaxed, the ligament width scales with time according to $w \propto t^{0.13} \approx t^{1/8}$.

The time dependence of ligament coarsening observed in this study cannot be explained on the basis of existing models, although a surface diffusion model for sintering does come close and should be very relevant to this process. First, in the case of second-phase particle coarsening (within a parent matrix) due to capillary forces, which is driven by a reduction in total interfacial energy, the radius R exhibits an Ostwald ripening dependence $R \propto t^{1/3}$ [91]. Since this is clearly different from np-Au ligament coarsening, it is not surprising that it differs from the $t^{1/8}$ time dependence observed here. Second, if a coarsening model based on surface diffusion is considered, e.g. for two spherical particles that undergo neck growth during sintering, a time dependence $w \propto t^{1/5}$ is obtained for the increase in thickness w of the neck region between the two particles [91]. This is closer to the ligament coarsening observed here, but still does not match the $t^{1/8}$ dependence. One reason for this lack of agreement may be that, in the sintering

model, the centers of the two particles are assumed to remain at a constant distance. However, during coarsening of np-Au, the average distance between nodes (i.e. the length of the ligaments) increases along with the ligament diameter.

Nonetheless, the sintering model does contain certain important features that apply to the coarsening of np-Au ligaments. In both cases, surface diffusion drives atoms toward the midpoint of each ligament by capillarity. In the sintering model, the rate-limiting flux occurs as one-dimensional surface diffusion along the length of a cylinder of uniform radius, yielding the $w \propto t^{1/5}$ dependence. Besides the geometric differences between ligament coarsening and particle sintering, the presence of the small tensile stress in the np-Au film may play a role. In the current study, coarsening appears to occur in the absence of significant stress, although a slight tensile stress does persist throughout the time interval in Figure 6.9. A tensile stress would tend to make the ligaments thinner and would thus counteract the capillarity-driven coarsening, requiring longer times for a given increase in diameter. Thus it may be possible, using a new model, to describe the experimental time dependence $w \propto t^{1/8}$ found here. This will be examined in more detail in a future study.

6.4.3 Dealloying-induced stress changes

It was observed that film stress decreases in accord with Ag content during the first 10 min of dealloying. The correlation between stress and Ag content, e.g. as shown in Figure 6.6a, is very strong and suggests that the two are coupled. A simple interpretation of this correlation is that the depletion of Ag exposes a high concentration of Au atoms on the surface of the eroding alloy, followed by surface diffusion and agglomeration of Au into stress-free ligaments. Since the Au atoms form a completely new structure (the ligaments), this would presumably relax the pre-existing stress in the Au-Ag alloy, at least partially. Thus, total film stress would decrease as long as Ag is removed during dealloying. As discussed below, however, it appears that the reduction in stress can be attributed to film cracking.

Within the first minute of dealloying, at least three changes occur: (i) Cracks appear in all films (Figures 6.1a-b, 6.2a, 6.3a). (ii) Pores form throughout the film thickness (Figure 6.4b). (iii) Film stress and Ag content decrease by more than 75%

(Figure 6.6). Dealloying, which necessarily involves the depletion of Ag and the formation of pores, should generate tensile stresses within the evolving nanoporous structure due to overall volume contraction [53]. However, average film stress instead decreases. As discussed in the previous paragraph, this may be partly due to reorganization of Au atoms. However, it is more likely due to the extensive cracking that occurs at grain boundaries, at least at the beginning of dealloying when cracking occurs and the largest decrease in film stress is measured. The cracks are most likely stress-free, thereby relieving stress over an area fraction at least as large as the areal crack density (~9%, accounting for the wedge shape of the cracks). This would offset the tension that may develop within np-Au ligaments in the regions away from cracks, and lead to a lower average film stress. Therefore, measurements of stress in dealloyed thin films provide a lower bound for the actual np-Au biaxial stress, and most likely substantially underestimate that actual stress.

As was shown in Figure 6.6, most of the eventual Ag depletion and stress relaxation occurred in the first minute of dealloying. Within the same time interval, extensive cracking also occurred (see Figure 6.3). In a separate study of crack-free np-Au films [72] the dissolution of Ag was accompanied by an increase in stress, instead of the relaxation observed here, implying that the initial formation of nanoporous structure does not reduce film stress. It is therefore proposed that the tensile stress expected from the dealloying process was relaxed by cracking in the films studied here. The amount of stress relaxation due to crack formation can be estimated from equations proposed by Freund and Suresh based on finite element modeling [92]. According to their model, the curvature change of a cracked film can be estimated by the ratio of film thickness to crack spacing. In the case of np-Au films, these ratios are 0.35 and 0.43 for samples S9 and G1, respectively (see Table 6.2). A reduction in substrate curvature (or, equivalently, film stress) of 95% to 100% is calculated, which agrees well with measurements of stress evolution during dealloying (Figures 6.6-6.7). Technically, the 95-100% reduction in biaxial curvature (film stress) applies to an array of parallel cracks (not a two-dimensional crack pattern such as that in an np-Au film), but this calculation can be used as a first-order estimate of the biaxial curvature reduction and indicates that an equivalent one-dimensional crack array would reduce virtually all of the film-stress-induced

substrate curvature. The film stress would therefore be expected to drop almost to zero, as was measured here.

Nonetheless, since grain boundary cracking occurs immediately during dealloying, the stress evolution can be used to calculate the minimum stress that must be present in np-Au ligaments. The highest film stress measured during dealloying was 27 MPa, as shown in Figure 6.7 for the 112 nm film (sample S12) after 5 min. Even for a thicker film (e.g. the 387 nm film in Figure 6.6a), 5 min dealloying is sufficient to reduce Ag content almost to the steady-state minimum. For the 112 nm film, therefore, it is expected that nearly all Ag has been depleted by 5 min, and that the 27 MPa stress is carried by a relatively pure np-Au film. The Gibson-Ashby scaling law [52] describes the strength of an open-cell porous material as $\sigma_y = C_1\sigma_s(\rho_{np}/\rho_s)^n$, where σ_s and ρ_s are the yield strength and density of solid Au, and ρ_{np} is the density of np-Au. C_1 and n are empirical constants, with $C_1 = 0.3$ and $n = 3/2$. As discussed above, ρ_{np}/ρ_s is the relative density of the dealloyed np-Au film and is nominally 0.243 (equal to the atomic percentage of Au in the initial alloy), with a corrected value of 0.31 (accounting for volume contraction). Using the Gibson-Ashby scaling law and the *corrected* relative density, the minimum equivalent bulk stress that evolved during dealloying of the 112 nm film is 520 MPa. This stress is significantly lower than the value of 750 MPa that would be calculated using the uncorrected relative density. Nonetheless, an equivalent bulk stress of 520 MPa is very high for Au, especially considering that this estimate provides a lower bound to the actual stress that evolves in the crack-free regions of np-Au during dealloying.

6.5 Summary

Nanoporous Au thin films on glass and on Si substrates were fabricated by dealloying precursor Au-Ag alloy films, which had an initial Au content of ~25 at.%. Adhesion of np-Au to both substrate types was significantly enhanced by depositing a Au interlayer before alloy deposition and, for Si substrates, a Ta interlayer beneath the Au. Pore formation during dealloying was rapid, producing a nanoporous structure throughout the film thickness within 1 min. Further dealloying caused the structure to coarsen.

Film cracking was prevalent in all np-Au films produced from the 25 at.% Au precursor alloy, and is likely due to preferential dealloying at certain grain boundaries. The cracks formed very quickly, many within the first minute of dealloying, and are believed to play an important role in the stress evolution of np-Au during subsequent dealloying and thermal cycling. The cracks should be stress-free, thereby lowering the average film stress measured across the entire wafer. Nonetheless, scaling laws predict that an equivalent bulk stress of at least 520 MPa evolves during dealloying of a 112 nm film. Thermal cycling of thin films did not induce a significant stress in the np-Au, perhaps due to the extensive film cracking that may have accommodated any expansion or contraction of the film.

Both Ag content and film stress decreased significantly and rapidly during dealloying, and these changes occurred before ligament width began to increase appreciably. Dealloying generally caused cracking, followed by subsequent stress increases and then stress relaxation, eventually leading to a stress-free state at extended times. Calculations indicate that film cracking could account for the measured stress relaxation. Finally, ligament width was found to increase with dealloying time according to $w \propto t^{1/8}$. This differs from existing models for other processes driven by surface diffusion, and may be due to geometric differences and/or the presence of a small tensile stress in the np-Au films.

Chapter 7

Microstructure, Stability and Thermomechanical Behavior of Crack-Free Thin Films of Nanoporous Au

Part of this chapter is based on the following published manuscripts:
Ye Sun, Jia Ye, Zhiwei Shan, Andrew M. Minor, T. John Balk, *The Mechanical Behavior of Nanoporous gold Thin Films*, JOM **59**(9) 54-58 (2007), copyright of 2007 by Springer Science and Business Media.

Ye Sun, Kalan Kucera, Sofie Burger and T. John Balk, *Microstructure, Stability and Thermomechanical Behavior of Crack-Free Thin Films of Nanoporous gold*, Scripta Materialia **58** 1018-1021 (2008), copyright of 2008 by Elsevier.

7.1 Introduction

Nanoporous noble metals possess chemical properties and a high surface-to-volume ratio that make them promising candidates for a variety of applications, including actuators [27], sensors [31] and catalysts [37]. Fabrication of noble metals with a nanoporous structure proceeds via a process known as *dealloying*, during which the less noble atoms (e.g. Ag) are chemically or electrochemically dissolved from a precursor alloy (e.g. Au-Ag). As the less noble atoms are leached from the alloy, the more noble atoms (e.g. Au) undergo surface diffusion and agglomeration, ultimately yielding a nanoscale, sponge-like structure consisting of nearly pure metal (Au) ligaments and open, interconnected pits [8, 49]. The length scale of the ligaments and pits within nanoporous metals can be readily tailored, from several nanometers up to microns in size, by varying the initial alloy composition, dealloying time and/or applied potential, or by subsequent heat treatment [63].

Recently, the mechanical properties of np-Au have drawn increasing attention [55, 64, 75]. The strength of nanoscale Au ligaments measured by nanoindentation was

reported to approach or even exceed the theoretical yield strength of bulk Au [55, 61]. Some researchers found that the ligament strength followed a Hall-Petch-type relationship with ligament size [60, 62]. Although much work on np-Au has focused on bulk material, several studies have addressed the behavior of thin film np-Au and have also revealed high strength levels compared to bulk Au [66, 68, 89]. However, it is still unknown which mechanism(s) govern deformation within nanoscale ligaments. Detailed studies of the behavior of dislocations and other defects are needed in order to understand the structure-property relationships that lead to the high equivalent strength levels of np-Au.

7.2 Experimental

The Au-Ag films used in this chapter (Au-70 at.% Ag) were sputtered at room temperature in a high vacuum chamber (AJA ORION system, base pressure better than 10^{-6} Pa) onto (100)-oriented silicon wafers (CrysTec GmbH, Germany) to thicknesses of 75 nm to 1 μm. Dealloying was performed with stock (70%) HNO_3. Some samples were dealloyed by free corrosion, while others by multiple stages dealloying, which combined free corrosion and electrochemical dealloying. Electrochemcial dealloying was performed using a simple galvanostatic electrochemical cell with a DC power supply (Extech 382285).

Wafer curvature measurements were performed (FLX-2320-S, Toho Technology Corporation) to determine film stress. Diametric scans were taken at 15° intervals to generate a three-dimensional stress map and obtain an average stress value representative of the entire film after each time of dealloying. Samples were thermally cycled to 200°C and then cooled to -70 °C and stress was measured with a selected reference angle. Morphology of the sample surface before and after dealloying was observed with scanning electron microscopes (Hitachi S900 SEM). Micrographs were analyzed to measure the width of np-Au ligaments. For each stage of dealloying, an average value was calculated from ~100 measurements of individual ligaments in SEM images. Residual Ag content with dealloying time was analyzed by energy dispersive spectrometry (EDS) system associated with the SEM (Hitachi S3200).

7.3 Results and discussion

7.3.1 Thermo-mechanical behavior of np-Au films

Thin film np-Au samples were subjected to thermal cycling in order to study the stress evolution and to determine the maximum stresses that can be generated in the films. Figure 7.1 shows stress-temperature curves for three np-Au films during cooling from 200˚C to -70˚C. Based on previous work with similar samples, it is known that the ligament width doubles (from ≈15 nm to ≈30 nm) during thermal cycling between 200˚C and room temperature. Thus, for the curves shown in Figure 7.1, it is assumed that a constant ligament width of ≈30 nm exists within all three films during cooling (no change in ligament width is expected during cooling from the maximum temperature). From Figure 7.1, it is apparent that thinner films carry higher stresses when subjected to the same thermal cycling temperature range.

Unlike solid metal films, for which stress varies inversely with film thickness due to geometric constraints that cause dislocation channeling [79], the strength of nanoporous metal films was expected to depend on ligament size, as was found for bulk np-Au [55, 60]. Overall, it is expected that the smallest geometric parameter, e.g. film thickness, grain size, ligament width, etc., will most heavily influence the nucleation and motion of dislocations and hence the film strength. Thus, it would be expected that the three films shown in Figure 7.1, all of which should have a ligament width of ≈30 nm, would exhibit similar stress-temperature behavior and the same maximum stress. But in this study, np-Au films were seen to behave more like solid films, with an inverse relationship between film thickness and stress after thermal cycling.

Based on the curves shown in Figure 7.1, it appears that the np-Au films exhibit thermoelastic stress-temperature behavior during the final stages of cooling to -70˚C. In this case, the films would not have reached their yield points, and the unexpected trend of increasing film stress with decreasing film thickness could have a different explanation. From Gibson & Ashby's scaling law [52], the yield strength of an open-cell foam is given by $\sigma_y = C_1 \sigma_s (\rho_{np}/\rho_s)^n$, where σ_s and ρ_s are the yield strength and density of solid Au, and ρ_{np} is the density of np-Au. C_1 and n are empirical constants, with $C_1 = 0.3$ and $n = 3/2$. ρ_{np}/ρ_s is termed the *relative density* of np-Au and is equal to the volume/thickness

percentage of Au in the precursor alloy (which in turn is taken to be the atomic percentage of Au in the Au-Ag alloy, due to the nearly identical lattice parameters of Au and Ag). In the current study, the theoretical relative density is 30%, assuming no volume contraction during dealloying. However, based on TEM images of film-on-wedge samples for *in situ* nanoindentation, which reveal the thickness of the dealloyed np-Au layer, the actual relative density appears to be higher (36%), due to contraction of the film thickness.

Since all films appear to have undergone thermoelastic deformation and presumably never reached their yield points during cooling, it follows that the actual yield strength of np-Au films should be higher than the maximum biaxial stresses shown in the stress-temperature curves of Figure 7.1. Thus, it is possible to calculate a lower bound for the equivalent bulk yield strength of the Au ligaments for each film. The results of these calculations using the Gibson-Ashby equation are shown in Table 7.1, along with the maximum film stress measured at the end of thermal cycling. These calculated stress levels, assumed to represent a lower limit for the equivalent yield strength, are already very high and approach the theoretical yield strength for bulk Au, in general agreement with other studies [62] but still predicting lower strength levels.

For proper comparison with the theoretical shear strength, the calculated equivalent stress levels in Table 7.1 should be converted into resolved shear stresses. The thin films are highly {111}-textured and therefore have a Schmid factor of 0.27. Taking the maximum value of 2.0 GPa (using the corrected relative density of 36%) from Table 7.1, the equivalent resolved shear stress at the end of thermal cycling is found to be 550 MPa. Estimates of the theoretical shear strength range from a maximum of $\mu/2\pi$ to a more realistic value $\approx\mu/30$ [93]. Using a shear modulus $\mu = 27$ GPa for Au [93], the theoretical shear strength is expected to lie between 900 MPa and 4.3 GPa. For the 75 nm np-Au film in this study, the calculated equivalent shear stress of 550 MPa corresponds to $\approx\mu/49$, which is approximately 60% of the realistic estimate of the theoretical shear strength for Au.

Table 7.1 Maximum biaxial film stress of np-Au films during thermal cycling and the corresponding equivalent bulk yield strength, calculated from the Gibson-Ashby scaling law using both theoretical relative density (0.30) and corrected relative density (0.36).

np-Au film thickness (nm)	Maximum film stress (MPa)	Equivalent bulk yield strength [$\rho_{np}/\rho_s = 0.30$] (GPa)	Equivalent bulk yield strength [$\rho_{np}/\rho_s = 0.36$] (GPa)
300	80	1.6	1.2
150	100	2.0	1.5
75	132	2.7	2.0

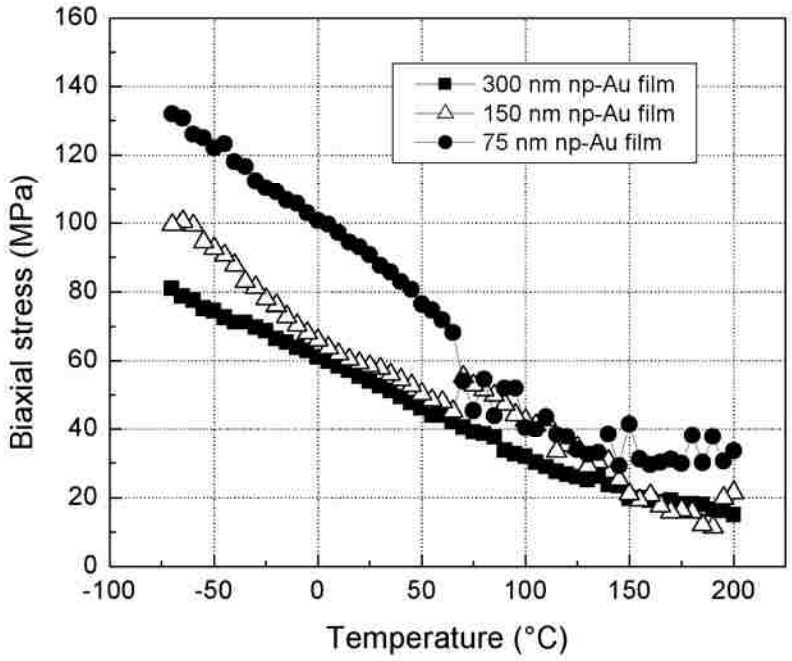

Figure 7.1 Cooling segments from the stress-temperature curves of np-Au films thermally cycled between 200°C and -70°C. Thinner films support higher stresses, even though all films have the same ligament width.

7.3.2 Thermal behavior of 75 nm np-Au films

A significant result of this chapter is that Au-70 at.% Ag films were dealloyed to produce np-Au films that exhibited uniform nanoporosity and were completely free of cracks. The absence of cracks should impart higher strength, as compared to np-Au films that were prepared from alloys with lower Au content and that exhibited extensive cracking [94]. The SEM micrographs in Figure 7.2 show the evolution of microstructure in a 75 nm np-Au film during repeated thermal cycling and annealing steps. This film had been dealloyed in 70% HNO_3 for 10 min. As seen in Figures 7.2a-c, no cracks were observed at any location in the film samples. After the 100˚C thermal cycle (Figure 7.2b), the ligament structure appears to be more sharply defined, but the measured ligament width is the same as in the as-dealloyed condition (Figure 7.2a). Following thermal cycling to 200˚C (Figure 7.2c), the ligaments and pits are much coarser, but the film retains a continuous nanoporous structure. However, annealing at 300˚C (Figure 7.2d) or higher temperatures caused the np-Au films to densify and apparently collapse onto the substrate. Annealing can thus be utilized to tailor the porosity and ligament size of nanoporous materials, as was also shown for bulk np-Au [63]. The underlying cause of ligament coarsening in np-Au during annealing and/or dealloying is believed to be Ostwald ripening [60, 63, 95]. Other researchers have not reported densification of np-Au such as that in Figure 7.2d. This may be due to the stress state during annealing of these thin films, which was compressive above 225˚C (see below).

Table 7.2 lists the average ligament width for a 75 nm np-Au film as a function of annealing temperature, based on measurements of SEM and TEM micrographs. Both types of images yielded consistent results for average ligament width at each thermal cycling stage. Ligament width remained nearly constant during thermal cycling to 100˚C, but increased from ~15 nm to ~30 nm during cycling to 200˚C. Above 200˚C, ligaments coarsened significantly, eliminating most of the porosity (see Figure 7.2d). Average grain size in this as-deposited film was ~45 nm. After dealloying, no grain boundaries were discernible, possibly because grain size is only twice the cell size (ligament plus pore diameter). The porous network thus masks any original grain structure.

Table 7.2 Ligament width for a 75 nm np-Au film after various thermal cycles. Compared to the as-dealloyed state, ligament width remained nearly constant after 100˚C annealing, doubled after 200˚C annealing and increased to 62 nm during 300˚C or higher temperature annealing. Each value below is an average of 350 to 500 ligament measurements.

Film Condition	Ligament width (nm)	
	From SEM images	From TEM images
As-dealloyed	12	15
Annealed at 100˚C	14	16
Annealed at 200˚C	30	29
Annealed at 300, 400 or 500˚C	62	-

It has been proposed that np-Au ligaments are themselves nanocrystalline, i.e. that each ligament contains multiple grains, which could influence the mechanical properties of np-Au and may cause the high strength levels determined for this material [60, 96]. Biener and Hodge reported that bulk np-Au (made by dealloying $Au_{0.42}Ag_{0.58}$) exhibited polycrystalline ligaments with grain size ~10-60 nm [61] and presented TEM micrographs that showed nanocrystallinity within Au ligaments [70]. However, Ding et al. studied free-standing nanoporous Au leaf (100 nm thick) that had been dealloyed by free corrosion and retained the grain structure of the precursor alloy, exhibiting single crystalline ligaments [89]. In the current study, np-Au ligaments with widths ~10-30 nm were observed to be single crystalline, and poly- or nanocrystalline ligaments were seen only in a sample subjected to extended dealloying.

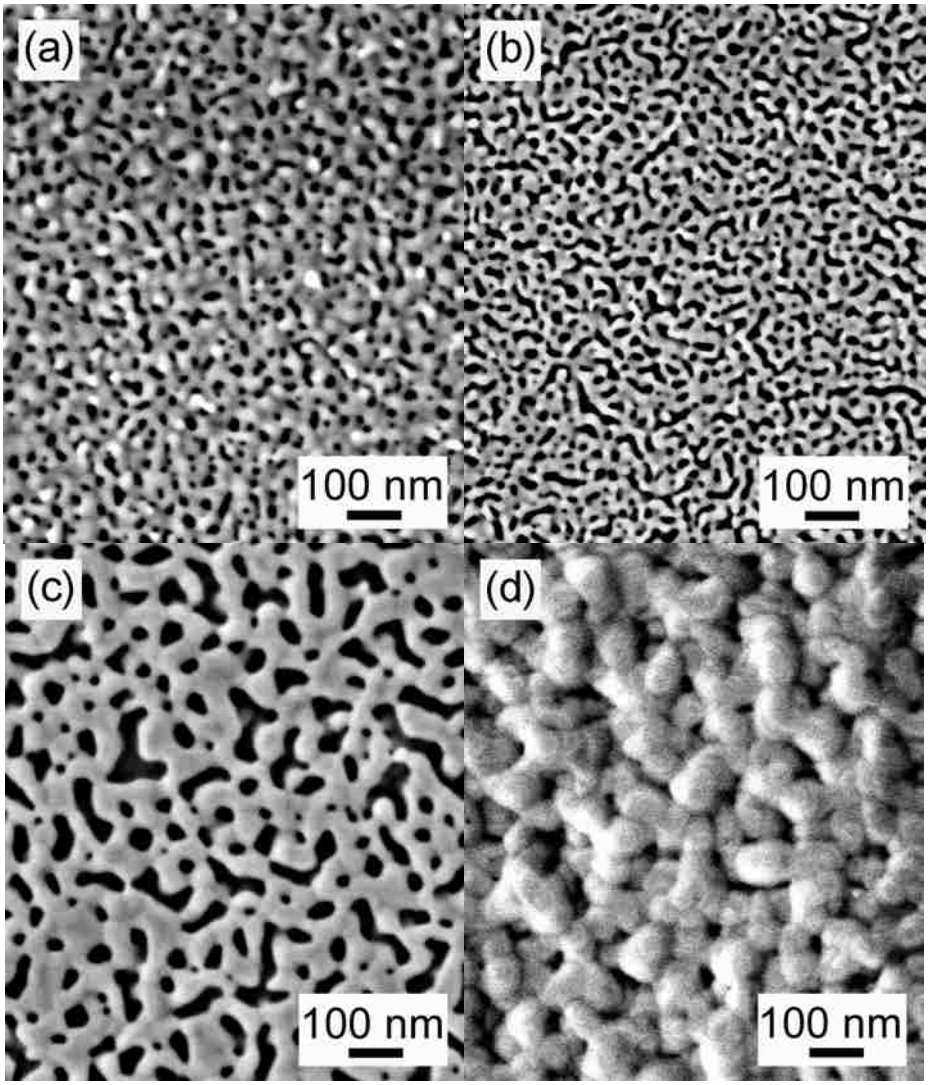

Figure 7.2 SEM micrographs showing structural evolution during thermal cycling of a 75 nm film. (a) As-dealloyed np-Au. (b) After thermal cycling to 100˚C. (c) After thermal cycling to 200˚C. (d) After thermal cycling to 300˚C, the nanoporous structure has densified and the open space between ligaments is significantly reduced. There is negligible ligament growth after 100°C compared with as-dealloyed state.

Figure 7.3 presents TEM micrographs of 75 nm np-Au films before and after thermal cycling to 200˚C. As was seen with SEM (Figure 7.2), ligaments coarsened during thermal cycling but no cracking occurred at grain boundaries (GBs) or elsewhere. The difference between these crack-free films and previously tested films that exhibited

extensive cracking [94] is higher Au content in the precursor alloy films used here. Although GBs are visible in Figure 7.3b, they exist in only a small number of ligaments, while the majority of ligaments are single crystalline. GBs cause some constriction of host ligaments, but do not act as failure initiation sites. The GBs in Figure 7.3b suggest a grain size ~200 nm (4-5 times the as-sputtered grain size). This may be due to specimen annealing, which caused ligament coarsening and, presumably, GB movement, possibly with consumption of small grains.

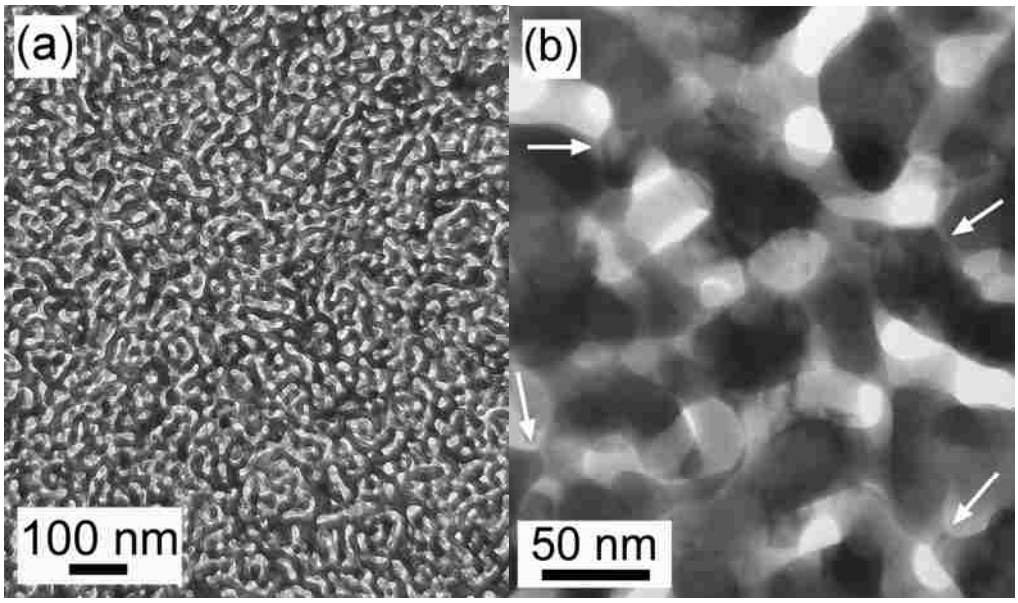

Figure 7.3 TEM micrographs showing nanoporous film structure. (a) 75 nm np-Au in the as-dealloyed state (10 min in 70% HNO_3), and (b) after thermal cycling to 200˚C. White arrows indicate grain boundaries.

Figure 7.4 is a TEM micrograph of a 45 nm np-Au film that was dealloyed for 35 min. The nanoporous structure exists as only a single layer (as opposed to the overlapping ligament layers seen in Figures 7.3a-b), and the ligaments are much coarser than in as-dealloyed 75 nm films (Figures 7.2a and 7.3a). Note that grain size and ligament width in the 45 nm film (Figure 7.4) are roughly the same as film thickness. In fact, the ligament structure appears to have collapsed onto the substrate, since the net thickness of Au in the alloy film was only 14 nm but the ligament widths in Figure 7.4 are 30-60 nm. Np-Au films can thus be tailored to form nanoporous structures consisting

of multiple layers (Figure 7.3b) or a monolayer (Figure 7.4) by varying the alloy film thickness and dealloying time.

The nanoporous structure appears to be unstable below a certain thickness, somewhere between 45 and 75 nm, at least during the 35 min dealloying time used for the 45 nm film. This may be due to the limited number of ligaments that can exist through the film thickness. Cell size (ligament width plus pore diameter) is typically ~25 nm after 10 min dealloying, implying that a 45 nm film could have 1-2 layers of ligaments. However, this may present an unstable situation where the nanoporous structure undergoes additional coarsening and forms a single layer of thicker/wider ligaments. A possible stability criterion for np-Au films with multiple layers of ligaments is that the pure Au thickness in the alloy should be larger than the ligament diameter after dealloying.

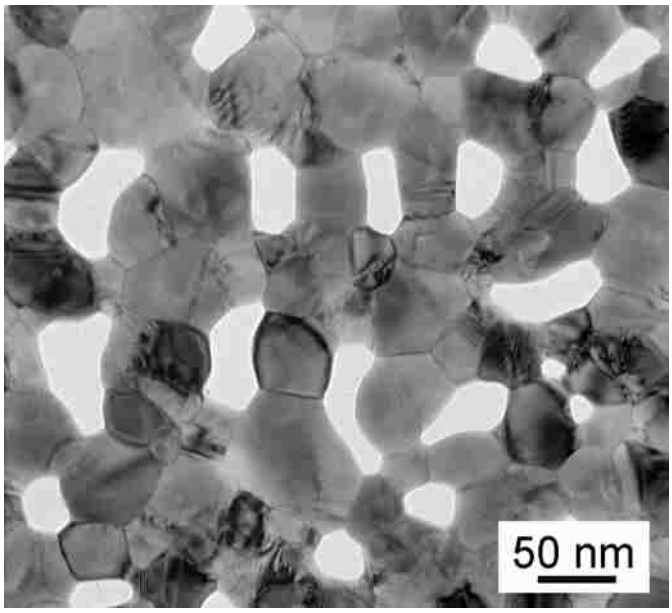

Figure 7.4 TEM micrograph of a 45 nm np-Au film dealloyed 35 min. Grain boundaries are conspicuous and ligaments are seen to be polycrystalline, although this is likely due to extensive coarsening and collapse of the nanoporous structure.

Table 7.3 lists alloy film stress prior to dealloying, as well as np-Au film stress measured immediately after dealloying and thermal cycling. Regardless of whether the initial alloy stress is compressive or tensile, the dealloying process leads to a high tensile film stress, although the reason is not yet fully understood [66]. It is likely due to the significant volume contraction that tends to occur during dealloying [53] and the lateral constraint imposed by the Si substrate that prevents in-plane contraction. It was hoped that an initially compressive stress in the alloy would avoid the generation of high tensile stresses during dealloying and thereby prevent film cracking. As seen in Table 7.3, high tensile stresses were not avoided, but these stresses did not cause cracking.

Table 7.3 Biaxial stress states of two 75 nm np-Au films with different initial stresses. All stress values are averages from 3D stress maps obtained at room temperature. Note that post-dealloying film stresses are calculated based on total thickness of the alloy film, and thus incorporate both ligaments and pores.

Film condition	Average biaxial stress (MPa)	
	Sample 1	Sample 2
Au-Ag alloy (before dealloying)	45	-65
As-dealloyed (10 min)	91	89
After 100˚C thermal cycle	61	-
After 200˚C thermal cycle	77	-

Figure 7.5 shows the evolution of film stress with temperature for another 75 nm np-Au film cycled to 100˚C and 200˚C. Stress at the end of both thermal cycles is ~83 MPa, very close to the 90 MPa stress measured after dealloying. The roughly linear trend in stress-temperature behavior suggests that the film experiences thermoelastic deformation up to 200˚C and that the Au ligaments never reach their yield point. Although it is difficult to identify the onset of a plastic regime in Figure 7.5, these curves for np-Au follow the same trends exhibited by fully dense metal films, i.e. biaxial stress becomes less tensile during heating and increases during cooling, due to differences in thermal expansion of the film and substrate. The densification of nanoporous films

observed after cycling to 300˚C (Figure 7.2d) may be due to compressive film stress which, as seen by extrapolation of the curves in Figure 7.5, exists above ~225˚C.

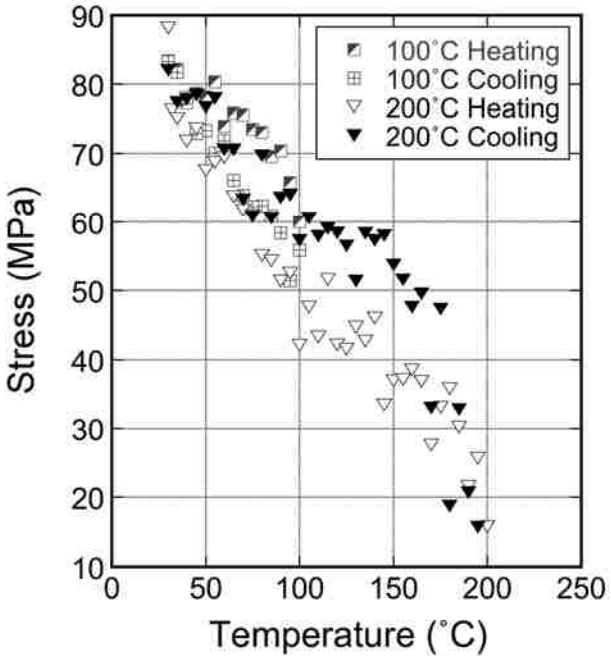

Figure 7.5 Biaxial stress of a 75 nm np-Au film on Si during thermal cycling to 100˚C and 200˚C. Deformation appears to be thermoelastic.

7.3.3 Morphology and stress evolution of 30 at.% np-Au films during dealloying

Figure 7.6 shows the evolution of nanoporous structure of a 300 nm thick np-Au film during various stages of dealloying. The average grain size of this 300 nm as-sputtered Au-Ag film is about 50 nm (Figure 7.6a). After a very short dealloying time of 5 seconds, numerous prominent pits formed at the center of grains, while some relatively smaller pits formed at grain boundaries or nearby. This observation contradicts the former hypothesis that dealloying occurs preferentially at grain boundaries. Instead, dissolution of Ag atoms occurred not only at grain boundaries, which exhibited some smaller pits, but most noticeably at the centers of grains with only a single prominent pore at each grain center (Figure 7.6b). After longer dealloying times of 15 or 30 seconds, in addition to an increase in quantity of prominent pits at grain centers, there was a noticeable increase in the diameter as well as quantity of the relatively smaller pits located near the grain boundaries (Figure 7.6c and d). After 1 min dealloying (Figure

7.6e), the number of smaller pits increased significantly and these smaller pits began to coalesce after 2 min (Figure 7.6f), resulting in the formation of larger channels between Au islands or ligaments. It was also observed that the size of prominent pits in the central regions of grains remained almost constant until dealloying was complete (Figure 7.6b-f). From 2 to 10 min dealloying, ligaments continued coalescing and coarsening, resulting in a more open nanoporous structure (Figure 7.6g-h).

Numerous prominent pits formed at the centers of grains. Dissolution of Ag atoms occurred not preferentially at grain boundaries, but instead it started at the centers of grains. This is suggested by an observation that the sizes of pits at centers of grains are much bigger at the initial stages of dealloying. The microstructure of a similar sample at shorter dealloying times was observed in an attampt to determine the locations where dealloying initiates. However, the morphology of a sample dealloyed for 2 seconds was found to be similar to that of sample that dealloyed for 5 seconds. It was difficult to obtain samples dealloyed less than 2 seconds. Diluted electrolyte may help increase the window of time for investigating the evolution of nanoporous structure, and further studies will therefore be performed.

The observation that there are many smaller pits around grain boundary region was consistent with Forty's results [18]: the concentration of Ag is relatively high in grain boundary regions, so chemical activity is more prominent there, which should cause more Au transport and therefore a greater density of nucleated island. Thus, the pits are more numerous but smaller in size with grain boundary regions. This could be a plausible hypothesis, were it not for the observation that single, larger pits exist in central regions of the grains. The existence of two length scales (see especially Figure 7.6e) suggests that the formation of these pits could be due to different mechanism.

Erlebacher's model of dealloying proposed a length scale λ, which is twice the mean distance a more noble atom may travel [5, 17]. This length scale is the average distance between the central, interior lines of neighboring ligaments for a well-developed nanoporous structure. During the incipient stages of porosity formation, the length scale λ corresponds to the distance between Au-rich islands or hills. According to the model, this length scale should be uniform throughout an entire specimen. If a Au enriched hill developed with a distance less than λ, this hill would eventually diminish because of

surface diffusion of Au atoms to nearby hills within a distance λ. However, this model cannot explain the presence of bimodal length scales.

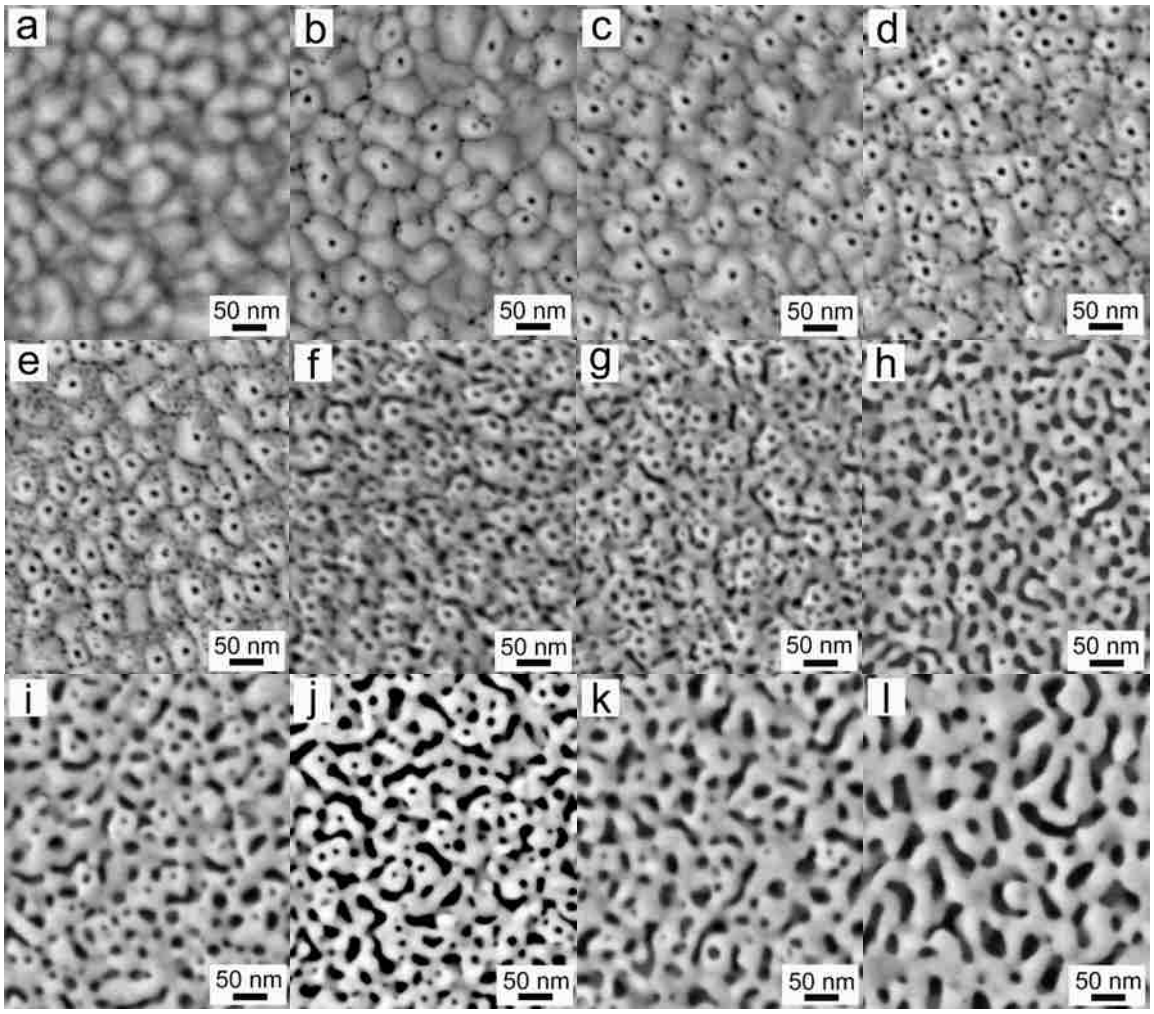

Figure 7.6 Evolution of nanoporous structure during dealloying, including early stages from Au-Ag film. Dealloying time: (a) 0; (b) 5 s; (c) 15s; (d); 30s; (e) 1 min; (f) 2 min; (g) 5 min; (h) 10 min; (i) 20 min; (j) 30 min; (k) 60 /Cite></EndNote>¶ [8]

Forty proposed a model that the widths of pits were caused by disordering and reordering of Au and Ag atoms on surfaces [19]. According to Forty's model, pitting is a result of the growth and coalescence of Au islands. However, in the current work, pits formed prior to Au islands. More importantly, Forty's model predicted shrinkage in the width of pits, which was not observed here. The observed phenomenon that bigger pits

form at centers of grains, immediately followed by smaller pits forming along grain boundaries, cannot be explained by Erlebacher's or Forty's models.

It was noticed that the size of pits formed in the centers of grains remained almost constant during 5 s to 2 min dealloying. This suggested that there exists an average maximal diffusion length that Au atoms can diffuse; otherwise the size of holes in the center of grains should become larger and larger. Average grain size was measured to be ~50 nm and average diameter of bigger pits at grain centers was ~9 nm at 1 min dealloying. We deduced that the length scale λ is half of the grain size. Ag atoms within the distance of λ from grain centers will diffuse towards grain centers and agglomerate into Ag clusters, while Au atoms, at the same time, diffuse in opposite directions and form a Au island. Figure 7.7 shows a schematic of phase separation of the Au-Ag alloy within a grain. Smaller pits formed along grain boundaries, separated by an average distance less than λ, and then coalesced after longer dealloying times resulting in an increase of length scale. This suggests that bulk diffusion outside an area with diameter λ may be much slower than in the central region. Surface diffusion, upon exposure to HNO_3, may be the dominant reordering mechanism in these grain boundary neighborhoods, so these samller pits with shorter length scale could be explained by Erlebacher's model.

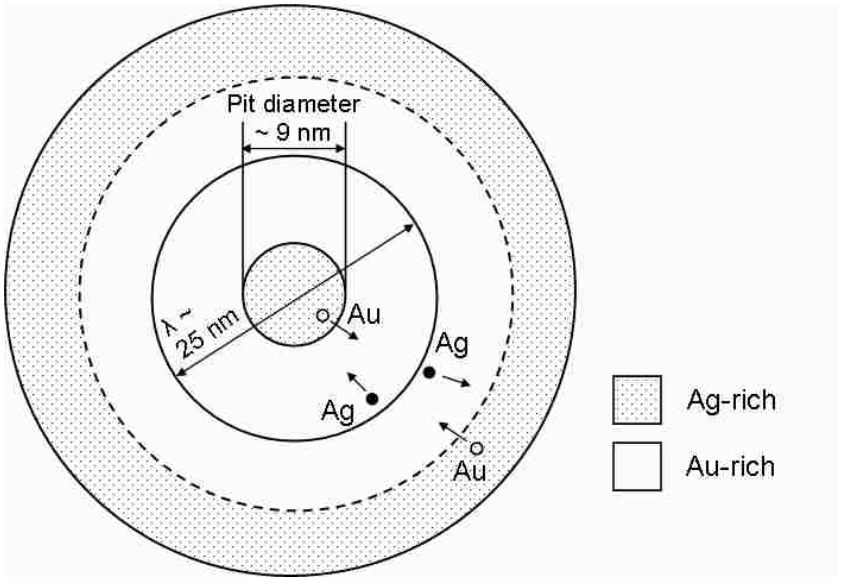

Figure 7.7 Schematic of bulk diffusion of Au and Ag atoms in an alloy grain.

This length scale was taken as the distance between central axes of ligaments and was retained when porosity became well-developed (Figure 7.6f-g). The cell size (diameter of a pit plus the diameter of a surrounding Au island, indicated by the dashed circle in Figure 7.7) of these bigger pits at grain centers would be larger than the length scale λ.

Figure 7.8a presents a plot of ligament width versus dealloying time. The plot shows that ligaments do not begin coarsening significantly until 5 min dealloying. The data was also plotted on a logarithmic scale, as shown in Figure 7.8b. By fitting the last four data points in the log-log plot, a relationship of $w \propto t^{0.24}$ between the ligament width w and dealloying time t is obtained.

The coarsening of ligaments after 5 min dealloying exhibited a dependence of $t^{0.24}$, in agreement with the literature for pore size coarsening of np-Au during electrochemical dealloying [97]. According to Dursun et al. [97], ligament coarsening is related to the surface diffusivity of Au atoms in electrolytes. The $t^{0.24}$ dependence of ligament width on dealloying time for the 30 at.% Au 300 nm film is quite different from the former result (for 25 at.% Au thin films), where ligament width increase as $t^{0.13}$. The discrepancy can be attributed to factors that affect the surface diffusivity of Au atoms in electrolytes. Comparing the two alloy types, the primary difference is the Au content in the starting alloys. Variation of the ratio of Au to Ag may affect the surface diffusivity of Au in HNO_3, which is a complicated process. Changing the starting composition of the precursor alloy will have an effect on vacancy density resulting from dissolution of Ag atoms, as well as the Au adatom density in HNO_3, which will ultimately affect the diffusion of Au atoms.

More importantly, residual stress is different in these two kinds of np-Au films and is another factor that can influence diffusion. Gorskii et al. [98] found that the diffusion rate of Au and Ag was considerably reduced when hydrostatic pressure was applied. Balluffi et al. [91] analyzed stress-induced diffusional transport. According to these authors, the applied stress alters the diffusion potentials at various sources and sinks atoms in the material. For example, if a polycrystalline wire specimen is subjected to a tensile force, the diffusion potential of grain boundaries will decrease because of the

presence of a normal tensile stress at boundaries, while the diffusion potential on the cylindrical specimen surface remains the same, since no normal stress acts there. The difference in diffusion potential between grain boundaries and surfaces will cause transport of atoms from grain surfaces to grain boundaries. This will result in elongation of the wire in response to the applied stress. The 30 at.% Au np-Au specimens carry residual biaxial stresses. In addition, ligaments of np-Au are never straight and are random in direction, so an applied force can always be decomposed into components parallel and perpendicular to the ligaments. According to Balluffi's study, diffusion along both parallel and perpendicular ligament axes will be increased. Thus, ligament coarsening (both along the length and width) of 30 at.% Au np-Au is more rapid than 25% at.% Au np-Au, which carries almost no stress. However, the interpretation above gives only a qualitative explanation as to why np-Au coarsens differently under stress. Further study is needed to quantitatively study the coarsening behavior of ligaments.

Figure 7.9 shows the stress evolution of np-Au films with different thickness during dealloying. Stresses in all films showed the same trend: stress increases during the initial period of dealloying and then decreases with extended dealloying after some peak value. Considering the early stages of dealloying in more detail (Figure 7.9b), it can be seen that the stresses in 75 nm, 150 nm and 300 nm films reached their peak values at 0.5 min, 1 min and 2 min. After reaching their peak values, stresses decreased rapidly. After 100 min dealloying, stresses approached a plateau of ~40 MPa.

Stress in np-Au films during dealloying was controlled by two concomitant and interactive processes: Ag dissolution and Au ligament coarsening. It is known that dealloying induces internal tensile stress in np-Au [58, 66], which is consistent with our results: tensile stress developed immediately after dealloying. Observation from Figure 7.6 shows that at 2 min dealloying time, Ag dissolution from the 300 nm film is almost complete and that ligament coarsening begins thereafter. The stress in the 300 nm film during dealloying reached its peak value at 2 min (Figure 7.9b). Combined with Figure 7.6 and 7.9, it is clear that the dissolution of Ag atoms caused the increase of stress in the initial stage of dealloying (Figure 7.9), while Au atom rearrangement and np-Au ligament coarsening is responsible for the stress decrease (Figure 7.9). The thinner the film, the shorter the time needed for the completion of Ag dissolution.

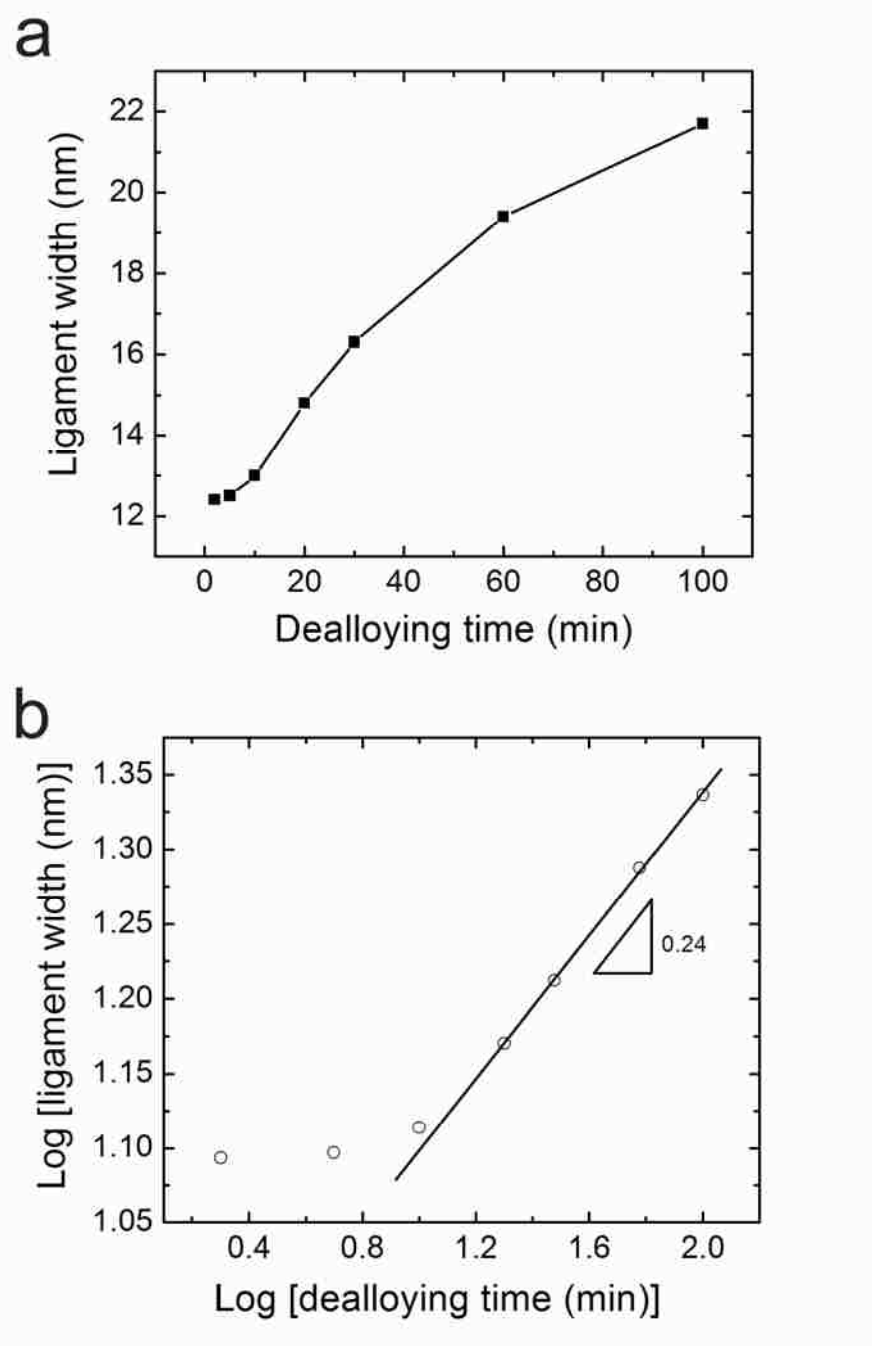

Figure 7.8 Evolution of ligament width in a 300 nm np-Au film during dealloying from 2 min to 100 min. (a) Ligament width versus dealloying time. Ligament width increased considerably after 5 min dealloying. (b) By fitting the data after 20 min dealloying on log-log scale, a power law of $t^{0.24}$ obtained.

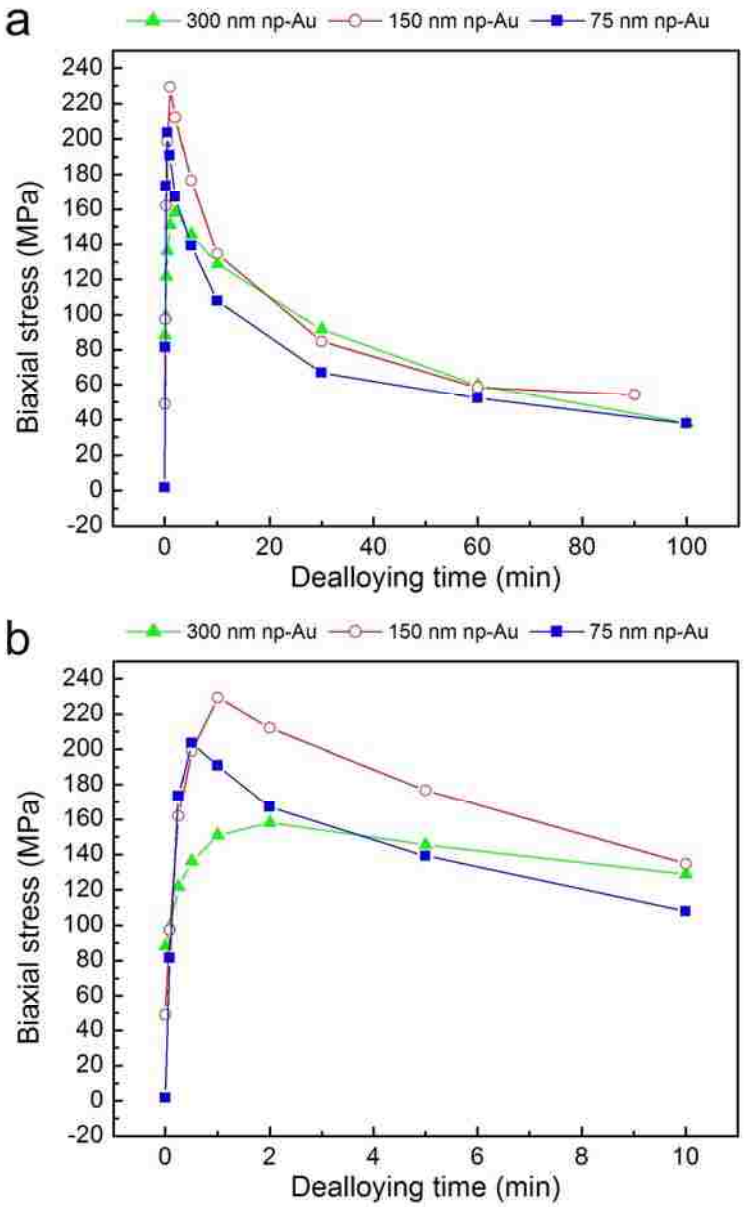

Figure 7.9 Stress evolution of np-Au thin films with dealloying time. Stresses increase during the initial stage of dealloying, reach their peak values, and then decrease with longer dealloying time.

Figure 7.10 shows the change in Ag content of a 300 nm np-Au film dealloyed by free corrosion. Ag content after electrochemical dealloying, as well as combined free corrosion and electrochemical dealloying, are also plotted in figure 7.10. For free

corrosion, Ag content decreases rapidly in the early stage of dealloying (within the first 5 min) and then declines continuously before reaching a plateau of ~13 at.% after 100 min dealloying. Apparently, free corrosion is not an effective method for removing residual Ag rapidly to a sufficiently low level (e.g. <10 at.%). For comparison, the sample was also dealloyed electrochemically for 30 min using a galvanostatic cell with applied potential $U = 0.33$ V and measured current $I = 1$ mA. The resulting residual Ag content of 8.2 at.% (solid circle) was much lower than the 23.2 at.% Ag obtained after 30 min free corrosion. However, while the electrochemical method expedites Ag dissolution, it causes cracking, which usually happens when the dealloying rate is too high.

Figure 7.11a shows cracking in a plan view SEM image of the film that was electrochemically dealloyed for 30 min. Inspired by our former work on bulk np-Au [57], a two-step dealloying method was used on the same film with the intent of avoiding cracking. Free corrosion for 20 min was followed by electrochemical dealloying for 10 min. The residual Ag content after two-step dealloying film was 10.1 at%, which is shown as the open square in figure 7.10. This two-step dealloying approach avoids cracking of the film and facilitates the dissolution of residual Ag content compared with free corrosion over the same amount of time. SEM image of the two-step dealloyed film is shown in figure 7.11b. The porous structure was formed, but no cracking was observed throughout the sample.

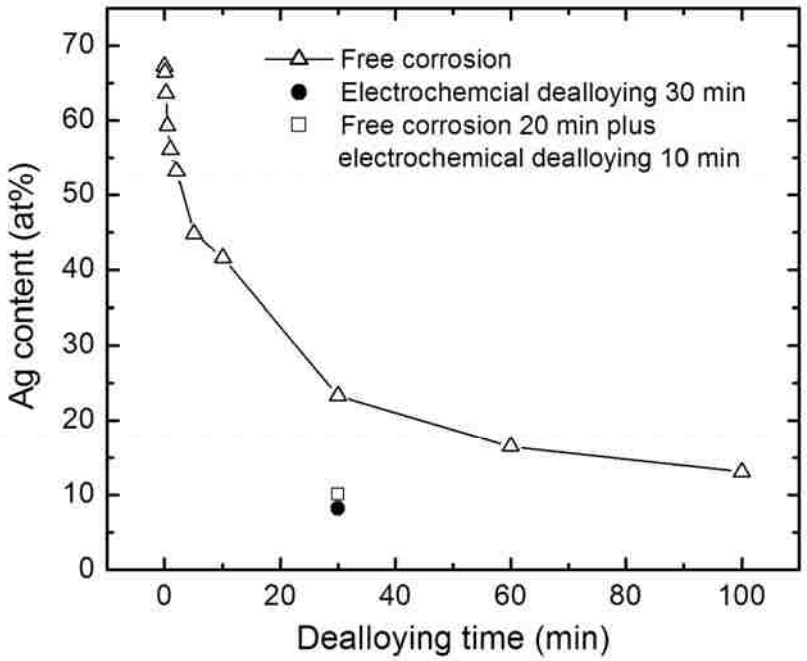

Figure 7.10 Evolution of Ag content in a 300 nm np-Au film during free corrosion, as measured by EDS (open triangles). For comparison, Ag content of a film that was electrochemically dealloyed for 30 min (solid circle) and a sample subjected to combined free corrosion for 20 min and then electrochemical dealloying for 10 min (open square) were also plotted.

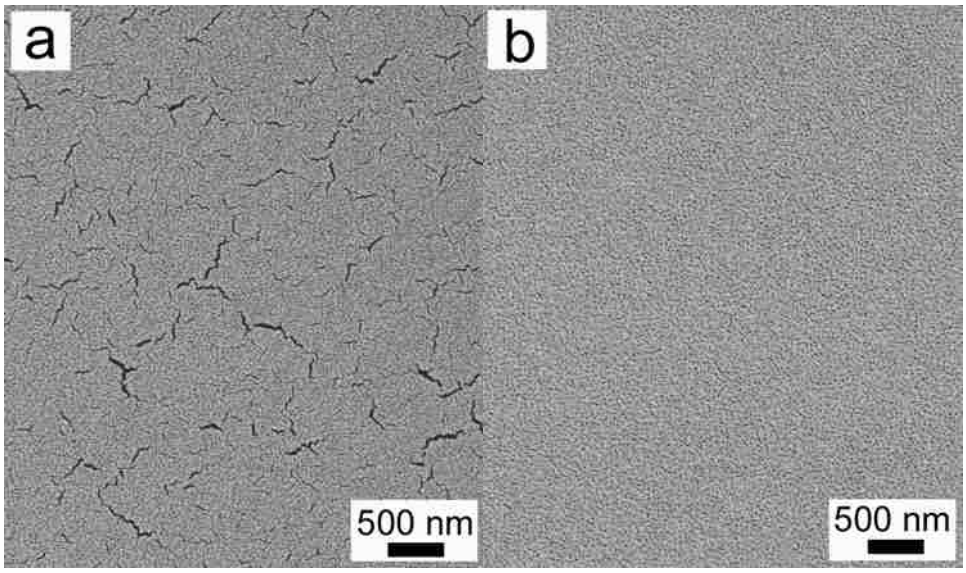

Figure 7.11 Effect of dealloying conditions on residual Ag content and microstructure of 300 nm np-Au films. For electrochemical dealloying, the applied voltage was 0.33 V. Plan-view SEM images of the 300 nm np-Au film dealloyed under different conditions (a) Electrochemical dealloying for 30 min. (b) Free corrosion for 20 min plus electrochemical dealloying for 10 min, which resulted in a crack-free nanoporous structure.

7.4 Summary

The biaxial stress of np-Au films during thermal cycling exhibited a dependence on film thickness, with thinner films carrying higher stresses that appear to be thermoelastic and thus set a lower limit on the yield strength of np-Au. Based on these stresses and correcting for the volume contraction that occurs during dealloying, the equivalent bulk yield strength of Au ligaments was calculated to be at least 2.0 GPa for a 75 nm np-Au film. This corresponds to a resolved shear stress $\approx\mu/49$, close to the theoretical shear strength of bulk Au. Interestingly, this demonstrates that these nanoporous materials can support stress levels that approach the theoretical shear strength while simultaneously exhibiting dislocation activity.

Completely crack-free np-Au thin films on Si substrates have been processed by dealloying and thermal cycling. Ligament width of np-Au films remains constant during cycling to 100˚C, but doubles during cycling to 200˚C. Cycling to higher temperatures causes significant ligament coarsening and densification of the porous structure. The thinner films studied here also underwent coarsening and collapse of the nanoporous structure, and it is postulated that total Au thickness must exceed the typical ligament diameter (12-15 nm) achieved during dealloying. Dealloying generates high tensile stresses in thin film np-Au, regardless of whether the film is initially under tension or compression.

After very short exposure of 30 at.% np-Au films to HNO_3, dealloying did not occur preferentially at grain boundaries, but instead was most prominent in central regions of grains. This may be due to aggregation of Ag at grain centers. There are two mechanisms that govern the stress change during dealloying: Ag dissolution leads to generation of tensile stress, while ligament coarsening relaxes this tensile stress. The thinner the film, the easier it is to remove or dissolve Ag atoms from it. Two-step dealloying combined with free corrosion and electrochemical dealloying produced films with no cracks and considerably lower residual Ag content. Ligament coarsening of 30 at.% np-Au films is time dependent and follows a power law of $t^{0.24}$, which is much faster than the time dependence of $t^{0.13}$ for 25 at.% films. Residual stress is thought to be responsible for the difference: the biaxial stress in 30 at.% Au films could facilitate diffusion of Au atoms along both parallel and perpendicular ligament axes, resulting in faster growth of ligament width as well as length.

Chapter 8

In situ nanoindentation of nanoporous Au thin film under TEM

This chapter is based on the following manuscripts:
Ye Sun, T. John Balk, *Mechanical Behavior and Microstructure of Nanoporous gold Films*, Mater. Res. Soc. Symp. Proc. 924 Z1.2.1-Z1.2.6 (2006), copyright of 2006 by Materials Research Society.

Ye Sun, Jia Ye, Zhiwei Shan, Andrew M. Minor, T. John Balk, *The Mechanical Behavior of Nanoporous gold Thin Films*, JOM **59**(9) 54-58 (2007), copyright of 2007 by Springer Science and Business Media.

Ye Sun, J. Ye, Andrew M. Minor and T. John Balk, *In-Situ Indentation of Nanoporous Thin Films,* Microscopy Research and Technique (2008) in press, copyright of 2008 by Wiley-Blackwell.

8.1 Introduction

Recent and ongoing studies have focused on nanoporous Au (np-Au) and other noble metals (e.g. np-Pt) to investigate their potential for applications such as catalysis and gas sensing [8, 37, 89, 99]. However, most of this work has focused on their electrochemical preparation or chemical properties [16, 86, 97, 100]. Recently, the surface functionalization of np-Au has been explored in the context of chemical sensing [101]. In addition to these important research areas, the mechanical properties of nanoporous metals have begun to attract increasing attention [61, 63, 70]. These studies suggest that np-Au may exhibit brittle fracture due to the characteristic length scales of pore size and sample dimension [63], and that theoretical shear strengths may be achieved by Au ligaments during nanoindentation testing [55, 61, 62].

More recently, Hodge et al. performed a systematic study involving nanoindentation of bulk np-Au, where the ligament size was varied by annealing [60].

They proposed a modified form of the Gibson-Ashby equation [52], introducing a Hall-Petch type factor that affected the strength of np-Au. Based on their findings, Hodge et al. set a threshold ligament size of 500 nm, above which the Hall-Petch term becomes negligible. The np-Au samples described in our paper were thin films with a maximum thickness of 300 nm and pore diameters of 10-20 nm, and our indentations were limited to ~100 nm in depth. Thus our studies probe the mechanical behavior at a much smaller length scale than previously reported in the literature.

While traditional nanoindentation testing has been performed on np-Au thin films [68], in situ nanoindentation in the transmission electron microscope (TEM) enables the possibility of real-time observation of deformation in np-Au ligaments and simultaneous measurement of load-displacement behavior [81, 102, 103]. With this technique, the nucleation and motion of dislocations can be observed while a load-displacement curve is simultaneously recorded, allowing direct correlation of measured mechanical behavior with microstructural changes. In this chapter, np-Au films of various thickness were tested by in situ nanoindentation. The motion of dislocations through np-Au ligaments and their interaction with each other was studied. Additionally, the effect of indenter displacement rate on the mechanical response of these np-Au films was investigated.

8.2 Experimental

When alloyed with a sacrificial metal such as Ag, noble metals such as Au can be subjected to a selective dissolution process known as dealloying that dissolves the Ag atoms, producing a nanoporous noble metal nanostructure via surface diffusion [50, 104]. The resultant structure consists of an interconnected network of ligaments and open porosity, with an extremely high surface-to-volume ratio. When Au-Ag alloys with approximately 20-40at% Au are immersed in HNO_3, Ag is selectively dissolved and np-Au with pore diameters and ligament sizes on the order of 10 nm or larger is formed [8, 105]. While most studies of np-Au have focused on bulk or free-standing thin film samples, it has been shown that blanket thin films of np-Au supported by Si substrates can be produced with uniform porosity and no cracking [72]. This form is most relevant to the current study, as it readily allows for the in situ nanoindentation of np-Au in the TEM.

Au-Ag alloy films with 25-30 at.% Au and thicknesses of 75, 150 and 300 nm were deposited onto substrates by co-sputtering from Au and Ag targets (ORION system, AJA International, base pressure ~10^{-6} Pa). Substrates included Kapton (HN 200, 50 μm thick, DuPont) and wedge-shaped Si, which were prepared using lithographic techniques [81]. Sputtering power and argon pressure were controlled during film deposition to produce films with a Au content of 25 or 30 at.%. For samples on silicon wedges, a 10 nm Ta interlayer and a 10 nm Au interlayer were sputtered before sputtering the Au-Ag alloy layer. This combination of interlayers produces excellent adhesion of the final np-Au film to the Si substrate. As-sputtered specimens were dealloyed by immersion in concentrated HNO_3 (70% stock concentration) for 30 minutes, followed by rinsing in ethanol and slow drying in air. Some specimens were annealed in air at 200˚C for 10 min, to coarsen the porous structure. For samples on Kapton, A 10 nm thick pure Au interlayer was deposited before Au-Ag films were sputtered onto substrates, in order to avoid films flaking off the substrates during dealloying. An *In situ* TEM sample was made from a specimen of np-Au on Kapton and the microstructure was investigated with a JEOL 2000 FX operated at 200 kV. In order to produce the *in situ* TEM sample, the backside of the Kapton substrate was mechanically dimpled and then chemically etched with a $KOH/H_2O/CH_3COOH$ mixture at 70 ºC.

In situ nanoindentation of dealloyed np-Au on Kapton and Si wedges was performed with a tensile holder in a JEOL 2000FX TEM and a Hysitron Picoindenter™ inside a JEOL 3010 TEM (operated at 300 kV). A Berkovich and a cube corner indenter with radius of curvature ~100 nm were used for indentation. All indentations were performed under displacement control and the indenter displacement rate was varied from 1 to 20 nm/s (constant for a given test).

Ligament size was measured from scanning electron micrographs of plan-view samples. Based on 350-500 measurements per film thickness, it was determined that the average ligament width was ~15 nm in all cases. Pore size could not be reliably measured from the micrographs, and instead was calculated from the ligament width and relative density. According to Gibson and Ashby's book on porous materials [52], the relative density (ratio of porous film density to the density of solid Au) is equal to $(d/l)^2$, where d is ligament width and l is cell size (ligament width plus pore diameter). For the as-

dealloyed np-Au films studied here, relative density was determined to be 36% and pore size ~10 nm.

8.3 Results and discussion

8.3.1 25 at.% Au nanoporous Au thin film

An *In situ* straining experiment in the TEM was performed on the np-Au/Kapton sample, yielding the micrographs shown in Figure 8.1. It is noted that there does not appear to be any grain boundary cracking. The cracking that did occur is oriented perpendicular to the loading axis and appears to be due to film stretching. Nonetheless, samples suggest ductile "bridging" behavior as seen in Figure 8.1b. As the film stretches and cracks, the np-Au film forms bridges that stretch across the crack, perpendicular to the "crack faces".

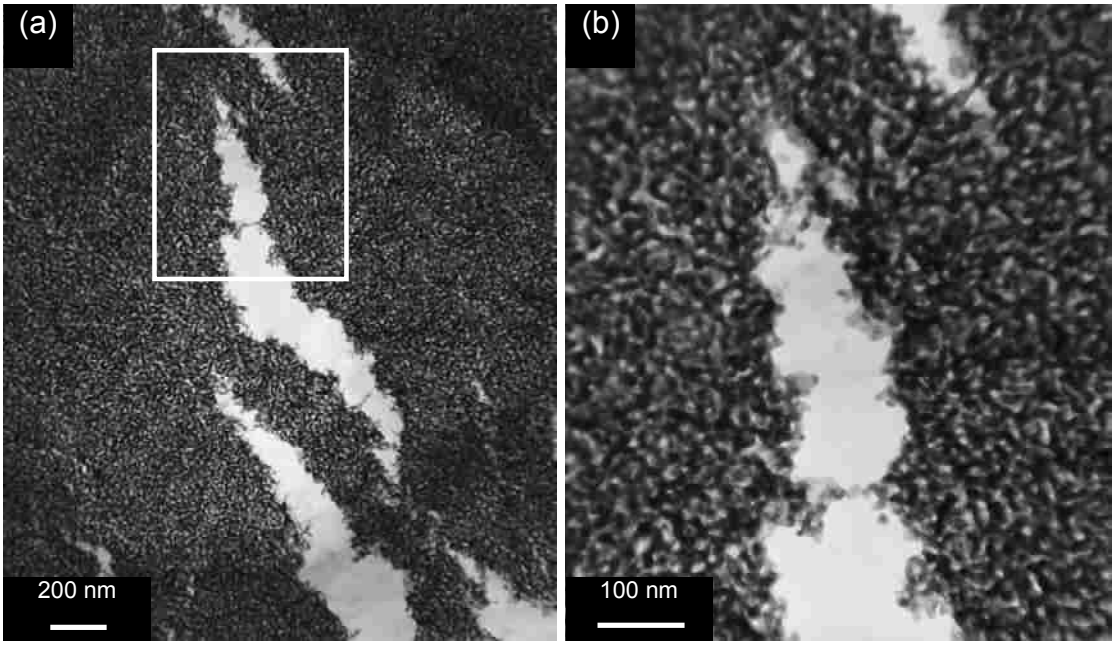

Figure 8.1 *In situ* TEM micrographs of a np-Au film on Kapton, dealloyed time for 5 minutes prior to this straining experiment. (a) Cracking of the np-Au film. (b) High magnification image showing ligaments bridging across the cracks.

8.3.2 30 at.% Au nanoporous Au thin film samples

Table 8.1 lists the average ligament width of np-Au films, after dealloying for 30 min, as a function of film thickness. This data was obtained from analysis of plan-view SEM images of np-Au films, such as that shown in Figure 1 above. The ligament width was the same for all np-Au films, indicating that the length scale of pores/ligaments is primarily dependent on dealloying time, while film thickness does not have a significant effect. However, as described below, film thickness does appear to influence the mechanical behavior of np-Au films as measured by thermal cycling.

Table 8.1 Ligament widths of np-Au films of various thickness. For each film, the ligament width data are based on the average of 350 to 500 measurements.

np-Au film thickness (nm)	Dealloying time (min)	Ligament width (nm)
300	30	15
150	30	13
75	30	14

Figure 8.2 presents TEM images of a 150 nm thick np-Au film before and after *in situ* nanoindentation. The film shown here is completely crack-free, which is quite unusual for np-Au samples in either bulk or supported thin film form. The width of ligaments in Figure 8.2a is 10-20 nm, which matches well with the results shown in Table 8.1. *In situ* nanoindentation of this 150 nm np-Au film was performed in displacement control mode. The diamond indenter used here had a Berkovich geometry, with a radius of curvature ≈100 nm. Figure 8.2b shows the indenter near the np-Au film, prior to indentation. Although the indenter vibrated during acquisition of Figures 8.2b-c, it was stable during the actual indentation experiment due to a damping effect upon contact. As shown in Figure 8.2c, the porous structure was compacted during indentation and became significantly denser, with a corresponding decrease in electron transparency.

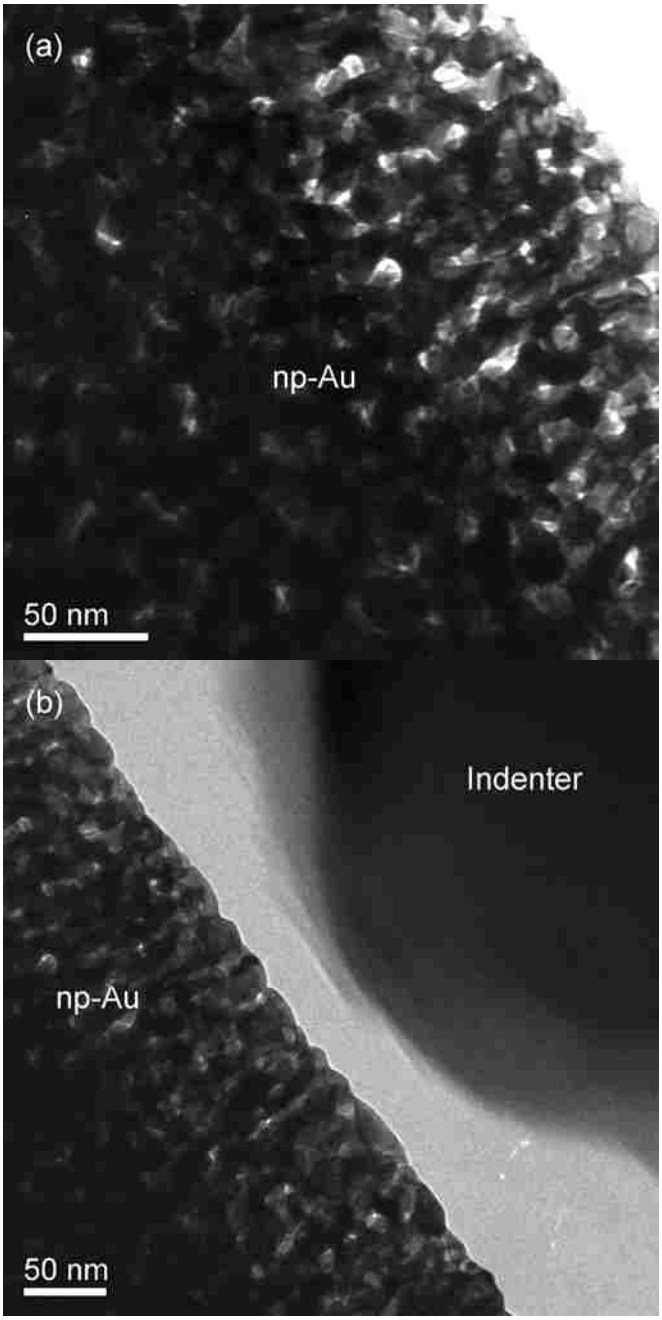
(a)
np-Au
50 nm
(b)
Indenter
np-Au
50 nm

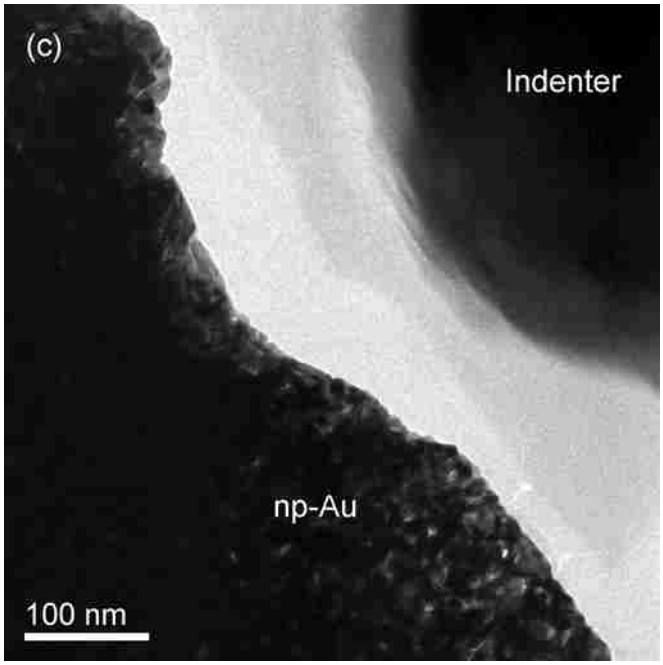

Figure 8.2 TEM images taken before and after *in situ* TEM nanoindentation of a 150 nm np-Au film on Si wedge, using a Berkovich diamond indenter. (a) As-dealloyed film with open porosity, (b) indenter moved into position near the np-Au film, and (c) densification of film after ligaments were compacted by the indenter. Despite the shaking apparent in (b) and (c), the indenter tip was steady during the actual indentation experiment. It can also be seen that the compacted np-Au region conformed to the diamond indenter and assumed the same shape.

Figure 8.3 presents the load-displacement curve corresponding to indentation of the 150 nm np-Au film portrayed in Figure 8.2. Two load-drops were observed in the loading curve and reveal an interesting aspect of deformation of np-Au during indentation. In the initial stages of nanoindentation, np-Au deformed easily and the displacement increased monotonically with increasing load. During this time, only the outermost layer of ligaments was compacted by the indenter, while the rest of the underlying structure remained undeformed. Upon further indentation, the "compaction front" of deformed np-Au moved into the film, ahead of the indenter, successively collapsing each neighboring layer of ligaments. It was also observed during *in situ* nanoindentation tests that, after initially smooth and easy compaction, expansion of the zone of deformed np-Au under the indenter was punctuated by short, collective jumps in the nanostructure. Comparison of the real-time load-displacement curve with the *in situ*

video indicates that these compaction bursts appear to correlate with the load drops, e.g. those observed in Figure 8.3. In this particular case, local maxima in the loading curve are marked by arrows at 70 and 81 nm indentation depth. The distance between load drops is approximately 11 nm, roughly the same as the pore size (9-10 nm) calculated from the measured ligament width and relative density according to the Gibson-Ashby equations [52]. Numerous other indentation tests exhibited similar load-drop intervals. This suggests that the load drops result from collective collapse of a layer of pores, i.e. that a broad array of ligaments/struts collapse simultaneously or in a chain reaction that causes a noticeable decrease in indenter load.

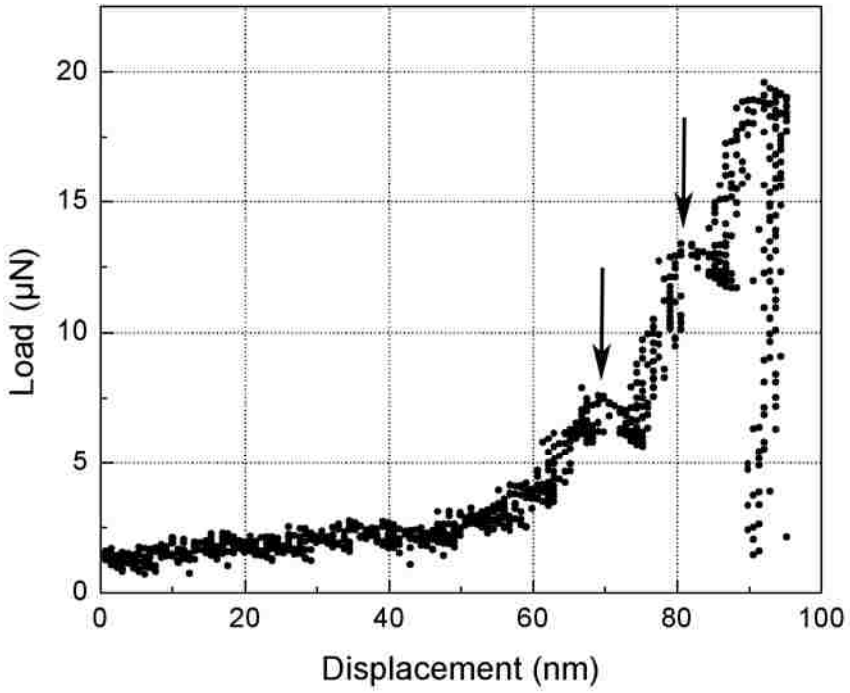

Figure 8.3 Load-displacement curve recorded during *in situ* TEM nanoindentation of a 150 nm np-Au film. This is the same indent that was shown in Figure 8.2. It appears that the load drops (marked by arrows) correspond to collective collapse of a layer of pores.

Figure 8.4 presents TEM images recorded during *in situ* nanoindentation of a 75 nm np-Au film using a cube corner indenter. For this test, indentation was performed "manually" (the indenter was moved forward in discrete steps until contact was made,

instead of programming a set displacement ramp and letting it run to completion). In this way, ligaments were compressed only slightly and deformation was kept to a minimum. Comparing Figures 8.4a-c, it can be seen that the two np-Au ligaments marked by arrows deform locally, while the remainder of the porous structure was not affected by this indentation. Upon contact, the ligament tips deformed easily and in a clearly ductile manner, as would be expected for Au. Although the global behavior of np-Au is often brittle and accompanied by extensive cracking, the deformation of individual ligaments is still ductile.

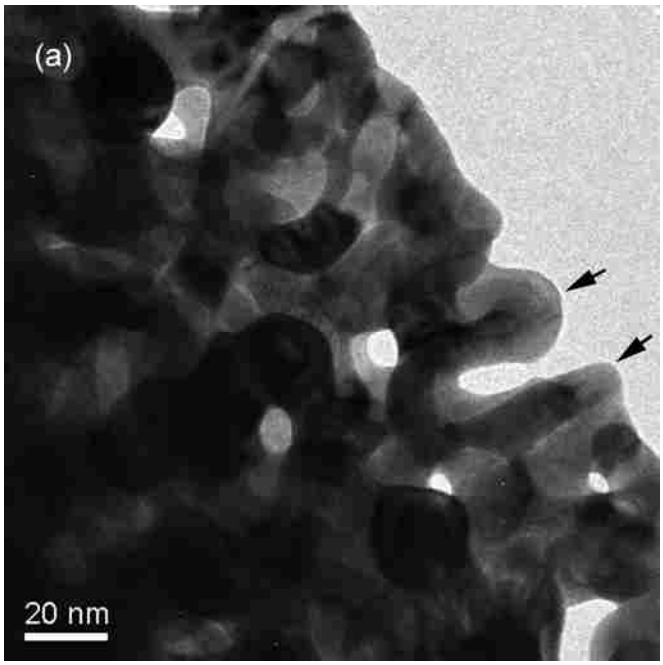

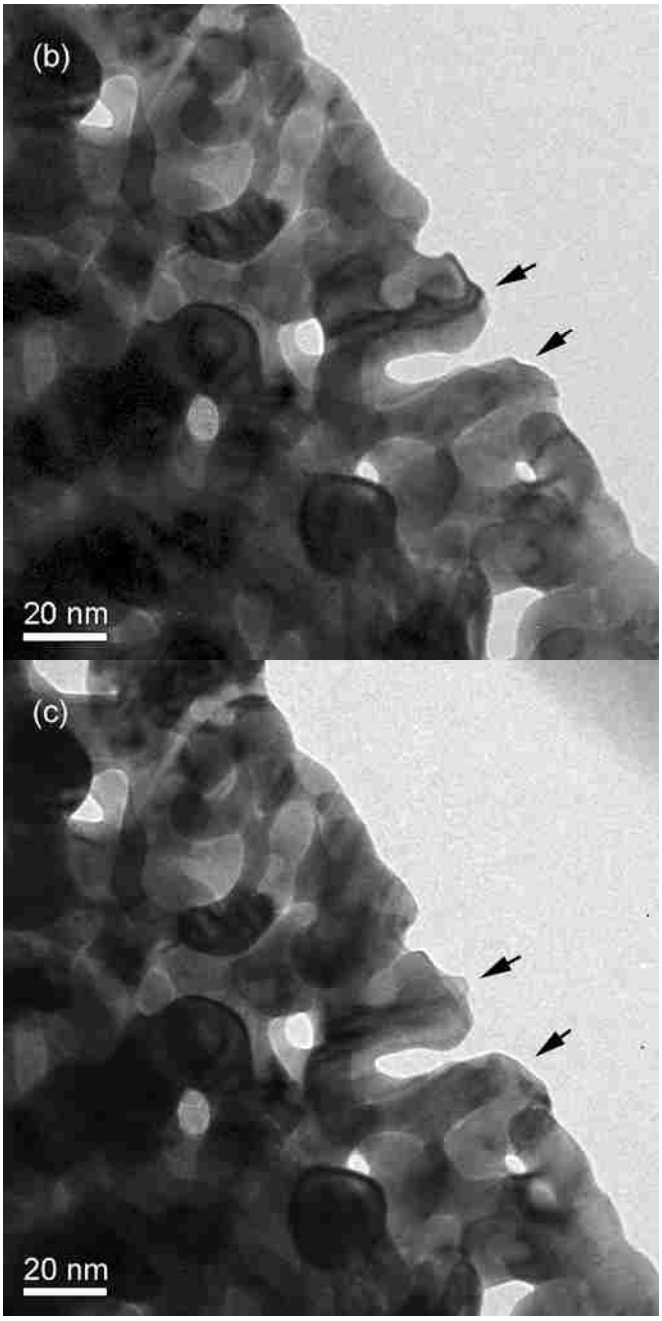

Figure 8.4 Still images recorded during a series of nanoindentation tests of a 75 nm np-Au film, where a cube corner indenter was used. Only two ligaments were compressed, and deformation was held to a minimum by manually moving the indenter in small steps. Ligaments contacted by the indenter are indicated by black arrows in (a) before indentation, and (b) after first indentation. Additionally, the ligaments were indented one more time, yielding a further shape change as shown in (c).

Figure 8.5 shows still images taken from *in situ* video observation of the 75 nm np-Au film during nanoindentation. The time interval between images is 0.6 seconds. In both images, the indenter is in contact with the outer layer of np-Au ligaments (the white contrast between the apparent indenter edge and the np-Au ligaments masks the actual edge of the indenter). The outermost layer of ligaments moved very slightly during continued motion of the indenter tip, accompanied by dislocations that were generated inside the ligament marked by a white arrow (compare Figures 8.5a and 8.5b). In Figure 8.5b, the dark lines corresponding to dislocations are seen to span the width of the ligament. Furthermore, the dislocations are straight, indicating that they do not experience a significant drag force from the surfaces of the ligament. In general, dislocations were observed to move easily within ligaments during deformation. Dislocations spanned the ligament width and underwent sequential glide to the ligament nodes, where they sometimes tangled with dislocations from other ligaments.

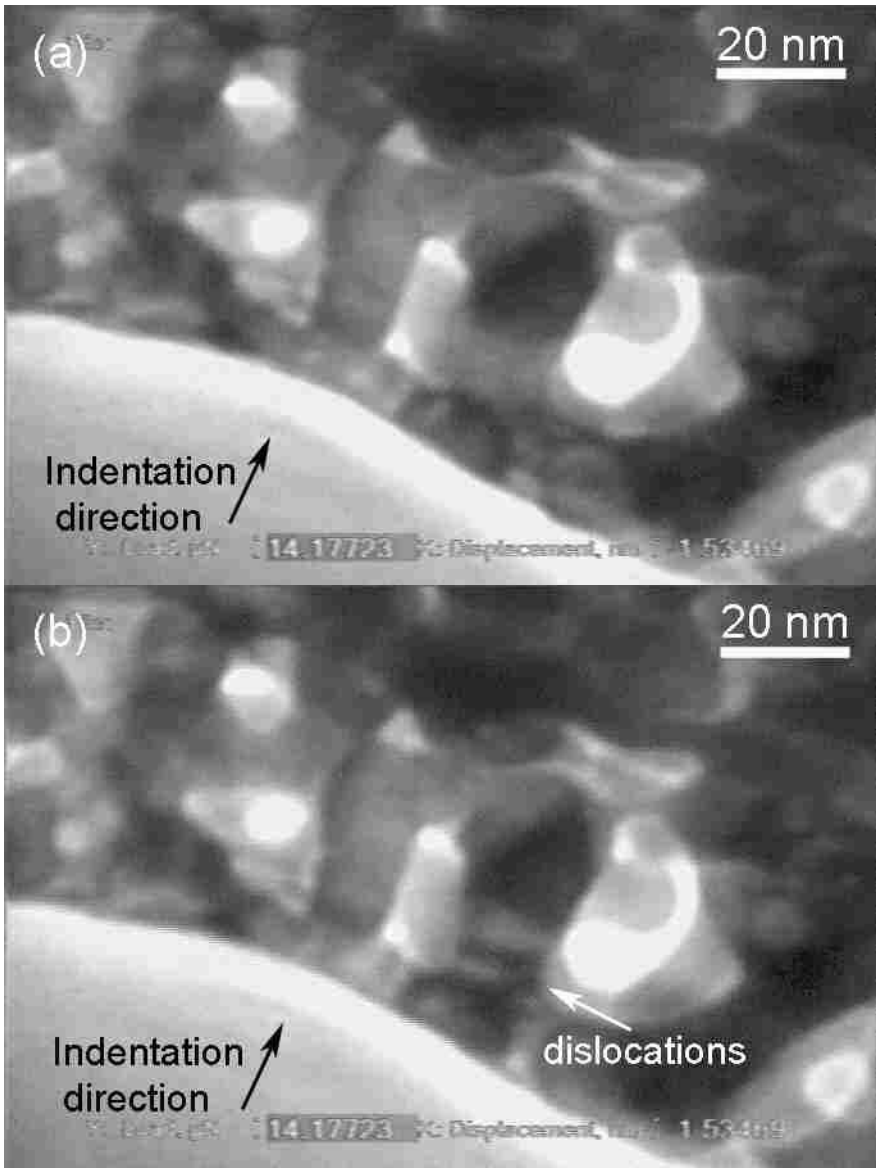

Figure 8.5 Still TEM images taken from an *in situ* movie recorded during indentation of a 75 nm np-Au film. Contact has already occurred in (a), as seen by the curved outermost layer of ligaments on the film surface. In image (b), taken 0.6 seconds later, dislocations can be seen moving upward, within the ligament marked by a white arrow. These dislocations were followed by others, and all moved toward the ligament node during continued indentation.

Thin films of np-Au consist of an open network of interconnected pores and ligaments. This is seen in Figure 8.6, where a 75 nm (nominal thickness) film is shown in the as-dealloyed and annealed states. Figure 8.6a reveals the numerous pores that exist in

the as-dealloyed film, which has an average pore size of ~10 nm and ligament width of ~15 nm. In the annealed state (Figure 8.6b), the np-Au film appears denser, yet still exhibits an open nanoporous structure. The denser appearance, however, is due to the wider ligaments and not to true densification of the np-Au. In both cases, the actual film thickness (measured from the Au interlayer to the average film surface) is ~65 nm. Dealloying thus caused a contraction of 13% in film thickness, consistent with other results for film-on-wedge samples [82]. Annealing caused the porous structure to coarsen (average pore size ~20 nm and ligament width ~30 nm) but did not lead to further densification or reductions in film thickness.

Still images from the indentation of a 75 nm np-Au film are presented in Figure 8.7. These images were obtained by averaging three successive frames from the *in situ* indentation movie, in order to average out background noise and improve the quality of these micrographs. Dislocations were nucleated under the indenter tip and moved easily along the axes of ligaments. An example is shown in Figure 8.7a, where three dislocations span the diameter of a ligament just beneath the center of the image. As indentation proceeded, these dislocations moved up and toward the node. After an elapsed time of 3.33 sec, Figure 8.7b shows that one dislocation has moved into the node, with the other two dislocations having moved only slightly. Further indentation caused these two dislocations to also move into the node.

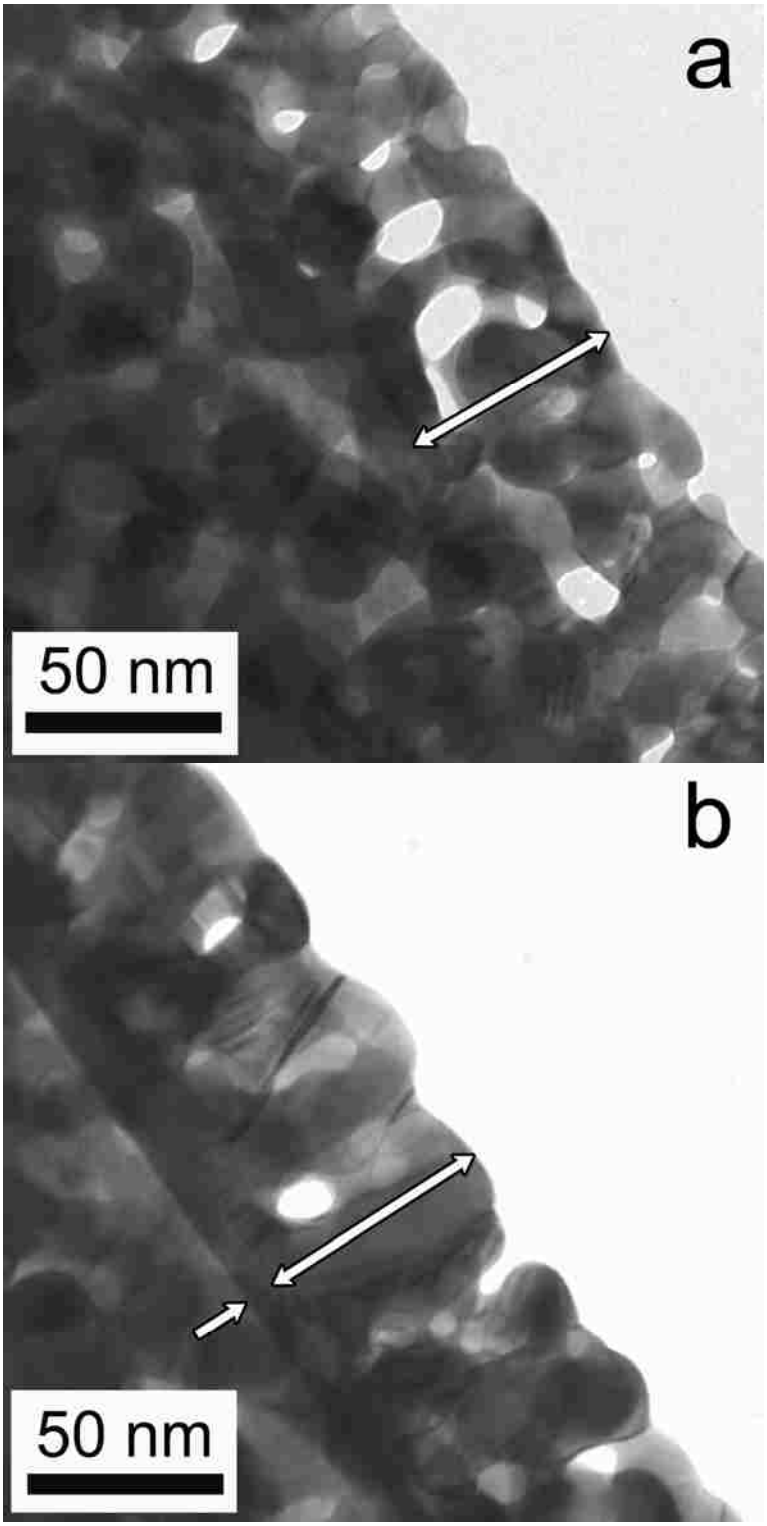

Figure 8.6 (a) As-dealloyed 75 nm np-Au film, showing an open nanoporous structure with interconnected ligaments. (b) After annealing at 200˚C, the 75 nm np-Au film exhibits thicker ligaments but has experienced no contraction in film thickness.

Figure 8.8 shows dislocation behavior within wider ligaments during indentation of the same 75 nm np-Au film. Prior to deformation (Figure 8.8a), the ligaments are nearly free of dislocations. After ~33 sec of indentation, there has been a significant amount of dislocation activity. Dislocations are seen in the ligament to the right of center, oriented perpendicular to the film surface. Additionally, the thin ligament (beneath the center of Figure 8.8a) has been sheared nearly to the point of rupture in Figure 8.8b. It should also be noted that, in the video sequences that yielded Figures 8.7 and 8.8, the motion of the indenter was observed to be jerky (as opposed to smooth), suggesting irregularities during the deformation of np-Au. This jerky motion was observed in the majority of indentation tests.

The collapse of a pore during indentation of annealed np-Au is shown in Figure 8.9. This 300 nm annealed film contains wider ligaments (~30 nm) and larger pores (~20 nm) than the as-dealloyed films. A pore can be seen slightly to the left of center in Figure 8.9a, in the middle of the np-Au film. The pore overlaps with a ligament, lowering the contrast at the edges, although the pore is still identifiable. During indentation, numerous dislocations move through the ligaments surrounding the pore. At the same time, the pore is gradually compressed to a flattened, oval shape in Figure 8.9b. The change in pore shape is not sudden, but instead is continuous and smooth, as was also observed for other pores during subsequent indentation tests.

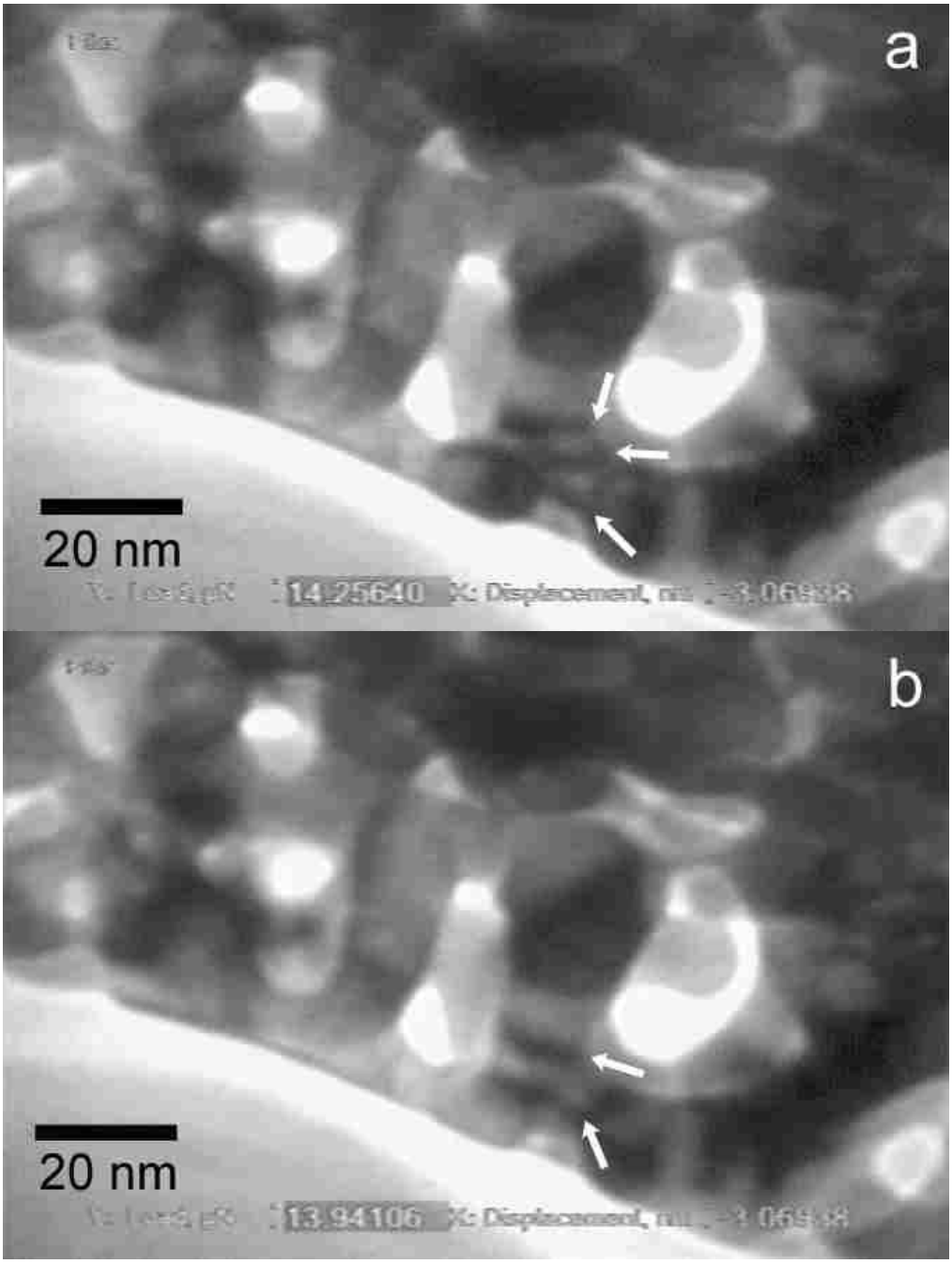

Figure 8.7 Still images from video sequence acquired during indentation of an as-dealloyed 75 nm np-Au film. Dislocations, for example the series of three dislocations in the lower/central region of image (a), are readily created during indentation, undergoing glide along the axes of the Au ligaments and interacting with other defects in the nodes of the nanoporous structure. (b) 100 frames (3.33 sec) later, one of the dislocations has moved up and into the node, leaving two dislocations in the ligament. Displacement rate of the indenter tip was 30 nm/s.

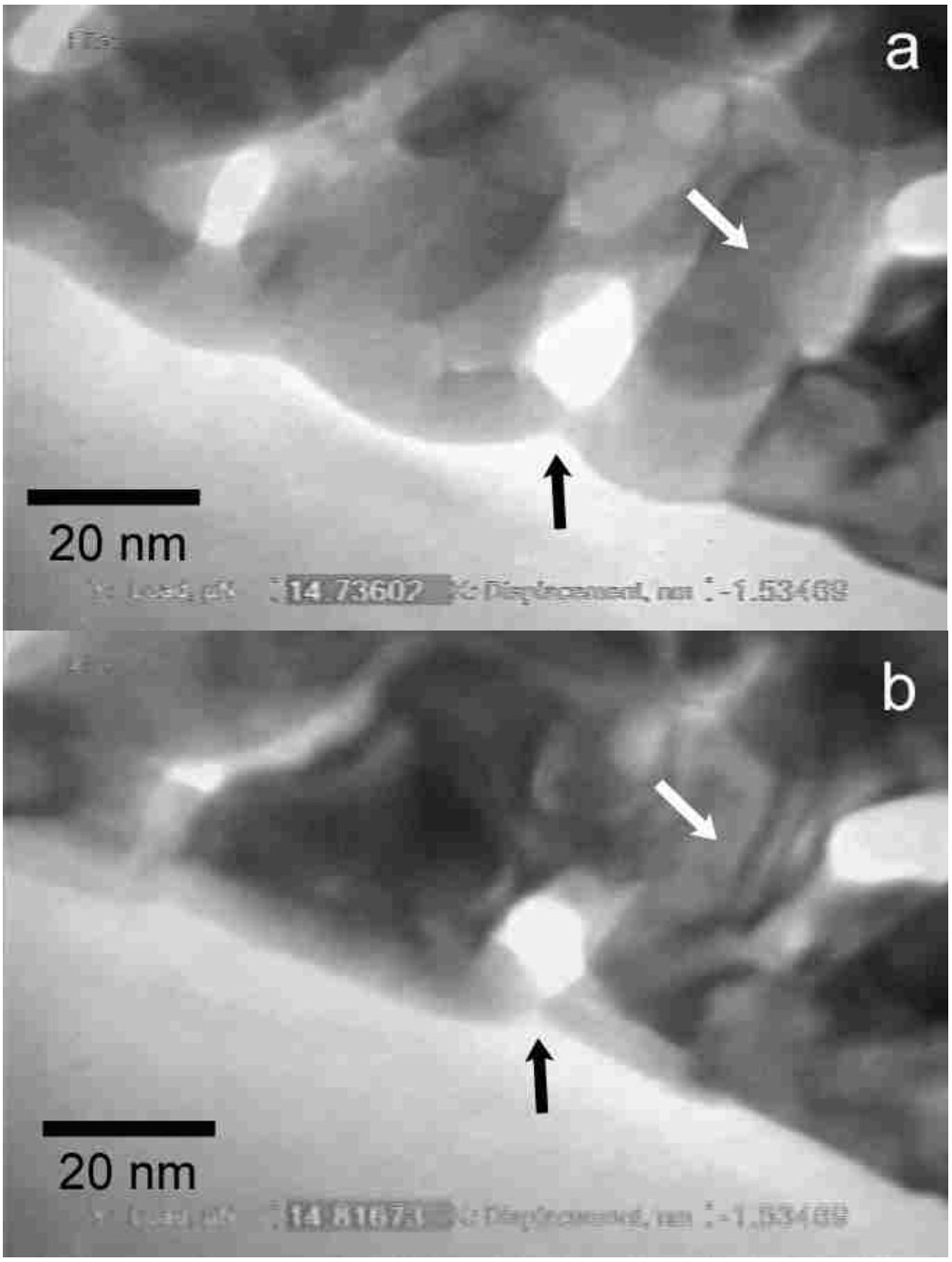

Figure 8.8 (a) A second location in the 75 nm np-Au film, prior to indentation. (b) Microstructure after indentation (~33 sec after the first image). A wider ligament, on the right side of these images, experiences more dislocation activity than shown in Figure 8.7. Also note the thin ligament at the film surface, which has nearly been sheared apart in (b).

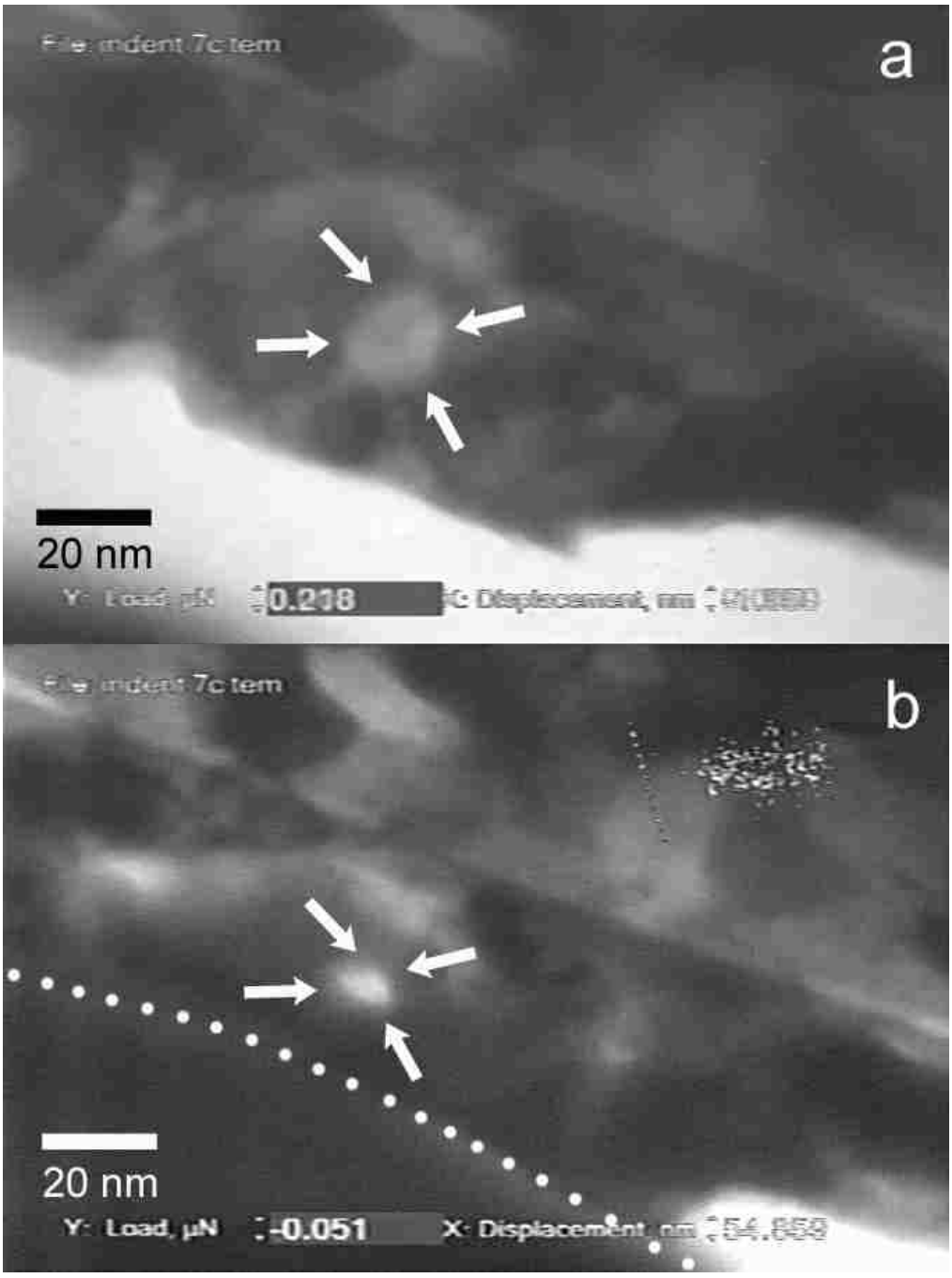

Figure 8.9 75 nm np-Au film after annealing at 200˚C. (a) Before indentation begins. (b) Near the end of indentation. During indentation (displacement rate of 6 nm/s), the pore in the center of the film collapses continuously (not abruptly). Before and during pore collapse, there is significant dislocation activity within the ligaments surrounding the pore.

The np-Au films with 75 nm film thickness (Figures 8.6-8.9) were ideal for obtaining micrographs of the porous structure and *in situ* videos of indentation, due to their electron transparency and minimal overlap of ligaments in the two-dimensional projected TEM images. However, the 75 nm films did not facilitate sufficient indentation depth to obtain meaningful load-displacement curves. The 150 and 300 nm np-Au films, although not ideal for observation of microstructure and dislocations, yielded interpretable and repeatable indentation curves for the measurement of mechanical behavior.

Load drops were observed during indentation of the thicker np-Au films. This is apparent in the load-displacement plots of Figure 8.10, each with a consistent spacing between load drops. The curves in Figure 8.10 were obtained from annealed 300 nm np-Au that was indented at various displacement rates, decreasing from 30 nm/s in Figure 8.10a to 7.5 nm/s in Figure 8.10d. This was done to investigate the effect of loading rate on deformation behavior. The spacing of the load drops decreases with decreasing displacement rate, and at the highest rate (Figure 8.10a) appears to be as large as ~20 nm. Figure 8.10a also exhibits smaller, more closely spaced load drops. It is noted that Figure 8.10b, which was obtained at a displacement rate very similar to that for Figure 8.10a, reveals numerous load drops spaced much more closely (~11 nm). This discrepancy in interval spacing may be due to the identification of each load drop, which may not always be straightforward.

Similar tests were performed on an as-dealloyed 300 nm np-Au film, but over a broader range of indenter displacement rates. Figure 8.11 presents load-displacement data from five indentation experiments. As was the case in Figure 8.10, a decreasing rate of indenter displacement causes a decrease in the spacing of load drops. For the slowest loading rate (1.5 nm/s, Figure 8.11e), the load drop interval is so short that the load data appear to be noisy, exhibiting a large amount of scatter. As shown in Figure 8.11f, however, this variation in load during indentation is still due to discrete load drops. Without knowledge of the dependence of load drop interval on loading rate, one could mistakenly attribute the load variations to scatter.

It is noted that the horizontal scatter in displacement data is much less in Figures 8.10-8.11 than in previously published load-displacement curves [82]. The improved data

quality is due to improved control electronics, resulting in a lowering of the noise in the tip displacement during indentation for the latter sets of experiments. This improvement allows the observation of very closely spaced load drops, such as those in Figures 8.11e-f.

8.4 Discussion

Significant numbers of dislocations were nucleated and underwent glide during the indentation of np-Au. This was observed during all indentation tests, as shown for example in Figures 8.7-8.9. Plasticity in this material is carried by dislocations, and np-Au exhibits ductile behavior, as would be expected based on the behavior of bulk Au. This is in contrast to the brittle behavior of bulk np-Au, which typically cracks when subjected to tension or bending during handling. However, this apparent discrepancy is in agreement with the findings of Li and Sieradzki, who performed three-point bend tests on bulk np-Au samples of varying pore/ligament size and found that samples significantly larger than their intrinsic pore size were more brittle [63]. In the case of the thin films examined in the current study, film thickness is only 3-12 times the cell size (ligament width plus pore diameter) of the np-Au, and thus the films would be expected to behave in a more ductile fashion.

The decrease in the spacing of load drops at slower indentation rates could be due to a kinetic effect. A slower loading rate should allow more time for dislocation nucleation to occur, improving the ability of dislocation production to keep pace with the imposed deformation and thereby leading to more closely spaced load drops (in agreement with Figures 8.10 and 8.11). The question arose of whether the load drops occurred at a constant time interval (as opposed to a distance interval), which would strongly suggest a kinetic (or statistical) effect in the plastic deformation of np-Au films. In order to explore this idea, the indentation data from Figures 8.10 and 8.11 were also plotted as load-time curves. These are presented in Figures 8.12 and 8.13, and the curves exhibit load drops with distinctly different shapes than in the load-displacement plots. Indeed, the load drops are more easily identified in Figures 8.12 and 8.13 (e.g. compare Figures 8.10a and 8.12a; Figures 8.11c and 8.13c). In several cases, the load-time plots revealed load drops that were not seen in the load-displacement curves (e.g. Figure 8.12a

versus 8.10a), although after knowing they exist, the careful observer can perhaps notice these drops in the load-displacement curve.

Table 8.2 summarizes the average load drop intervals, as a function of loading rate, obtained from multiple tests on as-dealloyed and annealed 300 nm np-Au films. The spacing of load drops was first measured from the load-displacement curves (Figures 8.10 and 8.11) using the bottom edges of load dips. As a first estimate of the equivalent load drop interval in time, these average distances were divided by the indenter displacement rate for a given test. Finally, the intervals were measured from the load-time curves in Figures 8.12 and 8.13. Comparison of the two sets of time interval data indicates that the values are generally consistent, although certain disparities exist. These are due to the inability of load-displacement curves to reveal all load drops, which seems to be more of an issue at faster displacement rates. Overall, the data in Table 8.2 show that, as the indentation rate decreases, load drops occur at shorter distance intervals and longer time intervals.

Table 8.2 Average spacing between load drops measured during indentation of 300 nm np-Au films at various displacement rates. The temporal spacing of load drops was obtained in two ways: dividing the interval distance by loading rate, and measuring from load-time curves such as those in Figures 8.12 and 8.13.

Displacement rate (nm/s)	Load drop interval (nm)		Load drop interval (s) [Calculated]		Load drop interval (s) [Measured]	
	As-dealloyed	Annealed	As-dealloyed	Annealed	As-dealloyed	Annealed
30	13.20	11.00	0.440	0.367	0.440	0.447
28.125	-	11.00	-	0.391	-	0.379
15	12.54	10.25	0.836	0.683	0.829	0.700
7.5	7.02	8.36	0.936	1.11	0.914	1.13
3	3.50	-	1.17	-	1.24	-
1.5	3.26	-	2.17	-	2.16	-

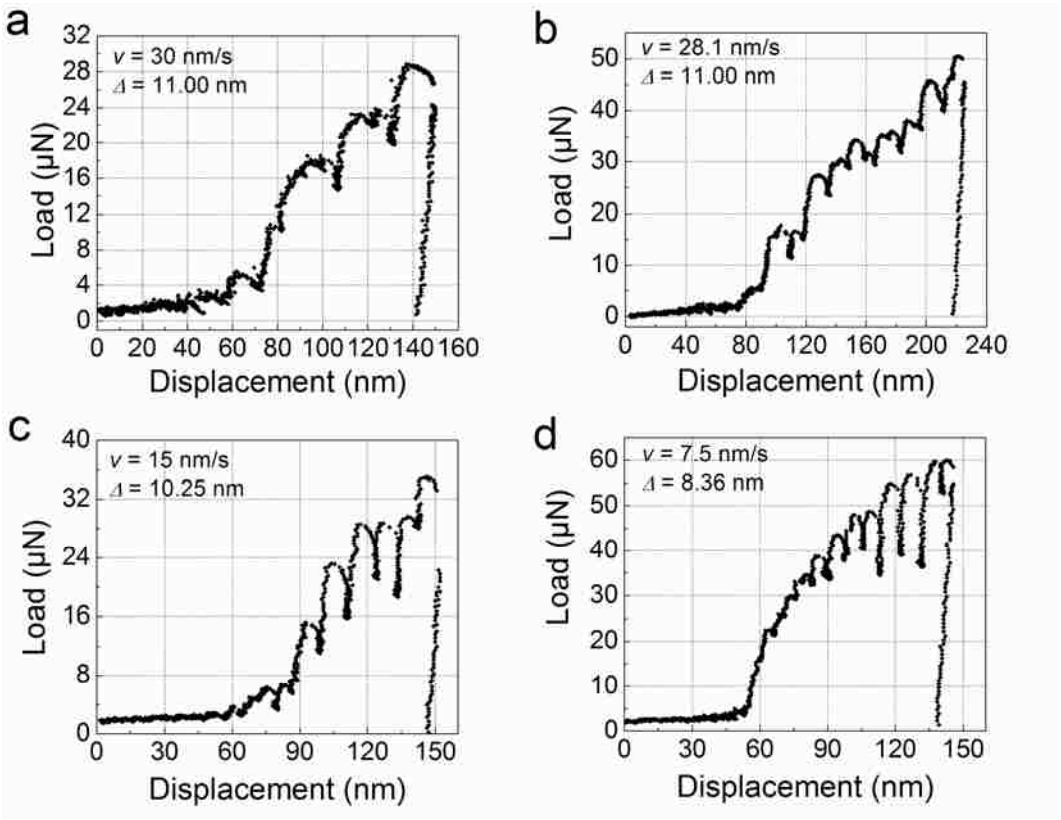

Figure 8.10 Load-displacement curves for an annealed 300 nm np-Au film indented at various displacement rates: (a) 30 nm/s; (b) 28.1 nm/s; (c) 15 nm/s; (d) 7.5 nm/s. As displacement rate decreases, the average interval between load drops decreases.

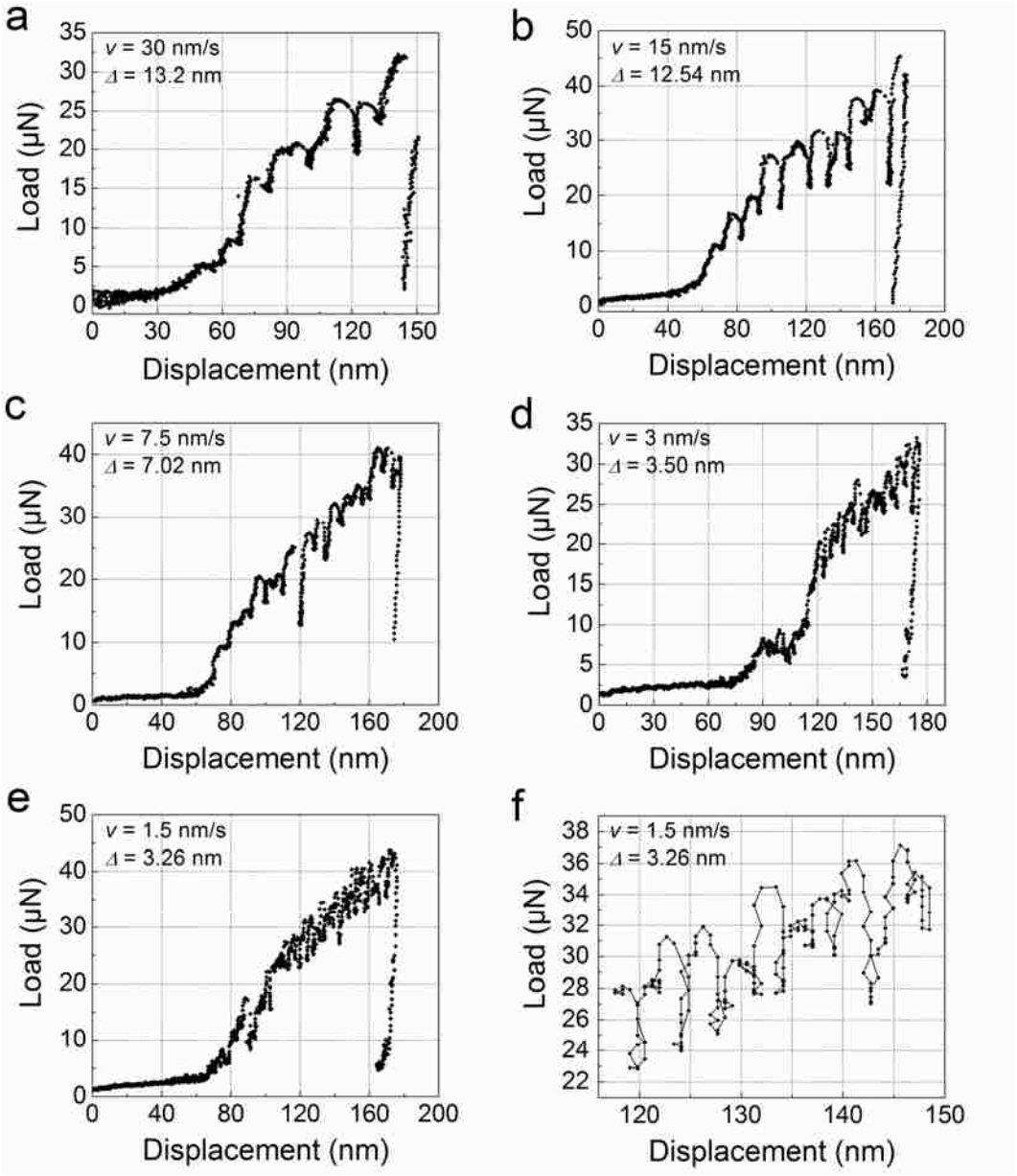

Figure 8.11 Load-displacement curves for an as-dealloyed 300 nm np-Au film indented over a broad range of displacement rates. (a) 30 nm/s; (b) 15 nm/s; (c) 7.5 nm/s; (d) 3 nm/s; (e) 1.5 nm/s. (f) Detailed view of the loading curve from (e), indented at 1.5 nm/s. As the displacement rate decreases, the average interval between load drops decreases so much that the data appear to suffer from a high amount of scatter. Figure (f), however, shows that actually this is not the case: the loading curve exhibits very closely spaced drops.

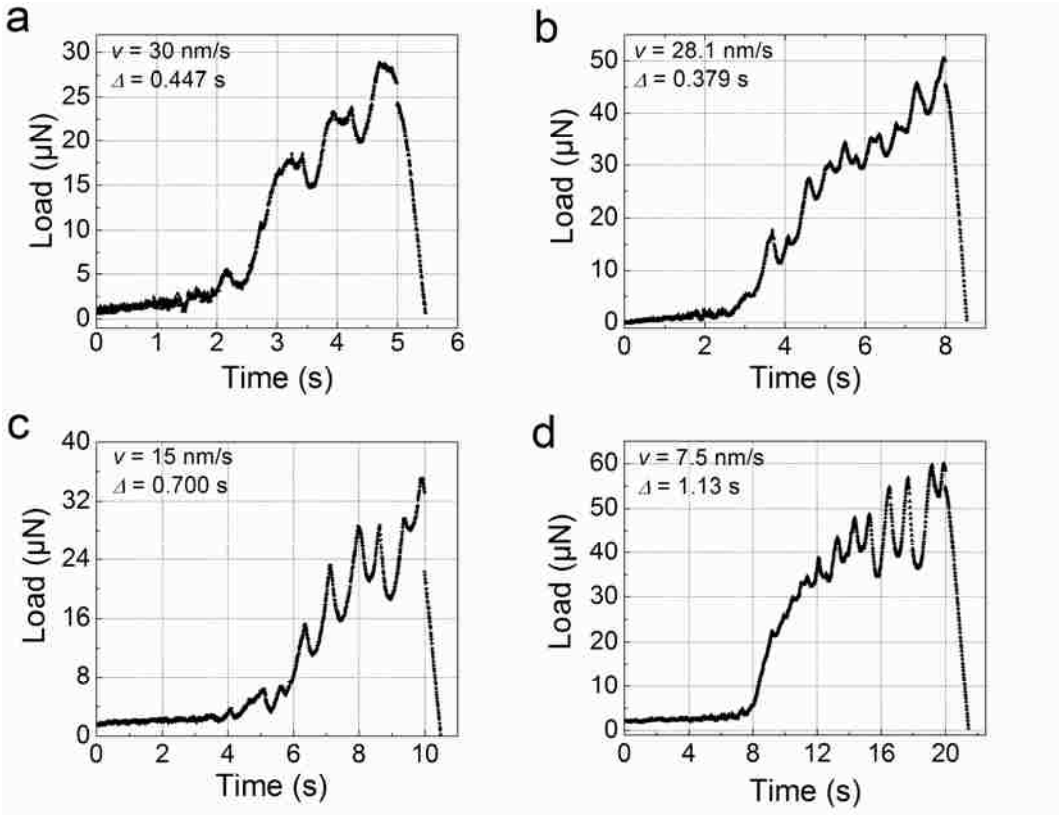

Figure 8.12 Load-time curves of the annealed 300 nm np-Au film deformed at various displacement rates. These plots were constructed from the same data used for Figure 8.10, but exhibit load drops with clearly different shapes. (a) 30 nm/s; (b) 28.1 nm/s; (c) 15 nm/s; (d) 7.5 nm/s. Load drops are more easily recognized in these load-time plots, which in some cases reveal additional load drops that are not apparent in the load-displacement curves.

Initially, it was believed that the spacing of load drops corresponded to the average pore size in the np-Au films [82]. The load-displacement curves from indentation of as-dealloyed 150 and 300 nm np-Au films exhibited load drops at regular intervals of ~10 nm. This interval spacing was equal to the average pore size calculated from measured ligament width and relative density, and the load drops were interpreted as resulting from the collective collapse of successive layers of pores during film compaction. To test this hypothesis, annealed np-Au was also indented, since it was known that annealing at 200˚C causes the ligament width to double but does not cause further contraction in the thickness of np-Au films on Si [72]. In light of the newer data

presented in this study, however, the spacing of load drops does not appear to be determined by pore size. Indeed, the annealed 300 nm np-Au film contains larger pores than the as-dealloyed film, yet exhibits load drops at shorter distance intervals (compare Figures 8.10a and 8.11a; compare Figures 8.10c and 8.11b). Additionally, the collapse of pores during slower loading experiments (e.g. 6 nm/s, as shown in Figure 8.9) is gradual, not abrupt, and thus would not explain the load drops. During indentation of thicker films at faster loading rates, however, the indenter motion was jerky and suggested that collective displacement such as pore collapse was occurring. Systematic testing of thinner films at varying loading rates, to observe the behavior of pores during indentation, would be helpful in clarifying this behavior.

In Figure 8.14, indenter load and displacement are plotted simultaneously versus time. It is seen that the load drops are accompanied by changes in the displacement rate, i.e. the rate of indenter displacement varies due to the load drops. These small displacement excursions (forward surges) occur because the feedback algorithm is not able to restore the position of the tip to its proper position in time. This is most noticeable at higher loading rates (Figure 8.14a). For slow loading (Figure 8.14c), the indenter displacement rate appears constant, because the control system has more time to counter gaments.

「

Figure 3.1 Schematic of setup for dealloying experiments????A??DC **voltage sup**ply

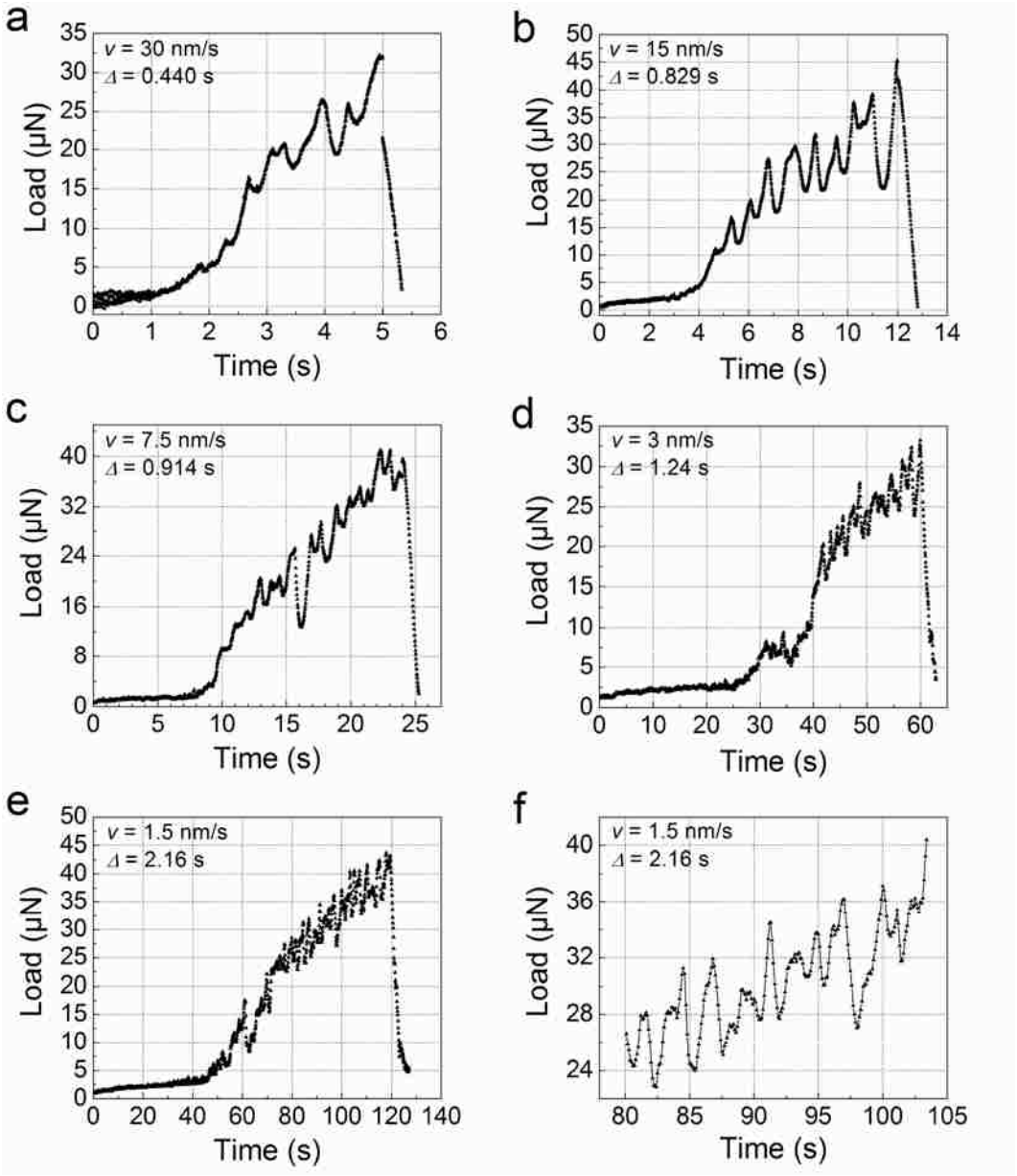

Figure 8.13 Load-time curves of the as-dealloyed 300 nm np-Au film deformed at various displacement rates. These plots are from the same tests portrayed in Figure 8.11. (a) 30 nm/s; (b) 15 nm/s; (c) 7.5 nm/s; (d) 3 nm/s; (e) 1.5 nm/s; (f) Detailed view of the plot from (e), showing the smooth distribution of data along the time axis (as compared to Figure 8.11f, where the load drops lead to multiple data points at certain displacements).

The intervals between load drops (in distance and in time) were plotted as a function of indenter displacement rate, on a log-log scale, to determine if there is a

functional dependence. No clear functionality was seen. The data are therefore plotted on a normal scale in Figure 8.15, which presents the average interval spacings for as-dealloyed and annealed 300 nm np-Au films (data taken from Table 8.2). Data for both specimens exhibit similar trends. In Figure 8.15a, it is seen that the distance interval increases with increasing displacement rate, and it appears that the distance interval may plateau at 10-14 nm. However, additional testing would be required in order to determine this conclusively. In Figure 8.15b, the time interval between load drops decreases with increasing displacement rate, but does not exhibit a plateau. This suggests that further increases in loading rate (above 30 nm/s) would reduce the time interval to the point where the load drops could not be identified as events, but instead would be on the order of the data sampling rate.

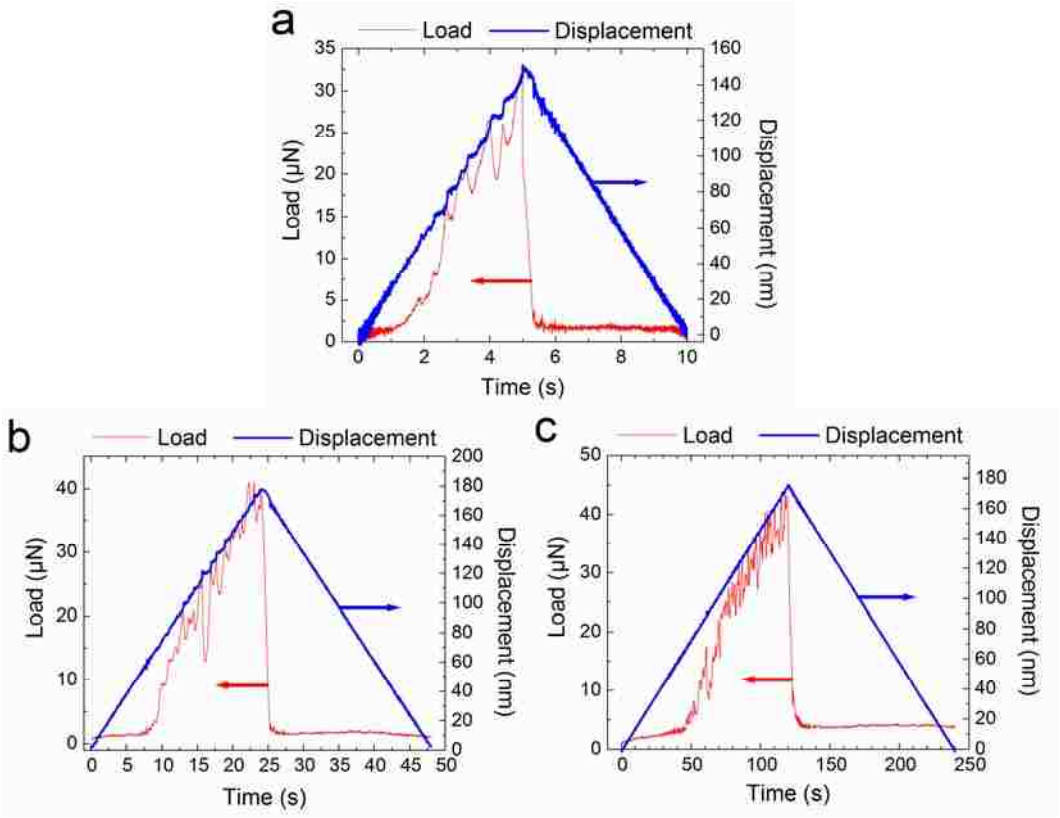

Figure 8.14 Overlaid plots of load and displacement versus time, for indents of the as-dealloyed 300 nm np-Au film from Figures 8.11 and 8.13. (a) 30 nm/s; (b) 7.5 nm/s; (c) 1.5 nm/s. At faster loading rates, e.g. 30 nm/s in (a), the clearly separated load drops lead to noticeable non-linearities in the displacement ramp, despite these tests being run in nominally displacement-controlled mode.

The spacing of load drops is clearly not governed by the pore size of np-Au, and these drops do not occur at a fixed interval of time or distance. However, the porous structure may still play a role in the observation of load drops during *in situ* nanoindentation. We postulate that the interval spacing is related to the collective deformation of ligaments and mediation of plasticity by dislocations in np-Au.

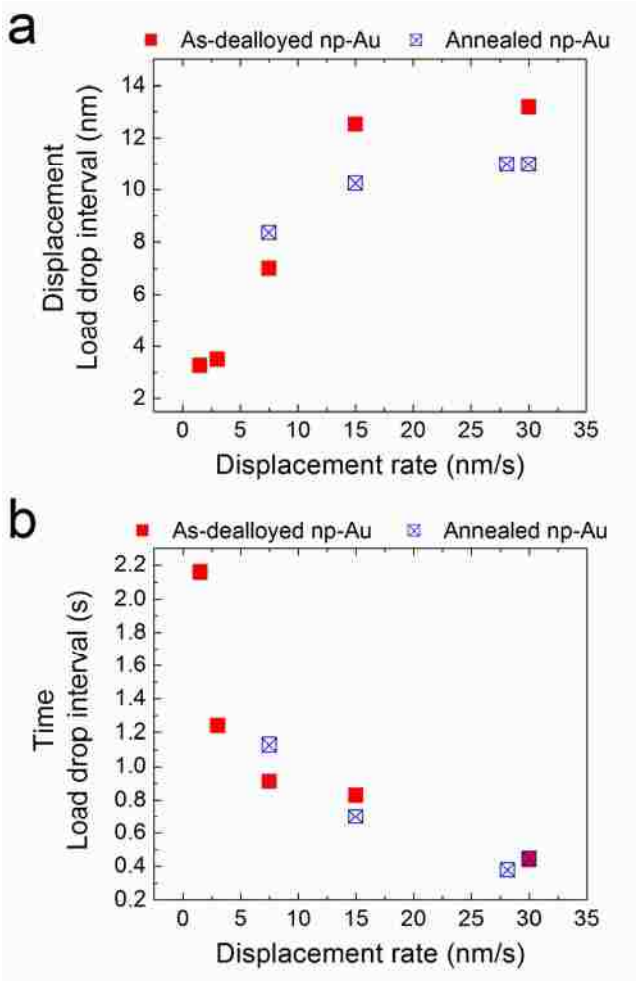

Figure 8.15 Plots of the average interval between load drops as a function of indenter displacement rate (data taken from Table 8.2). For both the as-dealloyed and annealed 300 nm np-Au films, higher displacement rates lead to (a) increases in the distance between load drops and (b) decreases in the time between load drops.

At the lowest loading rates, dislocations have ample time to nucleate and carry the imposed deformation. As the indenter displacement rate is increased, the material must respond by deforming more quickly, and the time interval between load drops decreases.

At the same time, dislocation nucleation, which is kinetically limited, may not be able to supply adequate numbers of dislocations to accommodate smooth and continuous plastic deformation. Strain energy accumulates within the np-Au ligaments and, when it is released, causes load drops that represent a burst of dislocation motion.

It is not yet completely clear how the nucleation and motion of dislocations affect the relationship between loading rate and load drop intervals. Further studies will be performed to investigate this in more detail.

8.5 Summary

In summary, *in situ* nanoindentation was performed on np-Au films inside the TEM. Deformation of np-Au proceeds via compaction of ligaments under the indenter, with the compaction zone gradually growing and passing through successive layers of the nanoporous structure. Although compaction of the overall np-Au film was accompanied by these discontinuities, individual Au ligaments deformed in a smooth and clearly ductile manner. It was also observed that dislocations were generated within the nanoscale ligaments (10-20 nm wide) of np-Au and moved easily along the ligaments during indentation. In other words, individual Au ligaments behaved as one would expect for a ductile metal such as Au. The nanoscale structure, however, provides additional constraints on dislocation motion and thereby changes the overall deformation response of np-Au.

Annealing did not cause further thickness reduction. Load-drops observed in the load-displacement curves were firstly thought to correspond to the collective collapse of rows of pores. Further experiments proved that the spacing of load drops is clearly not governed by the pore size of np-Au, and these drops do not occur at a fixed interval of time or distance. However, the porous structure may still play a role in the observation of load drops during *in situ* nanoindentation. We postulate that the interval spacing is related to the collective deformation of ligaments and mediation of plasticity by dislocations in np-Au.

Chapter 9

Summary and Overview

9.1 Concluding remarks

This doctoral work has involved the optimization of fabrication conditions, investigation of microstructural evolution during processing, and the study of mechanical behavior of np-Au in bulk and thin film form. Combining these aspects has yielded a better understanding of the underlying mechanisms behind dealloying and the structure-mechanical property relationships in this material.

In both bulk and thin film systems, significant advances were made in improving the structural integrity of np-Au by producing crack-free specimens that are better suited for practical application. The results of these studies on improving fabrication processes of np-Au, as well as the mechanism of pore formation during dealloying, will improve the understanding of these open topics. It was revealed that initial dealloying rate and Au percentage in precursor alloys are critical to crack formation. Np-Au films produced from 25 at.% Au alloy films showed extensive cracking, whereas 30 at.% Au np-Au films carried high tensile stress but did not crack, suggesting that stress may play an important role in ligament coarsening. Ligaments grew faster when np-Au films were subjected to residual tensile stress. Another finding related to diffusion is that ligaments of bulk np-Au coarsen differently, depending on the environment in which it is annealed. This difference was likely due to the slower diffusion of Au in vacuum than in air.

The results obtained from mechanical behavior studies of np-Au by microindentation, wafer curvature, and *in situ* nanoindentation have provided a well rounded set of data for comparison with other well-used techniques, such as conventional nanoindentation. Particularly, dislocation-related deformation was studied by *in situ* TEM, and could help to explain the unique properties of np-Au, such as the finding that the strength of a single ligament is close to the theoretical strength of Au.

9.2 Key findings

The results from the study of bulk np-Au (25 at.% Au in the precursor alloy) can be summarized as follows:

- Cracking is a prominent byproduct associated with the dealloying of 25 at.% np-Au, which can be improved by changing starting composition of precursor alloys and the dealloying conditions.
- Ligament coarsening occurred when bulk np-Au was annealed at 300°C and above, but significantly different morphology evolution was observed depending on environment. For annealing in vacuum, the underlying mechanism of coarsening is most like sintering, whereas Ostwald ripening appears to be the primary mechanism when ligaments coarsen in air. One important finding is that np-Au may be more thermally stable in vacuum applications than in air.
- Microhardness of np-Au generally increased with increasing annealing temperature, although this was not a monotonic trend. The inconsistent trend of hardness with temperature was thought to result from interaction between the microindenter and cracks caused by dealloying.
- Deformation of np-Au changed from brittle to ductile when ligaments coarsened. Fused grain boundaries appeared when np-Au was annealed above 400°C, resulting from sintering of neighboring Au atoms.

The results from the study of bulk np-Au (30 at.% Au in the precursor alloy) can be summarized as follows:

- Crack-free bulk np-Au with millimeter dimensions and exhibiting no volume change was produced by a two-step dealloying method. A galvanostatic approach combined with the use of 1:2 diluted HNO_3 followed by concentrated HNO_3 is well suited to the fabrication of millimeter-scale bulk np-Au with no cracking or volume contraction. The most important aspect of the two-step dealloying method is that it slows the initial etch rate.

- Grain boundaries and twins on alloy surfaces were retained during dealloying, even though nearly all Ag was removed from the precursor alloy. Isolated cracks were observed in dealloyed np-Au, but these were few in number and did not cause the specimen to break during handling or otherwise compromise mechanical integrity.
- Various types of dealloyed grain boundaries were observed in fully dealloyed samples (open, closed, or continuous/fused GBs). It is postulated that this variety in GB morphology is due to the character of the original GB, which should affect diffusion and dissolution rates.
- Focused ion beam exposure caused rapid and severe cracking and coarsening of the np-Au structure. Therefore, care must be taken when using ion beam milling to prepare samples from this fragile material.

The results from the study of np-Au thin films (25 at.% Au in the precursor alloy films) can be summarized as follows:

- Adhesion of np-Au to both substrate types was significantly enhanced by depositing a Ta interlayer and a Au interlayer before alloy deposition.
- Pore formation during dealloying was rapid, producing a nanoporous structure throughout the film thickness within 1 min. Further dealloying caused the structure to coarsen.
- Film cracking was prevalent and formed very quickly in all np-Au films produced from the 25 at.% Au precursor alloy, perhaps due to preferential dealloying at certain grain boundaries.
- Thermal cycling of thin films did not induce a significant stress in the np-Au, perhaps due to the extensive film cracking that may have accommodated any expansion or contraction of the film.
- Both Ag content and film stress decreased significantly and rapidly during dealloying, and these changes occurred before ligament width began to increase appreciably.

- Dealloying generally caused cracking, followed by subsequent stress increases and then stress relaxation, eventually leading to a stress-free state at extended times. Film cracking could account for the measured stress relaxation.
- Ligament width was found to increase with dealloying time according to $w \propto t^{1/8}$.

The results from the study of np-Au thin films (30 at.% Au in the precursor alloy films) can be summarized as follows:

- The biaxial stress of np-Au films during thermal cycling exhibited a dependence on film thicknes. The equivalent bulk yield strength of Au ligaments was calculated to be at least 2.0 GPa for a 75 nm np-Au film. This corresponds to a resolved $\tau \approx \mu/49$, close to the theoretical shear strength of bulk Au.
- Completely crack-free np-Au thin films on Si substrates have been processed by dealloying and thermal cycling. The ligament width of np-Au films remains constant during cycling to 100˚C, but doubles during cycling to 200˚C. Dealloying generates high tensile stresses in thin film np-Au, regardless of whether the film is initially under tension or compression.
- Dealloying did not occur preferentially at grain boundaries, but instead at central regions of grains. This may be due to aggregation of Ag at grain centers.
- There are two mechanisms that govern the stress change during dealloying: Ag dissolution causes tensile stress, whereas ligament coarsening results in compressive stress.
- The thinner the film, the easier it is to remove or dissolve Ag atoms. Two-step dealloying combining free corrosion and electrochemical dealloying, produced crack-free films with considerably lower residual Ag content.
- Ligament coarsening of 30 at.% np-Au films is time dependent and follows a power law of $t^{0.24}$, which is much faster than the time dependence of $t^{0.13}$ for 25 at.% films. Residual stress may be responsible for the difference: a biaxial stress in 30 at.% Au films facilitates diffusion of Au atoms along both parallel

and perpendicular ligament axes, resulting in faster growth ofligament width as well as length.

The *in situ* TEM studies of np-Au thin films can be summarized as follows:

- Deformation of np-Au proceeds via compaction of ligaments under the indenter, with the compaction zone gradually growing and passing through successive layers of the nanoporous structure.
- Individual Au ligaments deformed in a smooth and clearly ductile manner. Dislocations were generated within the nanoscale ligaments (10-20 nm wide) of np-Au and moved easily along the ligaments during indentation.
- The spacing of load drops is clearly not governed solely by the pore size of np-Au, and these drops do not occur at a fixed interval of time or distance. It is postulated that the interval spacing is related to the collective deformation of ligaments and mediation of plasticity by dislocations in np-Au.

9.3 Future work

One interesting finding of the present work is that the morphology of np-Au thin films evolved differently than was expected from the existing model of Erlebacher. This provides an opportunity for a new or at least an improved understanding of the mechanism of dealloying. However, it was difficult to mornitor the initial stages of the dealloying process, even after several seconds, due to the rapid diffusion rate of both Au and Ag in concentrated HNO_3. Etching Au-Ag films using dilute HNO_3 could illuminate the dealloying process and allow longer windows of time to observe the evolution of pit formation, width change, and possible shrinkage. Plan-view and cross-sectional SEM images of np-Au films dealloyed for short periods of time could serve this purpose. Moreover, a TEM study of np-Au films dealloyed by dilute etchant at short times could further reveal details of Ag dissolution, pit or pore formation, and coalescence of pits. It is suggested that atom-probe field-ion microscopy (APFIM) may be used to identify factors, such as Ag concentration of GBs versus grain interior regions, which will shed more light on the dealloying mechanism. *In situ* nanoindentation inside the TEM provided unique observations of dislocation interactions in np-Au during deformation. However, there is an absence of high-resolution TEM studies of dislocations produced during *in situ* nanoindentation. Such high-resolution TEM images should help clarify the doubt one might have about as to whether these claimed dislocations are instead due to contrast differences in the conventional TEM images.

Another fundamental finding of the present study is that ligament coarsening appears to be dependent on residual stress in the np-Au films: ligament growth followed a power law of $t^{1/8}$ for stress-free np-Au films, whereas $t^{1/4}$ was followed by films carrying tensile stress. To further study this topic, np-Au films with various stress can be fabricated by varying film thickness or deposition conditions (e.g. substrate bias, ion bombardment) and then studied during ligament coarsening.

Wafer curvature is an effective method to explore mechanical properties of np-Au films on substrates. Coarsening of ligaments hindered the analysis of mechanical behavior of np-Au films due to changes in microstructure, but elastic modulus can still be

calculated from the slopes of stress-temperature curves. Size effects of ligaments on elastic modulus of np-Au can be studied by annealing np-Au to various temperatures to obtain a range of ligament sizes. These np-Au films can be cooled to –70 °C to calculate elastic modulus from stress-temperature curves. Additionally, the fact that thinner np-Au films carried higher residual stresses warrants further study. Actual relative density or porosity of np-Au films from Au-Ag alloy films with different thickness, but the same composition, may vary because of differences in the ease of dissolving Ag atoms from the films. Actual relative density must play a role in residual stress difference as a function with thickness. Two types of experiments can be used to study the effect of porosity on the residual stress in np-Au films. (1) Np-Au films with the same thickness but varying relative density by dealloying Au-Ag films with different Au/Ag ratios. (2) Np-Au films with different thickness but having same relative densities to explore the thickness effect.

Using wafer curvature, another important quality, activation energy, can be measured by stress relaxation tests. These tests can be performed by heating np-Au films to a high temperature and cooling them to certain temperatures for isothermal annealing steps.

Although the present work focused on mechanical properties of np-Au, studies on its applications are equally important and worthy of additional effort. Np-Au has been reported to have applications such as catalysis, sensing and capacitance. Further studies can focus on the catalytic properties of np-Au in the conversion of CO to CO_2, or investigate changes in electrical or other properties when exposed to gases. These properties can be correlated to the surface properties of np-Au. Absent in the present study, to some degree, properties such as size, shape and distribution of pores in np-Au will be critical issues in those complex structural systems. They are very important to successful implementation of the structural/catalytic efficiency. Using physisorption techniques, such as BET nitrogen analysis, surface area and porosity of np-Au sholuld be characterized.

Appendix A

Standard Operating Procedure for Dealloying with Nitric Acid in the Fume Hood

Dealloying is a chemical etching/dissolution process whereby the less noble element in a binary single-phase alloy is removed into the etchant solution (nitric acid is a common etchant for this purpose). For example, Au-Ag alloys, which are perfectly miscible and form no second phases, can be dealloyed using concentrated nitric acid, which dissolves the Ag atoms and leaves the Au atoms behind as a solid material. Another example of dealloying involves Pd-Ag, which is also etched with nitric acid.

DEALLOYING WITH NITRIC ACID MUST BE PERFORMED IN THE FUME HOOD!

Warning: concentrated nitric acid is a highly corrosive and toxic acid that can cause severe burns to your skin. It is also a strong oxidizer and must not be mixed with organic solvents, e.g. alcohols such as ethanol and isopropanol, or ketones such as acetone. Nitric acid and the ethanol used for the final rinse must NEVER be mixed with each other. When mixed, the product fumes strongly and, if sealed within a capped container, can create sufficient pressure to cause that container to explode.

Familiarize yourself with the MSDS sheets for nitric acid BEFORE performing dealloying. You should also know, understand and practice the steps you must take if nitric acid comes into contact with your skin.

In case of exposure to a small area, flush the skin with large amounts of water for 15 minutes. If a large area of skin has been exposed to nitric acid, immediately go under the shower and rinse all affected areas for 15 minutes. Also, neutralize any remaining acid by generously applying sodium bicarbonate to all exposed areas. (For additional information, see the red/white posted sign regarding nitric acid).

<u>General guidelines for chemical work include:</u>

- Always work with the smallest amount of each chemical that is required.
- When working in the fume hood, remove all containers and chemicals that are not required for the experiment you are performing at that time. Properly store all containers/chemical that you remove.
- Paper towels and Kimwipes that have been used to absorb acids should be sealed in the appropriate solid waste container. Avoid letting nitric acid and organic solvents come into contact, both in the hood and in the trash!

- When working with chemicals in the fume hood, make sure that you are not alone and that a coworker is (1) aware of the procedure you are performing and (2) nearby in case you need help during an emergency.

For **chemical dealloying** (without a voltage supply), perform the following steps:

1. Put on lab coat and vinyl gloves (not nitrile gloves). Make sure that the gloves extend over the cuffs of the lab coat, such that your forearms are completely covered. If necessary, bind the sleeve of each glove so that it secures the cuffs of your lab coat.
2. Wear the ventilated goggles with attached face shield BEFORE starting (and of course during) your work with nitric acid.
3. Set the sash height at the correct operating level for the fume hood. Always make sure that the sash is between your face and the acid/solvent/waste containers, to provide maximum protection in case of a reaction or explosion.
4. Pour nitric acid (HNO_3, stock concentration) into a Petri dish, such that the liquid level is sufficiently high to completely cover the specimen. Use the smallest Petri dish that is suitable for the specimen, and use the minimum amount of acid that will suffice.
5. Place a label beneath or beside the Petri dish indicating that it contains nitric acid.
6. Prepare two separate dishes, one with water and one with ethanol (if necessary), for rinsing the specimen after dealloying. Label each container appropriately.
7. Place the sample into the acid and cover the Petri dish with the corresponding glass cover or with a watch glass.
8. Leave the sample in the acid for the appropriate length of time (generally 1 to 30 minutes).
9. Remove the cover from the Petri dish and place it on a paper towel.
10. Using stainless steel tweezers, remove the specimen from the nitric acid bath.
11. Touch the edge of the specimen to a paper towel in order to wick away excess nitric acid.
12. Immerse the specimen in the water bath to remove nitric acid residue.
13. Rinse the specimen with ethanol, and if necessary immerse the specimen in ethanol, for a final rinse.
14. Place the specimen on a Kimwipe while the ethanol dries from the surface.
15. Empty the used nitric acid into the hazardous waste container labeled “Nitric Acid”. Use a funnel to facilitate pouring the waste.
16. Empty the used ethanol into the hazardous waste container labeled “Ethanol/IPA/Acetone”. Use a funnel to facilitate pouring the waste.
17. Rinse all containers in the sink and immediately wash all containers thoroughly.

For **electrochemical dealloying** (with a voltage supply), perform the following steps:

1. Set up the 250 mL beaker, dry electrodes, electrical wires, power supply and multimeter to construct the electrochemical circuit. Wear gloves, lab coat and safety glasses, since this work is being done in the fume hood.
2. Change your protective clothing to that required for chemical dealloying with nitric acid, i.e. vinyl gloves, lab coat and ventilated goggles with attached face shield.
3. Set the sash height at the correct operating level for the fume hood. Always make sure that the sash is between your face and the acid/solvent/waste containers, to provide maximum protection in case of a reaction or explosion.
4. Pour nitric acid (HNO_3, stock concentration) into the beaker that will contain the electrochemical cell, such that the liquid level is sufficiently high to completely cover the specimen. Use the minimum amount of acid that will suffice.
5. Place a label beneath or beside the beaker indicating that it contains nitric acid.
6. Place the sample in the electrochemical cell with nitric acid for the appropriate length of time (generally 16 to 50 hours), with the voltage supply set at 1V. Periodically check the voltage supplied to the specimen and the current flowing through the specimen.
7. When the dealloying process is near completion, prepare two separate dishes, one with water and one with ethanol (if necessary), for rinsing the specimen after dealloying. Label each container appropriately.
8. After the desired amount of time, carefully remove the specimen from the nitric acid bath.
9. Touch the edge of the specimen to a paper towel in order to wick away excess nitric acid.
10. Immerse the specimen in the water bath to remove nitric acid residue.
11. Rinse the specimen with ethanol, and if necessary immerse the specimen in ethanol, for a final rinse.
12. Place the specimen on a Kimwipe while the ethanol dries from the surface.
13. Empty the used nitric acid into the hazardous waste container labeled “Nitric Acid”. Use a funnel to facilitate pouring the waste.
14. Empty the used ethanol into the hazardous waste container labeled “Ethanol/IPA/Acetone”. Use a funnel to facilitate pouring the waste.
15. Rinse all containers and electrodes in the sink. Immediately wash all containers thoroughly.
16. Unplug the power supply.
17. Wipe down the power supply, electrical wires and multimeter with fresh paper towels that have been moistened with water and squeezed out.

References

1. Lin, V.S.Y., et al., *A porous silicon-based optical interferometric biosensor.* Science, 1997. **278**(5339): p. 840-843.
2. Stefanou, N., A. Modinos, and V. Yannopapas, *Optical transparency of mesoporous metals.* Solid State Communications, 2001. **118**(2): p. 69-73.
3. Martin, C.R., *Nanomaterials - a Membrane-Based Synthetic Approach.* Science, 1994. **266**(5193): p. 1961-1966.
4. Haupt, M., et al., *Nanoporous gold films created using templates formed from self-assembled structures of inorganic-block copolymer micelles.* Advanced Materials, 2003. **15**(10): p. 829-831.
5. Jiang, P., J.F. Bertone, and V.L. Colvin, *A lost-wax approach to monodisperse colloids and their crystals.* Science, 2001. **291**(5503): p. 453-457.
6. Attard, G.S., et al., *Mesoporous platinum films from lyotropic liquid crystalline phases.* Science, 1997. **278**(5339): p. 838-840.
7. Jin, I., L.D. Kenny, and H. Sang, *Method of producing lightweight foamed metal*. U.S. Patent No. 4973358, 1990
8. Erlebacher, J., et al., *Evolution of nanoporosity in dealloying.* Nature, 2001. **410**(6827): p. 450-453.
9. Gibson, L.J., *Mechanical behavior of metallic foams.* Annual Review of Materials Science, 2000. **30**: p. 191-227.
10. Shapovalov, V., *Porous Metals.* Mrs Bulletin, 1994. **19**(4): p. 24-28.
11. Hayes, J.R., et al., *Monolithic nanoporous copper by dealloying Mn-Cu.* Journal of Materials Research, 2006. **21**(10): p. 2611-2616.
12. Min, U.S. and J.C.M. Li, *The Microstructure and Dealloying Kinetics of a Cu-Mn Alloy.* Journal of Materials Research, 1994. **9**(11): p. 2878-2883.
13. Moffat, T.P., F.R.F. Fan, and A.J. Bard, *Electrochemical and Scanning Tunneling Microscopic Study of Dealloying of Cu3au.* Journal of the Electrochemical Society, 1991. **138**(11): p. 3224-3235.
14. Pickering, H.W., *Stress Corrosion Via Localized Anodic Dissolution in Cu-Au Alloys.* Corrosion, 1969. **25**(7): p. 289-290.
15. Kabius, B., H. Kaiser, and H. Kaesche, *A Micromorphological Study of Selective Dissolution of Cu from Cupd-Alloys.* Journal of the Electrochemical Society, 1986. **133**(8): p. C304-C304.
16. Sieradzki, K., et al., *The dealloying critical potential.* Journal of the Electrochemical Society, 2002. **149**(8): p. B370-B377.
17. Forty, A.J., *Corrosion Micro-Morphology of Noble-Metal Alloys and Depletion Gilding.* Nature, 1979. **282**(5739): p. 597-598.
18. Forty, A.J. and P. Durkin, *A Micro-Morphological Study of the Dissolution of Silver-Gold Alloys in Nitric-Acid.* Philosophical Magazine a-Physics of Condensed Matter Structure Defects and Mechanical Properties, 1980. **42**(3): p. 295-318.
19. Forty, A.J. and G. Rowlands, *A Possible Model for Corrosion Pitting and*

Tunnelling in Noble-Metal Alloys. Philosophical Magazine a-Physics of Condensed Matter Structure Defects and Mechanical Properties, 1981. **43**(1): p. 171-188.
20. Pryor, M.J. and J.C. Fister, *The Mechanism of Dealloying of Copper Solid-Solutions and Intermetallic Phases.* Journal of the Electrochemical Society, 1984. **131**(6): p. 1230-1235.
21. Pickering, H.W. and C. Wagner, *Electrolytic Dissolution of Binary Alloys Containing a Noble Metal.* Journal of the Electrochemical Society, 1967. **114**(7): p. 698-706.
22. Gardiazabal, J.I. and J.R. Galvele, *Selective Dissolution of Cd-Mg Alloys .1. Static Samples.* Journal of the Electrochemical Society, 1980. **127**(2): p. 255-258.
23. Gardiazabal, J.I. and J.R. Galvele, *Selective Dissolution of Cd-Mg Alloys .2. Rotating-Ring Disk Electrode.* Journal of the Electrochemical Society, 1980. **127**(2): p. 259-265.
24. Dubinin, M.M., *The Potential Theory of Adsorption of Gases and Vapors for Adsorbents with Energetically Nonuniform Surfaces.* Chemical Reviews, 1960. **60**(2): p. 235-241.
25. Everett, D.H., *Manual of Symbols and Terminology for Physicochemical Quantities and Units, Appendix II: Definitions, Terminology and Symbols in Colloid and Surface Chemistry.* Pure and Applied Chemistry, 1972. **31**(4): p. 577-638.
26. Weissmuller, J., et al., *Charge-induced reversible strain in a metal.* Science, 2003. **300**(5617): p. 312-315.
27. Kramer, D., R.N. Viswanath, and J. Weissmuller, *Surface-stress induced macroscopic bending of nanoporous gold cantilevers.* Nano Letters, 2004. **4**(5): p. 793-796.
28. Cortie, M.B., A.I. Maaroof, and G.B. Smith, *Electrochemical capacitance of mesoporous gold.* Gold Bulletin, 2005. **38**(1): p. 14-22.
29. Lowe, C.R., *Nanobiotechnology: the fabrication and applications of chemical and biological nanostructures.* Current Opinion in Structural Biology, 2000. **10**(4): p. 428-434.
30. Bonroy, K., et al., *Realization and characterization of porous gold for increased protein coverage on acoustic sensors.* Analytical Chemistry, 2004. **76**(15): p. 4299-4306.
31. van Noort, D. and C.F. Mandenius, *Porous gold surfaces for biosensor applications.* Biosensors & Bioelectronics, 2000. **15**(3-4): p. 203-209.
32. van Noort, D., R. Rani, and C.F. Mandenius, *Improving the sensitivity of a quartz crystal microbalance for biosensing by using porous gold.* Mikrochimica Acta, 2001. **136**(1-2): p. 49-53.
33. Imamura, M., et al., *Self-Assembly of Mediator-Modified Enzyme in Porous Gold-Black Electrode for Biosensing.* Sensors and Actuators B-Chemical, 1995. **24**(1-3): p. 113-116.
34. Schechter, B., *Bright new world.* New Scientist, 2003. **178**(2392): p. 31-33.
35. Ebbesen, T.W., et al., *Extraordinary optical transmission through sub-wavelength hole arrays.* Nature, 1998. **391**(6668): p. 667-669.
36. Conway, B.E. and W.G. Pell, *Power limitations of supercapacitor and capacitance*

distribution operation associated with resistance in porous electrode devices. Journal of Power Sources, 2002. **105**(2): p. 169-181.
37. Ding, Y., M.W. Chen, and J. Erlebacher, *Metallic mesoporous nanocomposites for electrocatalysis.* Journal of the American Chemical Society, 2004. **126**(22): p. 6876-6877.
38. Zeis, R., et al., *Platinum-plated nanoporous gold: An efficient, low Pt loading electrocatalyst for PEM fuel cells.* Journal of Power Sources, 2007. **165**(1): p. 65-72.
39. Xu, C.X., et al., *Low temperature CO oxidation over unsupported nanoporous gold.* Journal of the American Chemical Society, 2007. **129**(1): p. 42-43.
40. Zielasek, V., et al., *Gold catalysts: Nanoporous gold foams.* Angewandte Chemie-International Edition, 2006. **45**(48): p. 8241-8244.
41. Steele, B.C.H. and A. Heinzel, *Materials for fuel-cell technologies.* Nature, 2001. **414**(6861): p. 345-352.
42. Grimwade, M., *Surface Enrichment of Carat Gold Alloys – Depletion Gilding.* Gold Technology, 1999(26): p. 16-23.
43. Newman, R.C. and K. Sieradzki, *Metallic Corrosion.* Science, 1994. **263**(5154): p. 1708-1709.
44. Kelly, R.G., et al., *Brittle-Fracture of an Au/Ag Alloy Induced by a Surface-Film.* Metallurgical Transactions a-Physical Metallurgy and Materials Science, 1991. **22**(2): p. 531-541.
45. Corcoran, S.G. and K. Sieradzki, *Porosity Induced Scc of Silver.* Scripta Metallurgica et Materialia, 1992. **26**(4): p. 633-637.
46. Friedersdorf, F. and K. Sieradzki, *Film-induced brittle intergranular cracking of silver-gold alloys.* Corrosion, 1996. **52**(5): p. 331-336.
47. Forty, A.J., *Micromorphological studies of the corrosion of gold alloys.* Gold Bulletin, 1981. **14**(1): p. 25-35.
48. Erlebacher, J., *An atomistic description of dealloying - Porosity evolution, the critical potential, and rate-limiting behavior.* Journal of the Electrochemical Society, 2004. **151**(10): p. C614-C626.
49. Erlebacher, J. and K. Sieradzki, *Pattern formation during dealloying.* Scripta Materialia, 2003. **49**(10): p. 991-996.
50. Sieradzki, K., et al., *Computer simulations of corrosion: selective dissolution of binary Alloys.* Philosophical Magazine a-Physics of Condensed Matter Structure Defects and Mechanical Properties, 1989. **59**(4): p. 713-746.
51. Dursun, A., *Nanoposity formation in Ag-Au alloys.* Ph. D. Dissertation, 2003.
52. Gibson, L.J. and M.F. Ashby, *Cellular Solids: Structures and Properties*. 2nd ed. 1997: Cambridge University Press.
53. Parida, S., et al., *Volume change during the formation of nanoporous gold by dealloying.* Physical Review Letters, 2006. **97**(3): p. 035504.
54. Crowson, D.A., D. Farkas, and S.G. Corcoran, *Geometric relaxation of nanoporous metals: The role of surface relaxation.* Scripta Materialia, 2007. **56**(11): p. 919-922.
55. Volkert, C.A., et al., *Approaching the theoretical strength in nanoporous Au.* Applied Physics Letters, 2006. **89**(6): p. 061920.
56. Hakamada, M. and M. Mabuchi, *Nanoporous gold prism microassembly through*

a self-organizing route. Nano Letters, 2006. **6**(4): p. 882-885.
57. Sun, Y. and T.J. Balk, *A multi-step dealloying method to produce nanoporous gold with no volume change and minimal cracking.* Scripta Materialia, 2008. **58**(9): p. 727-730.
58. Senior, N.A. and R.C. Newman, *Synthesis of tough nanoporous metals by controlled electrolytic dealloying.* Nanotechnology, 2006. **17**(9): p. 2311-2316.
59. Biener, J., A.M. Hodge, and A.V. Hamza, *Microscopic failure behavior of nanoporous gold.* Applied Physics Letters, 2005. **87**(12): p. 024301-1-024301-4.
60. Hodge, A.M., et al., *Scaling equation for yield strength of nanoporous open-cell foams.* Acta Materialia, 2007. **55**(4): p. 1343-1349.
61. Biener, J., et al., *Nanoporous Au: A high yield strength material.* Journal of Applied Physics, 2005. **97**(2): p. 024301.
62. Biener, J., et al., *Size effects on the mechanical behavior of nanoporous Au.* Nano Letters, 2006. **6**(10): p. 2379-2382.
63. Li, R. and K. Sieradzki, *Ductile-Brittle Transition in Random Porous Au.* Physical Review Letters, 1992. **68**(8): p. 1168-1171.
64. Hakamada, M. and M. Mabuchi, *Mechanical strength of nanoporous gold fabricated by dealloying.* Scripta Materialia, 2007. **56**: p. 1003-1006.
65. Ding, Y. and J. Erlebacher, *Nanoporous metals with controlled multimodal pore size distribution.* Journal of the American Chemical Society, 2003. **125**(26): p. 7772-7773.
66. Zhu, J.Z., et al., *Mitigation of tensile failure in released nanoporous metal microstructures via thermal treatment.* Applied Physics Letters, 2006. **89**(13): p. 133104.
67. Seker, E., et al., *The effects of post-fabrication annealing on the mechanical properties of freestanding nanoporous gold structures.* Acta Materialia, 2007. **55**(14): p. 4593-4602.
68. Lee, D., et al., *Microfabrication and mechanical properties of nanoporous gold at the nanoscale.* Scripta Materialia, 2007. **56**(5): p. 437-440.
69. Snyder, J., K. Livi, and J. Erlebacher, *Dealloying silver/gold alloys in neutral silver nitrate solution: Porosity evolution, surface composition, and surface oxides.* Journal of the Electrochemical Society, 2008. **155**(8): p. C464-C473.
70. Hodge, A.M., et al., *Monolithic nanocrystalline Au fabricated by the compaction of nanoscale foam.* Journal of Materials Research, 2005. **20**(3): p. 554-557.
71. Lee, D., et al., *Observation of plastic deformation in freestanding single crystal Au nanowires.* Applied Physics Letters, 2006. **89**(11): p. 111916.
72. Sun, Y., et al., *Microstructure, stability and thermomechanical behavior of crack-free thin films of nanoporous gold.* Scripta Materialia, 2008. **58**(11): p. 1018-1021.
73. Landman, U., W.D. Luedtke, and J.P. Gao, *Atomic-scale issues in tribology: Interfacial junctions and nano-elastohydrodynamics.* Langmuir, 1996. **12**(19): p. 4514-4528.
74. Oliver, W.C. and G.M. Pharr, *An Improved Technique for Determining Hardness and Elastic-Modulus Using Load and Displacement Sensing Indentation Experiments.* Journal of Materials Research, 1992. **7**(6): p. 1564-1583.
75. Mathur, A. and J. Erlebacher, *Size dependence of effective Young's modulus of nanoporous gold.* Applied Physics Letters, 2007. **90**(6): p. 061910.

76. Dixon, M.C., et al., *Preparation, structure, and optical properties of nanoporous gold thin films.* Langmuir, 2007. **23**(5): p. 2414-2422.
77. Qian, L.H., et al., *Surface enhanced Raman scattering of nanoporous gold: Smaller pore sizes stronger enhancements.* Applied Physics Letters, 2007. **90**(15): p. 153120-1-153120-3.
78. Rosler, J., et al., *Fabrication of nanoporous Ni-based superalloy membranes.* Acta Materialia, 2005. **53**(5): p. 1397-1406.
79. Nix, W.D., *Mechanical properties of thin films.* Metall. Trans. A, 1989. **20**(11): p. 2217-2245.
80. Cullity, B.D. and S.R. Stock, *Elements of X-Ray Diffraction*. 3 rd ed. 2001, Upper Saddle River, NJ: Prentice Hall. 638-639.
81. Minor, A.M., J.W. Morris, and E.A. Stach, *Quantitative in situ nanoindentation in an electron microscope.* Applied Physics Letters, 2001. **79**(11): p. 1625-1627.
82. Sun, Y., et al., *The mechanical Behavior of nanoporous gold thin films.* JOM, 2007. **59**(9): p. 54-58.
83. Kramer, D., R. Nadar Viswanath, and J. Weissmuller, *Surface-stress induced macroscopic bending of nanoporous gold cantilevers.* Nano Letters, 2004. **4**(5): p. 793.
84. Sun, Y. and T.J. Balk, *Mechanical behavior and microstructure of nanoporous gold films.* Mater. Res. Soc. Symp. Proc., 2006. **924**: p. Z01-02-01-06.
85. Jianzhong, Z., et al., *Mitigation of tensile failure in released nanoporous metal microstructures via thermal treatment.* Applied Physics Letters, 2006. **89**(13): p. 133104-1.
86. Huang, J.-F. and I.-W. Sun, *Formation of nanoporous platinum by selective anodic dissolution of PtZn surface alloy in a Lewis acidic zinc chloride-1-ethyl-3-methylimidazolium chloride ionic liquid.* Chemistry of Materials, 2004. **16**(10): p. 1829-1831.
87. Sharma, S.K., et al., *Effects of thermal annealing of thin Au film on Fe40Ni38Mo4B18.* Materials Science and Engineering a-Structural Materials Properties Microstructure and Processing, 2003. **351**(1-2): p. 316-324.
88. Sharma, S.K., et al., *Effects of thermal annealing of thin Au film on Fe40Ni38Mo4B18 in ultrahigh vacuum (UHV).* Journal of Materials Science, 2004. **39**(20): p. 6291-6297.
89. Ding, Y., Y.J. Kim, and J. Erlebacher, *Nanoporous gold leaf: "Ancient technology"/advanced material.* Advanced Materials, 2004. **16**(21): p. 1897-1900.
90. Lu, X., et al., *Dealloying of Au-Ag thin films with a composition gradient: Influence on morphology of nanoporous Au.* Thin Solid Films, 2007. **515**: p. 7122-7126.
91. Balluffi, R.W., S.M. Allen, and W.C. Carter, *Kinetics of Materials*. 2005: Wiley-Interscience.
92. Freund, L.B. and S. Suresh, *Thin Film Materials: Stress, Defect Formation, and Surface Evolution*. 2003, Cambridge: Cambridge University Press.
93. Hertzberg, R.W., *Deformation and Fracture Mechanics of Engineering Materials*. 3rd ed. 1989, New York: John Wiley & Sons, Inc.
94. Sun, Y. and T.J. Balk, *Evolution of Structure, Composition and Stress in Nanoporous Gold Thin Films with Grain Boundary Cracks.* Metallurgical and

Materials Transactions A, 2008. **39A**: p. 2656-2665.
95. Pugh, D.V., A. Dursun, and S.G. Corcoran, *Formation of nanoporous platinum by selective dissolution of Cu from Cu0.75Pt0.25.* Journal of Materials Research, 2003. **18**(1): p. 216-221.
96. Hodge, A.M., et al., *Characterization and mechanical behavior of nanoporous gold.* Advanced Engineering Materials, 2006. **8**(9): p. 853-857.
97. Dursun, A., D.V. Pugh, and S.G. Corcoran, *Dealloying of Ag-Au alloys in halide-containing electrolytes - Affect on critical potential and pore size.* Journal of the Electrochemical Society, 2003. **150**(7): p. B355-B360.
98. Gorskii, V.V., M.I. Dekhtyar, and I.Y. Dekhtyar, *Effect of Uniaxial Stress on Mutual Diffusion in Ag-Au System.* Physica Status Solidi B-Basic Research, 1975. **70**(1): p. 133-138.
99. Dursun, A., D.V. Pugh, and S.G. Corcoran, *Dealloying of Ag-Au alloys in halide-containing electrolytes. Affect on critical potential and pore size.* Journal of the Electrochemical Society, 2003. **150**(7): p. 355-360.
100. Ji, C. and P.C. Searson, *Fabrication of nanoporous gold nanowires.* Applied Physics Letters, 2002. **81**(23): p. 4437-9.
101. Huang, J.-F. and I.W. Sun, *Fabrication and surface functionalization of nanoporous gold by electrochemical alloying/dealloying of Au-Zn in an ionic liquid, and the self-assembly of L-cysteine monolayers.* Advanced Functional Materials, 2005. **15**(6): p. 989.
102. Minor, A.M., et al., *A new view of the onset of plasticity during the nanoindentation of aluminium.* Nature Materials, 2006. **5**(9): p. 697-702.
103. Warren, O.L., et al., *In situ nanoindentation in the TEM.* Materials Today, 2007. **10**(4): p. 59-60.
104. Newman, R.C., et al., *Alloy corrosion.* MRS Bulletin, 1999. **24**(7): p. 24-8.
105. Ji, C. and P.C. Searson, *Synthesis and characterization of nanoporous gold nanowires.* Journal of Physical Chemistry B, 2003. **107**(19): p. 4494-9.

Vita

Ye Sun

Ye Sun was born on December 5, 1973, in Shuangyashan, Heilongjiang, China. In 1996, he graduated from Dalian Railway Institute (now Dalian Jiaotong University) with a Bachelor's of Science degree in Materials Engineering. After college, he moved to Harbin, Heilongjiang and worked for 5 years as a Materials Engineer at Harbin Continuous Welded Rail Company, a government-owned company. In the fall of 2001, Ye began graduate study at the Harbin Institute of Technology and earned a Master's of Science degree in Materials Science in 2003. In the fall of 2004, Ye joined the University of Kentucky to pursue his PhD in Materials Engineering.

Publications

Peer reviewed journals

1. Ye Sun, J. Ye, Andrew M. Minor and T. John Balk, *In-Situ Indentation of Nanoporous Thin Films,* Microscopy Research and Technique – 2008 in press
2. Ye Sun and T. John Balk, *Evolution of Structure, Composition and Stress in Nanoporous gold Thin Films with Grain Boundary Cracks*, Metallurgical and Materials Transactions A, **39A** 2656-2665 (2008)
3. Ye Sun, Kalan Kucera, Sofie Burger and T. John Balk, *Microstructure, Stability and Thermomechanical Behavior of Crack-Free Thin Films of Nanoporous gold*, Scripta Materialia **58** 1018-1021 (2008)
4. Ye Sun, T. John Balk, *A multi-step dealloying method to produce nanoporous gold with no volume change and minimal cracking*, Scripta Materialia **58** 727-730 (2008)
5. Ye Sun, Jia Ye, Zhiwei Shan, Andrew M. Minor, T. John Balk, *The Mechanical Behavior of Nanoporous gold Thin Films*, JOM **59**(9) 54-58 (2007)

6. Ye Sun, Qingchang Meng, Dechang Jia, Chunlong Guan, *Effect of Hexagonal BN on the Microstructure and Mechanical Properties of Si_3N_4 Ceramics*, Journal of Materials Processing Technology **182** 134-138 (2007)
7. Ye Sun, Qingchang Meng, Dechang Jia, Liangjun Huang, *Influence of Titanium Diboride on the Microstructure and Mechanical Properties of Silicon Nitride Ceramic*, Materials Letters **58** 2057-2060 (2004)
8. Xiaodong He, Chunlong Guan, Yao Li, Ye Sun, *Mechanical properties of Ni-Cr-Al-Y superalloy foil by EB-PVD*, The Journal of Nonferrous Metals **14** 255-258 (2004) (Chinese)
9. Chunlong Guan, Xiaodong He, Yao Li, Ye Sun, *Microstructure and Mechanical properties of Ni-Cr-Al alloy by EB-PVD*, Journal of Aeronautical Materials **25** 11-14 (2005) (Chinese)

Conference proceedings

1. Ye Sun, T. John Balk, *Mechanical Behavior and Microstructure of Nanoporous gold Films*, Mater. Res. Soc. Symp. Proc. 924 Z1.2.1-Z1.2.6 (2006)
2. Chunlong Guan, Yao Li, Xiaodong He, Ye Sun, *Microstructure and mechanical properties of a Ni-Cr-Al alloy by EB-PVD*, International SAMPE Technical Conference, SAMPE 2004 389-395 (2004)